FDD - Final Design Demonstration

FDD Report submission to compete at

European Hyperloop Week

Gronigen

Date of submission

19 April 2025

Contents

List of Figures

1 Introduction

Description of the applicant and list of updated team members.

Applicant: Hyperloop Manchester

1.1 List of Commitee members.

Role	**Name**
President	Baris Gurel
Vice President	Kaustubh Girish
Chief Engineer	Rutvik Perepa
General Secretary	Neme Okoroafor
Project Manager	Nabhanyu Shetti
Project Manager	Ekta Nair
Braking Lead	Adeesh Bansal
Chassis & Outer Shell Lead	Alen Sabu
Magnetic Levitation Lead	Tette Smit
Electronics & Software Lead	Rohan Verma
Future Concepts and Full Scale Lead	Matthew Smith + Elliott Quinney
Suspension Lead	Bryan Yip
Propulsion Lead	Temi + Daeton How
Business Team Lead	Jihwan Chung
Inclusivity Officer	Veronica Mendez
Social Secretary	Cengizhan Dogan
Treasurer	Matthew Smith

1.2 List of Team members.

Figure 1: Chassis and Outer-shell Team

Name
Alen Sabu
Alex Neytchev
Osazemwen Osarenmwinda
Parshad Prashant Sawant
Mohammed Nadeem
Qing Chang

Figure 2: Electronics and Software Team

Name
Rohan Verma
Taimur Khan
Chandramouli Goswami
Rehan Fonseka
Marriam Amir
Kshitij Gupta
Anishvar

Figure 3: Magnetic Levitation Team

Name
Santiago del Barrio Morales
Finlay Lloyd
Elizabeth O'Connor
James Tillery
Saad Ahmed
Ming-Han
Idris Muzafar
Joseph Lailey

Figure 4: Braking Team

Name
Adeesh Bansal
Leon Jacob
Alejandra Vidaurrazaga
Kaif Khan
Hrishikesh Pawar
Worachot Tharahirunchot
Sarah Banoun
Emma Stevenson
Ye Emanuele Yang

Figure 5: Suspension Team

Name
Bryan Yip
Neme Okoroafor
Farouk Yousif
Katie Mui
Fadlan Zain
Arailym Oteu
Gary Lai
Kentaro Akihara
Wayne Leung
Reuben David Manjaly
Nipun Neil
Emma Kenard

Figure 6: Engineering Teams Organization

1.3 EHW 2025 Awards Entered

Hyperloop Manchester wished to enter its guidance subsystem in the guidance category. Hyperloop Manchester also wishes to enter the engineering excellence diploma award with its mechanical subsystem.

1.4 Brief System Overview.

Subsystem Overview

The Hyperloop pod is divided into the following key subsystems:

- **Propulsion**

- **Power**
- **Chassis**
- **Braking**
- **Suspension**
- **Control**

Each subsystem is managed by a dedicated team responsible for its design, development, and assembly. In addition to subsystem-specific tasks, each team ensures seamless integration with the central chassis structure to maintain overall functionality and system coherence.

Expected acceleration requirement in present in the braking and maglev sections.

Track

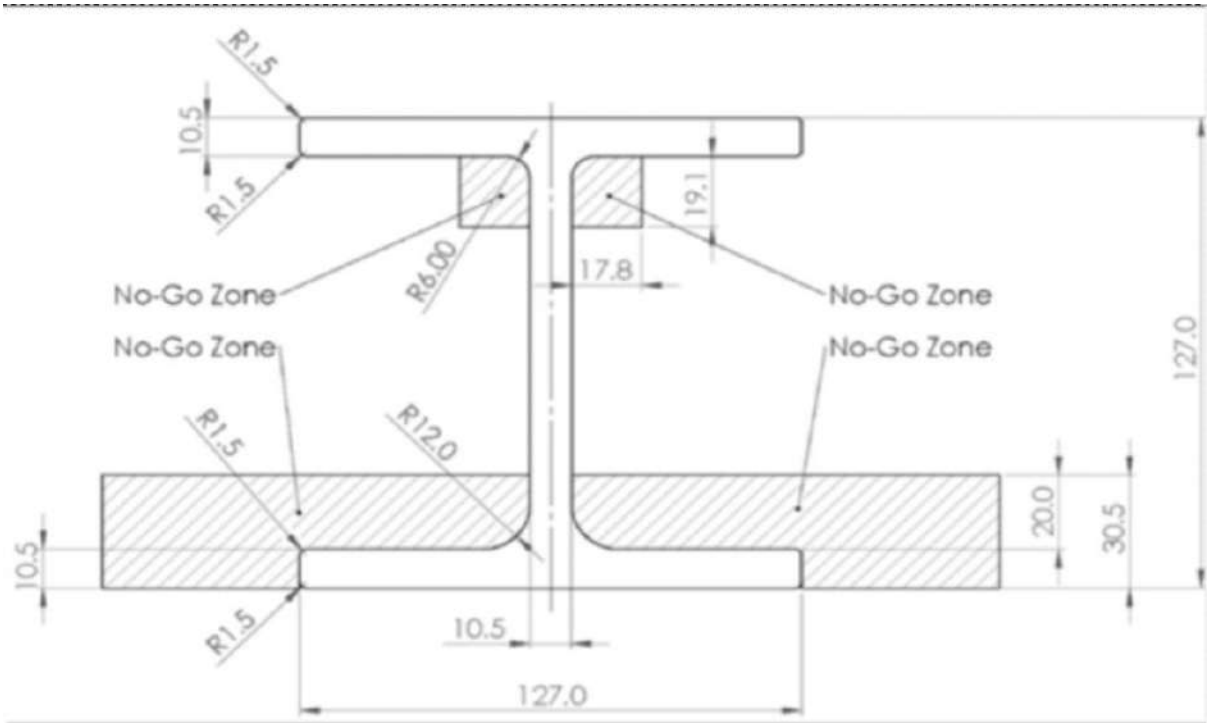

Figure 7: Pod Assembly render.

The Manchester Hyperloop pod is designed to operate on a 24-meter I-beam track, enabling controlled magnetic levitation demonstrations. The track is constructed using 6061-T6 aluminium, chosen for its excellent strength-to-weight ratio and compatibility with electromagnetic systems.

To ensure reliable performance and safety, the braking and lateral guidance systems are configured to function exclusively in designated areas along the track. These operational zones explicitly avoid the predefined *no-go zones*, where magnetic interference, structural limitations, or sensor inaccuracies may compromise system effectiveness.

The strategic division of the track into active and restricted regions ensures that critical subsystems such as levitation, braking, and guidance can function optimally without interference, supporting a safe

and repeatable testing environment. The track is supported by aluminum profile stand structures, which provide a stable base for the I-beam. The I-beam is securely clamped to both the track supports and the track itself, enhancing overall structural stability and ensuring reliable operation.

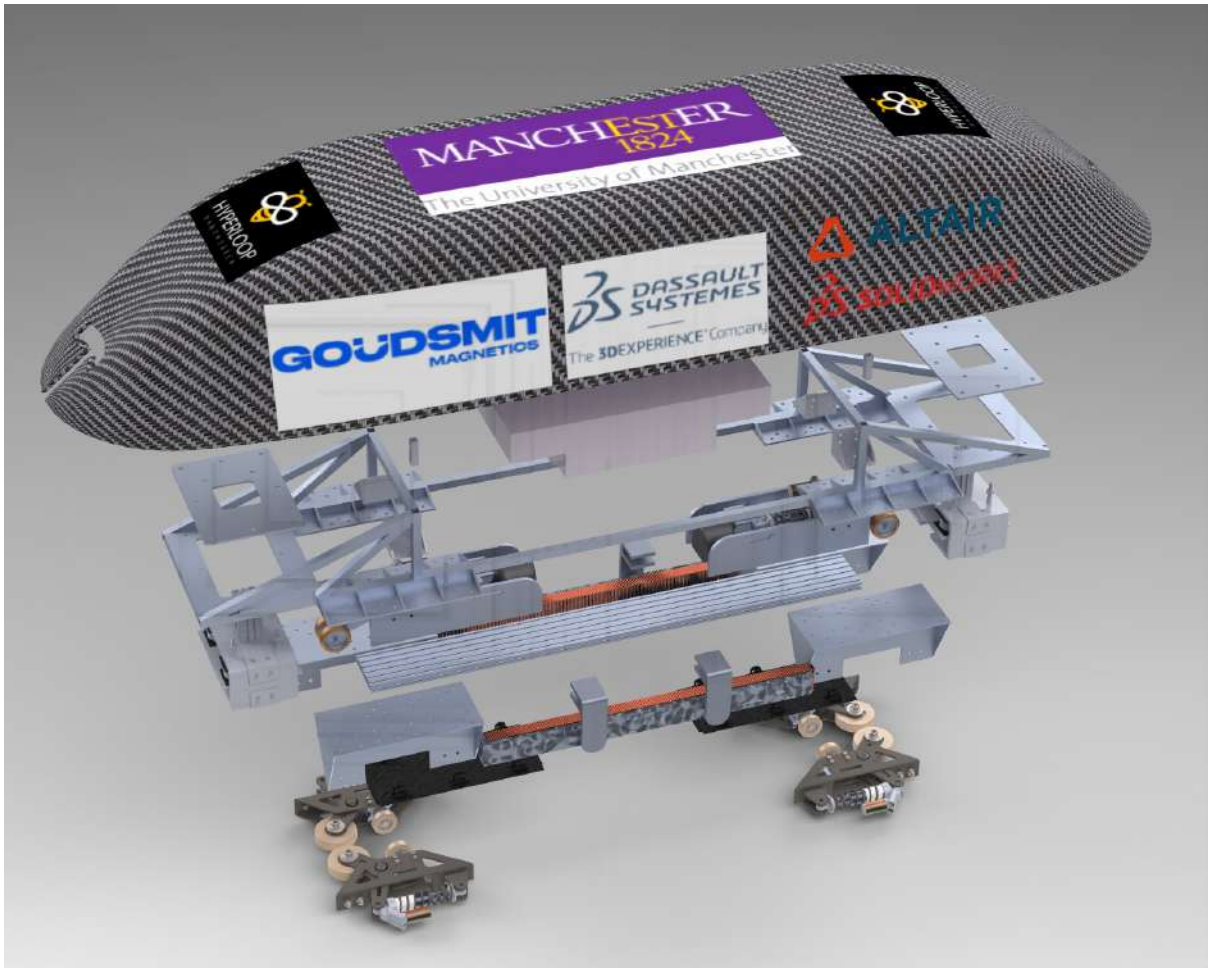

Figure 8: Pod Assembly render.

Transport and Logistics

The completed Hyperloop pod and its supporting equipment are planned to be transported to the European Hyperloop Week (EHW) Gronigen, via road freight. Given the size, weight, and sensitivity of the pod and associated systems, the use of a professional logistics or moving company is deemed the most practical and secure method; we are in contact with potential moving partners.

To ensure safe handling and transport, the pod and the track will be disassembled into modular sections and packed into custom-built crates, which will be loaded onto a hired transport van or lorry. The team will accompany the shipment to assist with on-site unloading, inspection, and final assembly at the competition venue.

Given the expected transport and accommodation costs, additional funding will be sought through coordination with the Faculty of Science and Engineering (FSE). Budget discussions are currently underway to secure partial financial support from the university, with the remainder being covered through

Parameter	Value
Length [mm]	1998
Width [mm]	347
Height [mm]	193
Weight [kg]	100
Vertical levitation method	Halbach Linear array Array
Vertical levitation system max. current [A]	N/A
Lateral levitation method	EMS System
Lateral levitation system max. current [A]	N/A
Motor concept	Brushless DC Motor
Motor max. current [A]	278 A A
Regenerative braking used	No
LV system max. voltage [V]	12V
HV system max. voltage [V]	50V
Braking method	Pneumatic activated spring calliper brakes.
Pneumatic system max. pressure [bar]	15 Bar
Data Log Frequency [Hz]	10Hz
Board communication protocols	Serial, WiFi and CAN

Table 2: System Overview Specifications

sponsorships and society fundraising initiatives. The FSE has expressed interest in supporting the team's participation at EHW as part of its commitment to promoting student-led engineering innovation and international collaboration.

1.5 Philosophy

At Manchester Hyperloop, we believe in the power of innovation, collaboration, and continuous improvement. Our philosophy is rooted in the pursuit of excellence in engineering, where hands-on learning, teamwork, and creative problem-solving form the foundation of our approach. We are committed not only to designing and building a cutting-edge Hyperloop pod but also to refining our work year after year, ensuring that we challenge the limits of what's possible in the realm of high-speed, sustainable transportation. Through our annual participation in various global Hyperloop Week competition, we push ourselves to grow, to learn, and to make a meaningful contribution to the future of mobility. Our community of engineers is dedicated to shaping the next generation of transportation technology, one innovation at a time.

1.6 Primary Objectives.

The primary objectives of Manchester Hyperloop, based on the philosophy and mission, would be:
1. Design and Build a Hyperloop Pod: Develop and construct a functional Hyperloop pod that incorporates cutting-edge technology and engineering principles, demonstrating innovation and technical skill.
2. Continuous Improvement and Refinement: Iteratively improve designs and systems each year, ensuring that every version of the Hyperloop pod surpasses its predecessor in terms of efficiency, performance, and sustainability.
3. Enhance Technical Skills and Innovation: Foster a culture of learning and technical growth, where each team member develops expertise in their field, contributing to the collective innovation of the pod

design.

4. Promote Teamwork and Collaboration: Cultivate a collaborative environment where different subteams, from mechanical to software, work together seamlessly, sharing knowledge, resources, and skills to achieve common goals.

1.7 Development Environment.

Hyperloop Manchester, is situated on the grounds of the University of Manchester, but operates independently, distinct from the university's direct affiliation. The team meets twice every week. Aside from these frequent meetings, the team keeps an open line of contact to ensure that information is shared fluidly across members. The research objectives began with a thorough analysis of the previous year's successes in each separate subsystem, providing the groundwork for the current academic year's activities. This thorough study contributed in the creation of a strategic work plan designed to improve and polish our subsystem designs. The formation of a series of specific tasks, each designed to reinforce the design of our subsystems, was central to this approach. The complete documenting of every choice was a major component of our methodology, ensuring a transparent and informed design process. We emphasised the incorporation of simulations in accordance with our commitment to precision. These simulations are critical in creating useful data, as they serve as the foundation for our analytical computations.

Budget Breakdown

1.8 Source of funding.

Hyperloop Manchester is registered as a student society under the student union of the University of Manchester, as such we receive funding from the Student Union, this along with sponsorships are our main sources of funding to build and compete with a pod.

2 Scaling up of the hyperloop pod.

Scaling the Hyperloop pod to a full scale system encounter major challenges due to aerodynamic limitations especially the Kantrowitz limit. This limit defines the highest speed a pod can travel in a low pressure tube before the airflow around it becomes choked. As the pod's cross-sectional area increases, or the tube diameter decreases both of which raise the blockage ratio, the Mach number at which choking occurs decreases. Once this threshold is passed the air can no longer bypass the pod efficiently and shock waves form. This leads to a rapid increase in pressure drag often referred to as the syringe effect where the pod acts like a piston, compressing air in front of it. (2) used CFD simulations to show that although axial compressors can help reduce this pressure build-up and lower power consumption by up to 47.5% their benefit becomes limited at larger pod sizes (2). Other aerodynamic challenges such as wave drag, turbulent flow and heat buildup also make it harder to scale up the system. Similar

Table 3: Project Budget Breakdown

Category	Supplier	Item	Cost (£)
Electronics	RS	Various electronics components	229.57
Suspension	Technica	Wheels	83.18
	KJN	Aluminium Profile	139.18
	RS	Igus Bearings	59.04
Full Team	RS	Cirlips & Pliers	390.87
	Orbital Fasteners	Various M grade fasteners	748.99
	FESTO	Fluidsim software licenses	592.21
	Global Hyperloop Competition	GHC registration	39.60
	Squarespace	Website	19.20
Braking	Igus	Bearings	46.62
	RS	Shaft Collar	27.96
	Spring Masters	Springs	62.63
	GWR Fasteners	Threaded spacers	77.94
Chassis	Metals4U	Aluminium Box section	21.60
	Easy Composites	Aluminium Honeycomb sheet	158.40
	Metals4U	Aluminium box section, aluminium sheet	321.46
Propulsion	Amazon	Mosfets, Arduino, Plug	45.34
	RS	2x maxon motors	665.74
	Stepper Online	2x motor controllers	56.46
	UoM Workshop	Not received receipts	unknown
		Total	**3,785.99**

problems were experienced in early high speed rail research like Japan's superconducting maglev project where air resistance became a major issue above 500 km/h despite open-air designs and streamlined shapes (3). This shows that to scale the Hyperloop pod effectively we would not only need to improve its aerodynamic design but possibly make the tube much larger which would be very expensive and difficult. Thermal management is another big issue in designing a full scale Hyperloop pod. Since the pods travel in a near vacuum environment (about 100 Pa) regular cooling methods like air or liquid convection don't work. A full-size pod could generate over 30 MW of heat from systems like propulsion, levitation, electronics, and passenger support. According to the Delft Hyperloop VII (2023) study three possible solutions were analysed Radiative Heat Removal Systems (RHRS), Sublimation-Based Heat Removal Systems (SBHRS) and Heat Storage Systems (HSS) using Phase Change Materials (PCMs). RHRS work similarly to spacecraft cooling but are only effective for small heat loads due to the small temperature difference between the pod and the tunnel air. SBHRS can manage larger amounts of heat by sublimating substances like water, but they require a lot of extra equipment such as vacuum pumps and condensers which makes the pod heavier and more complicated. HSS are passive systems that store heat by melting PCMs but they can only store a limited amount of energy and need to be recharged after each trip (4). If a full-scale pod doesn't have a reliable Thermal Management System (TMS) it could overheat quickly damaging electronics and making the system unsafe. Similar problems were handled in the Japanese maglev project using liquid helium cooling and insulation but this method is not practical for the long-distance, high-speed travel the Hyperloop aims to offer (3). Overall, the combined aerodynamic and thermal challenges indicate that, without sophisticated and wellintegrated systems to

Table 4: Project Income Breakdown

Income Source	**Amount (£)**
Confirmed Income	
FSE Budget (SU account)	8,500.00
FSE Budget (workshop)	1,500.00
Membership fees (SEM 1)	1,410.00
Subtotal (Confirmed)	**11,410.00**
Expected Income	
RS Cash Grant	500.00
RS Credit Grant	500.00
Membership fees (SEM 2)	unknown
Subtotal (Expected)	**1,000.00**
Grand Total IN	**12,410.00**

Table 5: Proposed (costs are estimates)

Category		**Cost**
Suspension		
PCB way	CNC machined components	£812.53
Propulsion		
Enepaq	Battery	£1,300.00
Stepper online	2x Motor Controllers	£56.46
RS	2x Motors	£665.74
unknown	Bearings	£50.00
unknown	Motor wheels	£125.00
unknown	Couples	£100.00
unknown	Shaft	£15.00
Maglev		
unknown	T bolts	£40.00
Full scale & Concepts		
unknown	Rover components	£400.00
Full Team		
logomeup	Tshirts, hoodies	£1,000.00
unknown	Track clamps + clips	£400.00
Total		**-£4,964.73**

manage airflow and heat, developing a safe and effective full-scale Hyperloop pod remains unachievable at this stage.

Table 6: Summary

Item	**Amount**
Grand Total Out	-£8,750.71
Outstanding Balance	£7,624.01
Balance after proposed OUT and expected IN	£3,659.29

3 Chassis

3.1 Overview of Design.

The Hyperloop pod's chassis design prioritizes four key attributes: strength, stiffness and weight requirements, modularity, and cost-effectiveness. To achieve this, the design strategically integrates elements of both ladder and truss structures, leveraging the strengths of each to create a framework that efficiently distributes loads. This hybrid approach ensures structural integrity while minimizing weight.

Modularity is a core principle, allowing the chassis to accommodate various subsystems and facilitating future upgrades or design iterations. This adaptability extends to ease of manufacturing and maintenance. The modularity is achieved by leaving several open sections in the ladder and the truss area, so that once the battery pack and other systems are integrated, the chassis can be expanded by welding at nodes more primary and secondary support load-bearing members. Furthermore, the sheet metals can be re-drilled for further adjustments for suspension and braking and still retain their structural integrity.

The chassis incorporates a semi-space frame design, providing a balance of strength and weight reduction. Reinforced mounting points are integrated throughout the structure to securely house components and ensure their stability under operational stresses. This reinforced framework also provides the necessary flexibility to accommodate future modifications or the integration of new technologies. The semi-space frame also incorporates cut sheet metal weldments, which are then welded, and the loads from the suspension, brakes and top suspension are all transferred through common welded plate to the chassis nodes.

The magnetic levitation system placed at the center of the pod, posed an integration challenge for connecting the top suspension and the chassis effectively, due to the awkward nature of the mounts which had to be created for the integration of the top suspension. The idea hence formed, is to ensure that the rolling phase of the journey is mostly handled by the maglev ski alone i.e. the maglev ski is stressed, the chassis member chosen to connect to the ski is split, for weight considerations, its also made of aluminium profile, it has very good sectional stiffness (owing to its high second area of moment). This meant that the loading of the pod should it roll in the levitation phase needed to be accounted for and hence the side suspension plates which connect to the maglev ski needed to act as a stressed member.

3.2 Specifications

Material Choice:

- Balances strength, stiffness and weight requirements.
- Suitable for applications requiring high structural performance and durability.

Material Used: Aluminium 6061-T6

Component	Weight (kg)
Truss Weight	2.804
Guide Suspension Mount (4 units)	0.763 x 4
Guide Suspension Integration Plate (4 units)	0.599 x 4
Top Suspension Mount (4 units)	0.34 x 4
Braking Integration Plate (2 units)	0.735 x 2
Braking Mounting Plate (2 units)	0.477 x 2
Total Weight	**12.04**

Table 7: Weight Breakdown of Truss and Mount Components

Subsystem Integration

Mounts: The mounts are reinforced to provide increased strength, ensuring reliability and durability under operational loads. They are also designed with modularity in mind, allowing for easy customization and replacement to accommodate varying subsystem requirements.

Dimensions The axis plane is as follows: the pod length is defined along the z-axis, the pod width is defined along the x-axis, and the pod height is defined along the y-axis.

Component	Length (L) mm	Width (W) mm	Height (H) mm
Truss Frame	1998	348	193
Guide Wheel Suspension Mount	346	130	151.5
Top Suspension Mount	230	75	65
Brake Mounts	190	270	5

Table 8: Dimensions of Truss Frame and Mounts

3.3 Design for Manufacture: Chassis

3.3.1 Overview

The hyperloop chassis system is designed to provide structural support while ensuring stability, safety, and efficient transfer of forces during operation. It is built from Aluminium 6061 T6, chosen for its high strength-to-weight ratio and corrosion resistance. The system consists of several key components, each with a specific function. Square tube cross sections form the primary framework of the chassis. The tubes provide structural strength and rigidity to support the weight of the capsule and withstand external forces during operation. Guide wheel weldments are positioned on both sides of the chassis, the guide wheel weldments are critical for maintaining smooth movement along the track. They provide stability by ensuring that the capsule stays aligned with the track, preventing lateral movement during high-speed travel. Top suspension (TS) mounts (Front, Side, and Bottom Parts) are integral to the suspension system, providing support and absorbing dynamic forces acting on the chassis. The front, side, and bottom TS mounts are attached to the frame to ensure the suspension remains functional and balanced, maintaining stability during acceleration, deceleration, and turns. The chassis frame comprises several aluminium 6061 T6 components, including structural tubes, braking plates, and welded assemblies. Below is a summary of the key components:

Sr No.	Component Name	Quantity	Material
1	Square tube cross section (19*19*1.6 mm)	20	Aluminium 6061 T6
2	Breaking Plate	2	Aluminium 6061 T6
3	Breaking Weldment	2	Aluminium 6061 T6
4	Guid Wheel Weldment Right	2	Aluminium 6061 T6
5	Guid Wheel Weldment Left	2	Aluminium 6061 T6
6	LH GW Mount Top Part	2	Aluminium 6061 T6
7	RH GW Mount Top Part	2	Aluminium 6061 T6
8	LH GW Mount Front	2	Aluminium 6061 T6
9	RH GW Mount Front	2	Aluminium 6061 T6
10	LH GW Mount Side	2	Aluminium 6061 T6
11	RH GW Mount Side	2	Aluminium 6061 T6
12	T6 Mount Front Part	4	Aluminium 6061 T6
13	T6 Mount Side Part	8	Aluminium 6061 T6
14	T6 Mount Bottom Part	4	Aluminium 6061 T6

Table 9: Component List Chassis

3.3.2 Component Manufacturing Processes

All components are depicted in the appendix. **Square Tube Cross Section (19x19x1.6 mm)**

- **Quantity:** 14
- **Material:** Aluminium 6061 T6
- **Manufacturing Process:**
  - **Band Saw Cutting to Length:** The square tube cross-sections are cut to their required lengths using a band saw. This process is efficient for cutting long, straight sections of metal. The band saw uses a continuous blade with teeth to precisely cut the aluminium tubes, minimizing waste and ensuring accurate length dimensions.

Braking Plate

- **Quantity:** 2
- **Material:** Aluminium 6061 T6
- **Manufacturing Process:**
  - **Water Jet Cutting:** Water jet cutting is used to cut the complex profile of the breaking plates. The high-pressure jet of water, often combined with an abrasive material, allows for precise cutting of intricate shapes in the aluminium without affecting the material's integrity. It avoids heat-affected zones, ensuring no distortion.
  - **Drilling to Nominal Diameter:** After the initial cut, holes of precise diameters are drilled into the breaking plates to accommodate fasteners or mounting hardware.

Breaking Weldment

- **Quantity:** 2

- **Material:** Aluminium 6061 T6
- **Manufacturing Process:**
  - **Water Jet Cutting & Drilling to Nominal Diameter:** Similar to the breaking plate, this component undergoes water jet cutting to create the necessary profiles. Precision drilling is also performed to achieve the required hole diameters for further assembly.

Guide Wheel Weldment Right & Left

- **Quantity:** 2 (Right), 2 (Left)
- **Material:** Aluminium 6061 T6
- **Manufacturing Process:**
  - **Water Jet Cutting & Drilling to Nominal Diameter:** These components are cut to shape using water jet cutting, followed by drilling to the nominal diameters needed for assembly. The guide wheel weldments are critical for the precise movement and positioning of the braking system, so dimensional accuracy is important.

LH & RH Guide Wheel Mount Top Part

- **Quantity:** 2 (LH), 2 (RH)
- **Material:** Aluminium 6061 T6
- **Manufacturing Process:**
  - **Water Jet Cutting & Drilling to Nominal Diameter:** The left and right-hand top mounting parts of the guide wheel are created by water jet cutting, which produces a clean edge with minimal material deformation. The holes are then drilled to the precise nominal diameter for mounting or bolting the parts together.

LH & RH Guide Wheel Mount Front

- **Quantity:** 2 (LH), 2 (RH)
- **Material:** Aluminium 6061 T6
- **Manufacturing Process:**
  - **Water Jet Cutting & Drilling to Nominal Diameter:** Similar to the top parts, the front mounting parts for both left and right guide wheels are fabricated using water jet cutting. Post cutting, drilling is used to make holes for screws or bolts that will secure the parts during assembly.

LH & RH Guide Wheel Mount Side

- **Quantity:** 2 (LH), 2 (RH)

- **Material:** Aluminium 6061 T6
- **Manufacturing Process:**
  - **Water Jet Cutting:** These side parts are cut using water jet technology to achieve precise dimensions for the required shape. The cutting process allows for high accuracy in cutting through the aluminium without warping.

TS Mount Front Part

- **Quantity:** 4
- **Material:** Aluminium 6061 T6
- **Manufacturing Process:**
  - **Water Jet Cutting & Drilling to Nominal Diameter:** The torsion spring mount front parts are first cut using water jet cutting, followed by drilling to achieve the required hole sizes. This allows the components to be correctly mounted in the hyperloop system.

TS Mount Side Part

- **Quantity:** 8
- **Material:** Aluminium 6061 T6
- **Manufacturing Process:**
  - **Water Jet Cutting:** These side parts are primarily made using water jet cutting, allowing the manufacturer to precisely shape the components while maintaining the material's properties.

TS Mount Bottom Part

- **Quantity:** 4
- **Material:** Aluminium 6061 T6
- **Manufacturing Process:**
  - **Water Jet Cutting & Drilling to Nominal Diameter:** The bottom parts of the torsion spring mount undergo water jet cutting, and after shaping, holes are drilled to the required nominal diameter. This ensures compatibility with other components in the assembly process.

3.3.3 Material Selection

The chassis is primarily constructed using Aluminium 6061 T6 due to its high strength-to-weight ratio, corrosion resistance, and good weldability. This material selection ensures structural durability while maintaining lightweight properties essential for high-speed transportation.

3.3.4 Design for Manufacturability Considerations

- **Material Optimization:** Minimizing material waste through efficient cutting techniques and nesting strategies for water jet cutting.
- **Tolerance Control:** Ensuring precise cutting and drilling to reduce post-processing and assembly errors.
- **Assembly Efficiency:** Using modular weldments and prefabricated sub-assemblies to streamline welding and reduce overall manufacturing time.
- **Structural Integrity:** Maintaining adequate weld penetration and joint strength to support high loads and dynamic forces during operation.

Component Manufacturing Details

Component	Details
Square Tube Cross Section (19x19x1.6 mm)	**Quantity:** 14 **Material:** Aluminium 6061 T6 **Manufacturing Process:** **Band Saw Cutting to Length:** The square tube cross-sections are cut to their required lengths using a band saw. This process is efficient for cutting long, straight sections of metal. The band saw uses a continuous blade with teeth to precisely cut the aluminium tubes, minimizing waste and ensuring accurate length dimensions.
Braking Plate	**Quantity:** 2 **Material:** Aluminium 6061 T6 **Manufacturing Process:** **Water Jet Cutting:** Water jet cutting is used to cut the complex profile of the breaking plates. The high-pressure jet of water, often combined with an abrasive material, allows for precise cutting of intricate shapes in the aluminium without affecting the material's integrity. It avoids heat-affected zones, ensuring no distortion. **Drilling to Nominal Diameter:** After the initial cut, holes of precise diameters are drilled into the breaking plates to accommodate fasteners or mounting hardware.
Breaking Weldment	**Quantity:** 2 **Material:** Aluminium 6061 T6 **Manufacturing Process:**

Component	Details
	Water Jet Cutting & Drilling to Nominal Diameter: Similar to the breaking plate, this component undergoes water jet cutting to create the necessary profiles. Precision drilling is also performed to achieve the required hole diameters for further assembly.
Guide Wheel Weldment Right & Left	**Quantity:** 2 (Right), 2 (Left) **Material:** Aluminium 6061 T6 **Manufacturing Process:** **Water Jet Cutting & Drilling to Nominal Diameter:** These components are cut to shape using water jet cutting, followed by drilling to the nominal diameters needed for assembly. The guide wheel weldments are critical for the precise movement and positioning of the braking system, so dimensional accuracy is important.
LH & RH Guide Wheel Mount Top Part	**Quantity:** 2 (LH), 2 (RH) **Material:** Aluminium 6061 T6 **Manufacturing Process:** **Water Jet Cutting & Drilling to Nominal Diameter:** The left and right-hand top mounting parts of the guide wheel are created by water jet cutting, which produces a clean edge with minimal material deformation. The holes are then drilled to the precise nominal diameter for mounting or bolting the parts together.
LH & RH Guide Wheel Mount Front	**Quantity:** 2 (LH), 2 (RH) **Material:** Aluminium 6061 T6 **Manufacturing Process:** **Water Jet Cutting & Drilling to Nominal Diameter:** Similar to the top parts, the front mounting parts for both left and right guide wheels are fabricated using water jet cutting. Post cutting, drilling is used to make holes for screws or bolts that will secure the parts during assembly.
LH & RH Guide Wheel Mount Side	**Quantity:** 2 (LH), 2 (RH) **Material:** Aluminium 6061 T6 **Manufacturing Process:**

Component	Details
	Water Jet Cutting: These side parts are cut using water jet technology to achieve precise dimensions for the required shape. The cutting process allows for high accuracy in cutting through the aluminium without warping.
TS Mount Front Part	**Quantity:** 4 **Material:** Aluminium 6061 T6 **Manufacturing Process:** **Water Jet Cutting & Drilling to Nominal Diameter:** The torsion spring mount front parts are first cut using water jet cutting, followed by drilling to achieve the required hole sizes. This allows the components to be correctly mounted in the hyperloop system.
TS Mount Side Part	**Quantity:** 8 **Material:** Aluminium 6061 T6 **Manufacturing Process:** **Water Jet Cutting:** These side parts are primarily made using water jet cutting, allowing the manufacturer to precisely shape the components while maintaining the material's properties.
TS Mount Bottom Part	**Quantity:** 4 **Material:** Aluminium 6061 T6 **Manufacturing Process:** **Water Jet Cutting & Drilling to Nominal Diameter:** The bottom parts of the torsion spring mount undergo water jet cutting, and after shaping, holes are drilled to the required nominal diameter. This ensures compatibility with other components in the assembly process.
Material Selection	The chassis is primarily constructed using Aluminium 6061 T6 due to its high strength-to-weight ratio, corrosion resistance, and good weldability. This material selection ensures structural durability while maintaining lightweight properties essential for high-speed transportation.
Design for Manufacturability Considerations	**Material Optimization:** Minimizing material waste through efficient cutting techniques and nesting strategies for water jet cutting. **Tolerance Control:** Ensuring precise cutting and drilling to reduce post-processing and assembly errors. **Assembly Efficiency:** Using modular weldments and prefabricated sub-assemblies to streamline welding and reduce overall manufacturing time.

Component	Details
	Structural Integrity: Maintaining adequate weld penetration and joint strength to support high loads and dynamic forces during operation.

3.4 Conclusion

In conclusion, the Design for Manufacturability (DFM) process for the hyperloop chassis system has focused on optimizing material selection, manufacturing methods, and assembly efficiency. Using Aluminium 6061 T6 and processes like band saw cutting, water jet cutting, and drilling, the components are designed for precision and minimal material waste. Key elements, including square tube cross sections, guide wheel weldments, and top suspension mounts, are assembled to ensure structural integrity, stability, and performance. The DFM process has resulted in a chassis that meets the required specifications, ensuring safe and efficient integration into the hyperloop system.

4 Braking

4.1 Overview

From a top-level view, the proposed friction braking system clamps onto the top flange of the I beam with a pair of power-off brakes that ensure full functionality of the pod when power is turned off. It achieves this with a combination of pneumatic cylinders and springs. In terms of an operational perspective, this braking system targets a maximum velocity of 30 km/h prior to braking and stoppage within 4m. The free body diagram for the braking system can be viewed in the appendix, from the FBD we can see that the expansion of the springs has two implications. The first is that the top brake pad, indicated in green, is pressed onto the top portion of the I beam. The second is that the springs' expansion causes the entire actuator assembly to move upwards, thus causing the bottom brake pads, in red, to press against the bottom of the top flange.

The "power-off brakes" function as follows: pressure is established in the rod end of the cylinder using a solenoid valve, thus causing the piston to retract and compress the springs as shown in the image below. Thus, when power is switched off - be that intentionally or in a power outage - the solenoid valve is no longer able to maintain the pressure in the rod end and the springs are able to expand.

4.2 Specifications

Parameter	**Value**
L0 - Unloaded length (mm)	88.10
Ln - Max. loaded length (mm)	41.10
Sn - Maximum travel (mm)	47.00
Fn - Maximum load at Ln (N)	303.88
R - Spring constant (N/mm)	6.48

Table 11: Spring Specifications

4.2.1 Component List

The following table lists the components used in the system:

Table 12: Component List

Part No.	Part Name	Drawing Name	Quantity
1	Attachment_plate.SLDPRT	Attachment_plate drawing.SLDDRW	12
2	Bottom_Brake_Pad.SLDPRT	Bottom_Brake_Pad drawing.SLDDRW	24
3	Bottom_Plate.SLDPRT	Bottom_Plate drawing.SLDDRW	24
4	Brake Pad.SLDPRT	Brake Pad drawing.SLDDRW	12
5	Brake Pad holder.SLDPRT	Brakepad holder drawing.SLDDRW	12
	L bracket short.SLDPRT	L bracket short drawing.SLDDRW	24

Continued on next page

Table 12 – continued from previous page

Part No.	Part Name	Drawing Name	Quantity
6	L bracket long.SLDPRT	L bracket long drawing.SLDDRW	24
7	Side_Plate.SLDPRT	Side_Plate drawing.SLDDRW	24
8	Rail.SLDPRT	Rail drawing.SLDDRW	24
9	Top_Plate.SLDPRT	Top Plate drawing.SLDDRW	12
10	Nyloc moer M10.SLDPRT	off the shelf	48
11	Igus_Bearing.SLDPRT	off the shelf	612
12	Final Spring.SLDPRT	off the shelf	24
13	Shaft Collar	off the shelf	24
14	Connecting_Rod.SLDPRT	Connecting_Rod drawing.SLDDRW	12

Step	**Calculation / Result**
$v^2 = u^2 + 2as$	$0 = 8.33^2 + 2a(4)$, $a = -8.67\,\text{ms}^{-2}$
$F_{\text{net}} = F_f = ma$	$F_f = 50(8.67) = 433.68\,\text{N}$
$F_f = F_N k$	$433.68 = F_N(1)$, $F_N = 433.68\,\text{N}$
F_N(Required) = F_N(Safety Factor)	F_N(Required) = 867.36 N
F_N(Required) = 433.68 N per Braking System	$F_{\text{Spring}} = 216.84\,\text{N}$ per spring, Spring Selected
Ensure actuator compresses both springs	Actuator force = 620 N at 10 bar working pressure
Maximum Force = 303.88 N	$x = \frac{F_2 - F_1}{k}$, $x = \frac{303.88 - 216.84}{6.48}$, $x = 13\,\text{mm}$

Table 13: Calculation and Results for Braking System

The system integrates into the main chassis via the means of an attachment plate designed to join to the rails of the braking system, as this is the only part that remains stationary during the braking procedure.

system due to the compressibility of the air. Cylindrical rails were selected as these can go through the profile of the brake pad, as opposed to a flat style rail which would have to be attached to the side, thus being more prone to bending moments. Plain bearings were the best choice for guides along the rails, as they are the easiest to assemble. The size of the rails (diameter 10mm) themselves was determined via an FEA simulation conducted on a rail of circular profile under transverse shear stress.

4.3 Results and Visuals

4.3.1 Variation of Distance, Velocity and Deceleration with Time

The distance graph flattens rapidly due to the non-linear nature of deceleration in this system resulting in the pod completely stopping in half a metre.

The velocity graph has akin to, but non-ideal behaviour. The graph starts off with a flat line indicating the initial constant velocity at which we assume the hyperloop pod to be travelling at, finally resulting in a velocity of zero when the pod comes to a complete stop.

The deceleration plot shows development of deceleration in cases of emergency braking in further detail. We can see that the deceleration is characterised by a sharp incline initially when the power is cut off and the pneumatic actuator loses pressure, resulting in the springs unloading and brake pads applying pressure on the I-beam after which deceleration increases at a much more gradual pace.

4.3.2 Variation of Weight Distribution with Time

The plot depicts the weight distribution during dynamic loading conditions on the front and rear brakes of the pod. The positive values depict downward force, and the negative values depict when loading or force in the upward direction. The static loads for both the front and rear brakes Centres of Gravity (CoGs) (light blue and green lines) coincide due to the equidistant nature of the pads to the pod's CoG.

For dynamic loading, both experience varying loading conditions over time, which follows the total down force generated by the difference between the weight and maglev force at a particular velocity value. The front brakes (red line) experience downward force throughout the braking time, which means the top pads for both system designs at the front get additional normal force acting on them resulting in additional frictional force.

On the other hand, at the rear brakes (blue line), negative or upward force is experienced for a period. This results in different effects for each of the systems. For the clamps, this scenario adds more normal force to the bottom brake pads at the rear module.

4.3.3 Variation of Braking Force with Time

As with the deceleration of the pod, the braking force also follows a non-linear, exponential growth due to the emergency nature of the system. The braking force is completely affected by friction that is applied suddenly under the weight of the pod, resulting in braking forces in kilonewtons. The braking force is calculated as mentioned before as the difference between magnetic lift and total applied frictional force. The braking force is plotted from 0 seconds all the way to when the pod achieves a complete stop (In our model's case, t = 0.093 seconds) with a peak braking force of 5.3025 kN.

4.4 Variation of Normal Force with Time (Front and Back Braking Systems)

Before analysing this section, it must be noted that the 2 bottom brake pads were coupled for the sake of simulation in the code and therefore are assumed to be a single bottom pad for each system.

The graphs above depict variation of normal force between the upper and lower brake pads for the front and rear braking systems. The loading variation between the upper and lower brake pads gives insight into the rocking motion experienced by the hyperloop pod in the case of an emergency braking situation. This rocking motion is a result of the pod's inertia during motion. The pod tends to remain in a state of motion, resisting the stopping force, resulting in a greater force being applied to the top brake

pad of the front braking system. During this process, as the whole pod is a rigid body, the rear bottom of the pod would be raised resulting in a force exerted by the rear bottom brake pad on the I-Beam as well.

One possible concern when analysing these graphs is the lack of normal force exerted by the front bottom brake pad and rear top brake pads upon the pod's stopping or once it has slowed down enough. This is because once the pod comes to a stop, the time during which force is exerted by these 2 pads on the I-Beam is too short to produce a massive visual shift in the plot.

4.4.1 Variation of Braking Pad Volume and Height with Time

The brake pad volume and height wear plots are here to understand a general trend when it comes to wear and is not a definitive solution as further research needs to be conducted on viable brake pad materials. For the sake of these simulations, the brake pad material analysed is an aluminium composite with frictional factor 1 and wear coefficient 1.73×10^{-13} which is very low, implying low wear rates.

These graphs are comparing the top and bottom brake pad volume wear during the braking process. The plots were classified for top and bottom brake pads as opposed to front and rear due to the large difference in brake pad volume between the top and bottom pads.

The plot is in accordance with the rocking motion observed in the variation of normal force graphs as can be seen from the greatest volume wear being in the case of the front top brake pad (red line) and the rear bottom brake pad (green).

These plots unlike the volume plots, are split between the front and rear brake pads. Similarly to the volume plots however, the rocking motion can also be noticed as seen by the top brake pad suffering more wear in the front than the rear and the bottom brake pad suffering more wear in the rear than in the front.

Overall, the wear on the brake pads with the current brake pad material is negligible as it is only in the degree of 10^{-5}.

4.4.2 Spring Selection Graph

This graph compares springs by assessing force provided by springs with varying spring constants and spring lengths (compressed and extended) with respect to the stopping distance that needs to be achieved. This graph was used in the 2022-2023 academic year (in Braking_Code_v2) to determine the ideal springs for use when building the small-scale hyperloop pod. While the spring parameters and options chosen from the catalogue are outdated, these parameters can be adjusted in the code to compare various other springs and determine the best option.

4.5 Design for Manufacture: Braking

4.5.1 Overview

The hyperloop braking system comprises multiple interconnected components designed to operate under high loads and extreme conditions. Below is a summary of the materials and components used:

Braking system consists of asbestos brake pads supported with the attachment plate and brackets made out of aluminium which are connected to the chassis. The brakes are mounted around the I-Beam track and activated with a pneumatic actuator which is connected to the brake pad holder via a connecting rod. There are three brake pads; one on the top of I-Beam and two on the bottom side of the I-Beam flange. These are guided by guide rails made of stainless steel. When the brakes are actuated the brake pads encounter the I-Beam and the kinetic energy of the pod is converted into heat which helps in slowing it down.

Aluminium 6061-T6 is highly suitable for the Hyperloop brake system due to its excellent strength-to-weight ratio and corrosion resistance. As a lightweight material, it helps reduce the overall mass of the braking system, which is crucial for energy efficiency in high-speed transport like the Hyperloop. The high tensile strength and rigidity of 6061-T6 ensure it can handle the intense forces during braking without failure. Its weldability and machinability allow for efficient manufacturing of brake components with complex geometries. The material's corrosion resistance, especially in anodized form, ensures longevity even in harsh operating environments. Additionally, its thermal conductivity allows for effective heat dissipation during braking, preventing overheating. These attributes make aluminium 6061-T6 a strong, lightweight, and reliable material for the demanding requirements of the Hyperloop brake system.(5)

Stainless steel grades 304 and 316 are ideal for the Hyperloop brake system due to their exceptional corrosion resistance, strength, and durability. Grade 304 offers good resistance to a wide range of environments, while Grade 316, with added molybdenum, is more resistant to chloride-based corrosion, making it ideal for high-stress, moisture-prone environments like the braking system. Both grades exhibit high tensile and yield strengths, ensuring the material can withstand the significant forces during braking. Additionally, their weldability allows for easy fabrication of complex brake components. Stainless steel's high-temperature resistance is critical for brake systems that experience elevated temperatures during deceleration. The combination of these properties makes stainless steel a reliable and durable choice for ensuring the structural integrity and performance of the brake system over time (6).

4.5.2 Manufacturing Process Overview

All the photos are in the appendix.

4.5.3 Primary Manufacturing Methods

1. **Waterjet Cutting:** Used for precision machining of components like the attachment plate, bottom plates, and brake pad holder. Waterjet cutting ensures accurate shapes, minimizes thermal distortion, and allows complex geometries without requiring secondary finishing (7).

2. **Drilling:** Nominal diameters of the holes are created using a conventional drilling machine, providing efficiency and reliability in hole-making.

3. **Lathe Turning:** Used for components such as the rails and bearing housings to achieve precise dimensions, surface finishes, and threading (8).

Part No.	Part Name	Quantity Per System	Total	Material
1	Attachment Plate	1	2	Al-6061 T6
2	Bottom Brake Pad	2	4	Al-6061 T6
3	Bottom Plate	2	4	Al-6061 T6
4	Brake Pad	1	2	Al-6061 T6
5	Brake Pad Holder	1	2	Al-6061 T6
6	L Bracket (Short)	2	4	Al-6061 T6
7	L Bracket (Long)	2	4	Al-6061 T6
8	Side Plate	2	4	Al-6061 T6
9	Rail	2	4	Stainless Steel
10	Top Plate	1	2	Al-6061 T6
11	Nyloc Nut (M10)	4	8	Off-the-Shelf
12	Igus Bearing	6	12	Off-the-Shelf
13	Final Spring	2	4	Off-the-Shelf
14	Shaft Collar	2	4	Off-the-Shelf
15	Connecting Rod	1	2	Al-6061 T6

Table 14: Parts List Braking

4. **Tungsten Argon Gas (TIG) Welding:** Provides clean, strong, and precise welds for components like the bearing housings and side plates. TIG welding is especially advantageous for aluminum, ensuring minimal warping and high joint strength.

5. **Off-the-Shelf Components:** Bearings, nuts, and springs are pre-fabricated for easy assembly and cost efficiency.

4.5.4 DFM Principles Applied

Category	Details
Simplification	Components are designed with standardized geometries to simplify machining and assembly.
	Off-the-shelf components reduce the need for custom manufacturing.
Material Optimization	Use of recyclable and readily available materials like Al-6061 T6.
	Stainless steel provides durability for high-wear parts.
Ease of Assembly	Clear assembly instructions reduce labor time and errors.
	Modular design facilitates repair and maintenance.
Cost and Risk Analysis	
Cost Breakdown	**Material Costs:** Approximately 60% of the total cost.

Category	Details
	Labor Costs: 25% of the total cost, focused on machining and assembly.
	Tooling Costs: 15%, largely for CNC setup, waterjet cutting, and TIG welding equipment.
Potential Risks	**Tolerances:** Misalignment of rails can affect system functionality.
	Material Availability: Any supply chain disruption for Al-6061 T6 or stainless steel.
	Assembly Errors: Incorrect alignment of components during welding or assembly.
Mitigation Strategies	Regular quality checks during machining and assembly.
	Use of jigs and fixtures for precise alignment.
	Vendor evaluation for reliable material sourcing.
Sustainability Considerations	
	Use of recyclable materials like Al-6061 T6.
	Optimization of machining processes to minimize material waste.
	Modular design supports reusability and ease of repair, extending system lifecycle.

5 Pressurized Systems

5.1 Overview

Pressurized systems are employed in both the braking and suspension subsystems due to their critical need for fail-safe operation. Pneumatic systems, known for their safety and reliability, were selected to meet these requirements. Both pneumatic circuits share essential components, with the suspension circuit incorporating a larger actuator to accommodate the greater force required for deployment, as it must bear the full weight of the pod. The implementation of these systems is carried out in collaboration with FESTO, the primary supplier of pneumatic components. In terms of other design choices: Pneumatic actuators were selected, as these will best account for the possible vibrations of the suspension

5.2 Parts list and Specifications

The pneumatic part list for the braking component

Component	Manufacturing Process
Attachment Plate	Cut to shape using waterjet cutting for high precision and minimal thermal stress. Drill holes for mountings and fasteners using a conventional drilling machine. Bearing housings are turned on a lathe and welded to the plate using TIG welding.
Bottom Brake Pad	Profiled using waterjet cutting. Finished with surface treatments for smoothness and corrosion resistance.
Bottom Plate	Fabricated through waterjet cutting for accurate dimensions. Holes drilled to specifications for assembly compatibility.
Top Brake Pad	Machined via waterjet cutting to achieve the intricate shape. Surface finishing for friction optimization.
Brake Pad Holder	Waterjet cutting used for precise shape creation. Drilled for accommodating bearings and fasteners.
L Brackets (Short and Long)	Divided into short and long brackets and manufactured using waterjet cutting from Al-6061 T6 sheets. Holes drilled for mounting with a drilling machine for nominal diameter.
Side Plates	Cut using waterjet cutting for precise dimensions. Welded to the top plate using TIG welding.
Rails	Raw material is cut using a hacksaw to the required size. Turned on a lathe to achieve precise length and diameter. Screw threads are also turned on a lathe for fastening.
Top Plate	Precision cut with waterjet technology. Bearing housings turned on a lathe and welded to the plate using TIG welding. TIG welding used to attach side plates.
Connecting Rod	Machined from Al-6061 T6 using a CNC lathe. Turned on a lathe to ensure precise diameter and surface finish. Drilled and tapped for assembly.
Off-the-Shelf Components	Bearings, springs, Nyloc nuts, and shaft collars are pre-fabricated and sourced for assembly.

Table 15: Component-Specific Manufacturing Processes

Specification	Value
Maximum Pressure [bar]	15
Operating Pressure [bar]	10

Table 17: Pneumatic system parameters.

Component	Number	Specifications	Reference	Price (GBP)
Actuator	2	Diameter: 32mm, Stroke: 40mm, Connection: Male thread, Double acting	ADN-S-40-5-I-P-A	67.24
Solenoid Valve	2	Connection: G1/8, Length: 20mm, Normally closed, Polymer housing, 3/2	VUVS-L20-M32C-AD-G18-U1-F7-1C1	71.33
Pressure Regulator	1	Connection: G1/4	MS4-LFR-1/8-D7-ERM-AS	68.98
Silencer	2	Connection: G1/8	UC-1/8	6.32

Component	**Number**	**Specifications**	**Reference**	**Price (EUR)**
Plastic Tubing	TBD	Outer Diameter: 4mm, Wall Thickness: 0.75mm	PUN-H-4X0.75-BL	TBD
T Junction	1	Airflow: “1/8”	QSLV2-1/8-4	TBD
Air Tank	1	Volume: 0.1 L	CRVZS-0,1	TBD

Table 18: Pneumatic parts list.

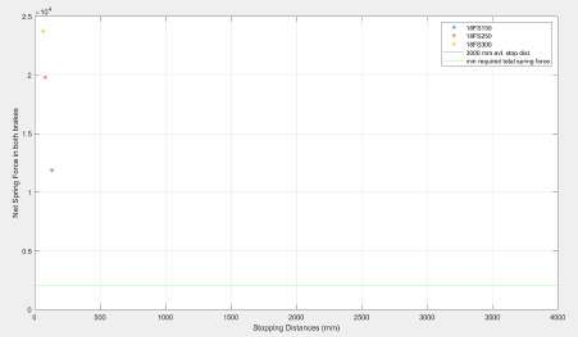

Figure 9: Spring selection Braking.

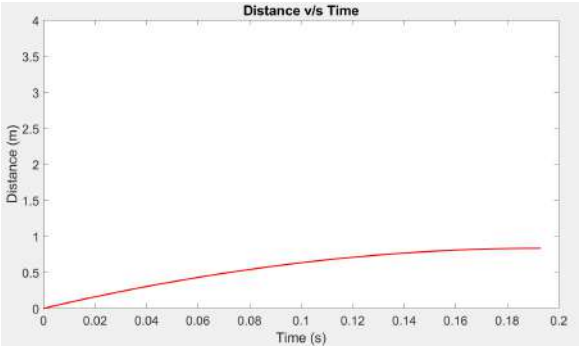

Figure 10: Distance vs time Braking.

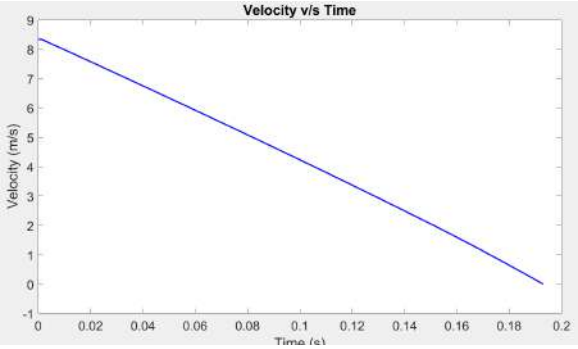

Figure 11: Velocity vs time Braking.

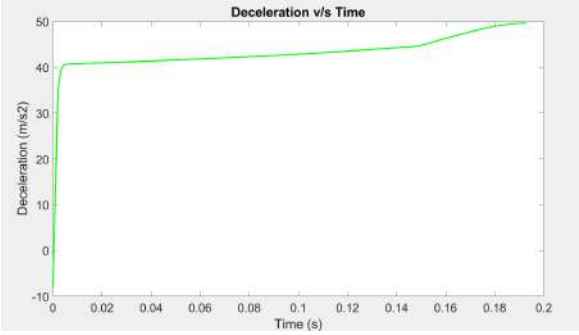

Figure 12: Deceleration vs time Braking.

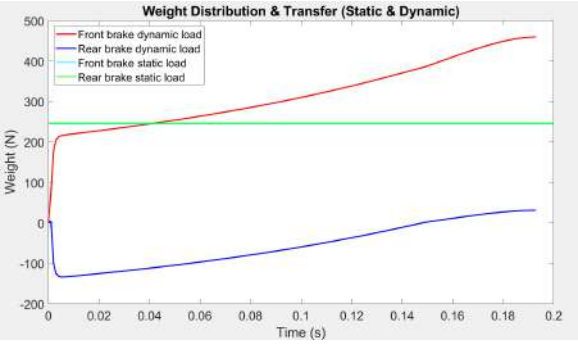

Figure 13: Weight distribution of brakes.

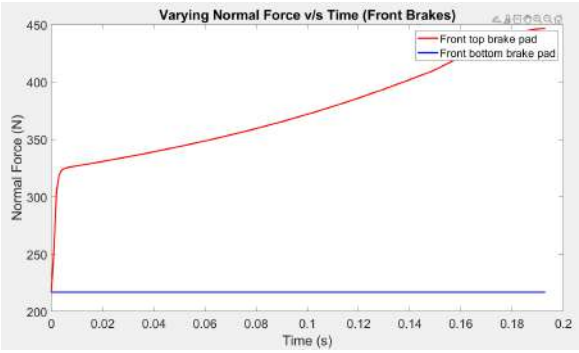

Figure 14: Braking force vs time.

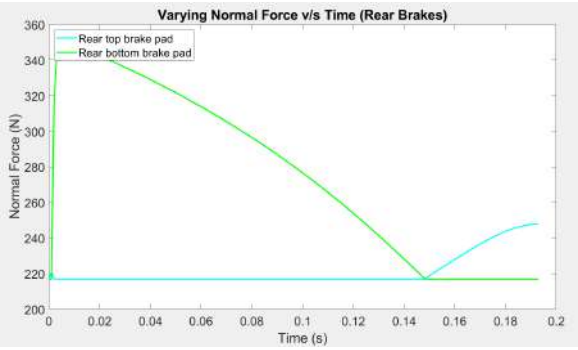

Figure 15: Normal force front brakes.

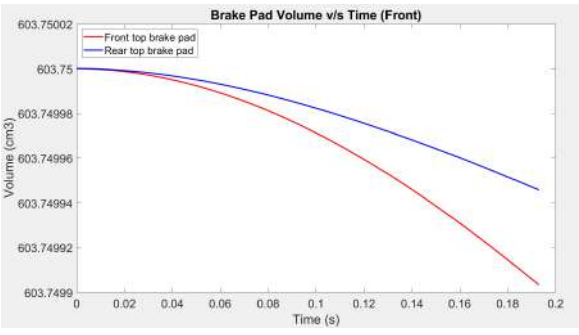

Figure 16: Normal force back brake.

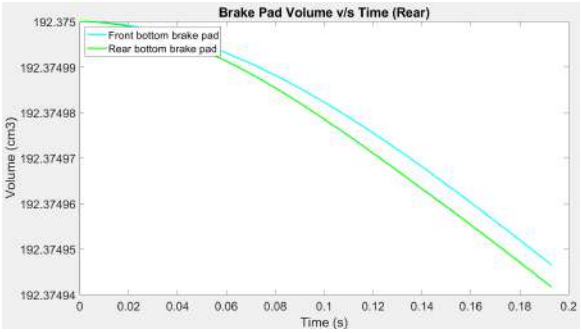

Figure 17: Brake pad volume bottom pads.

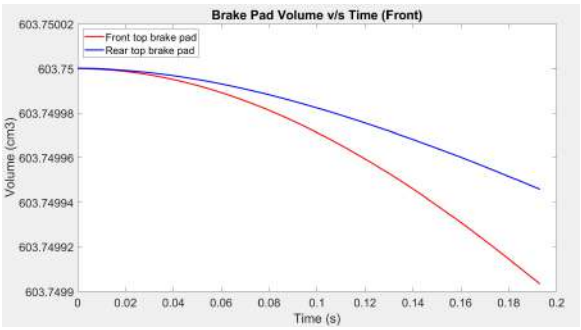

Figure 18: Brake pad volume front.

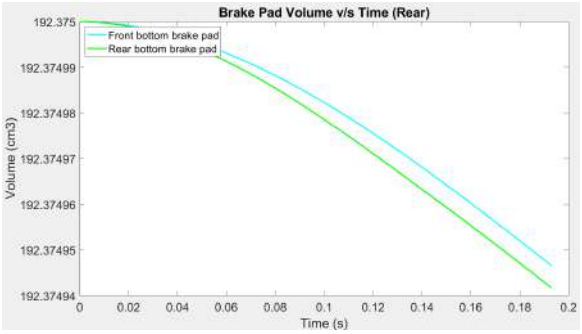

Figure 19: Brake pad volume Rear.

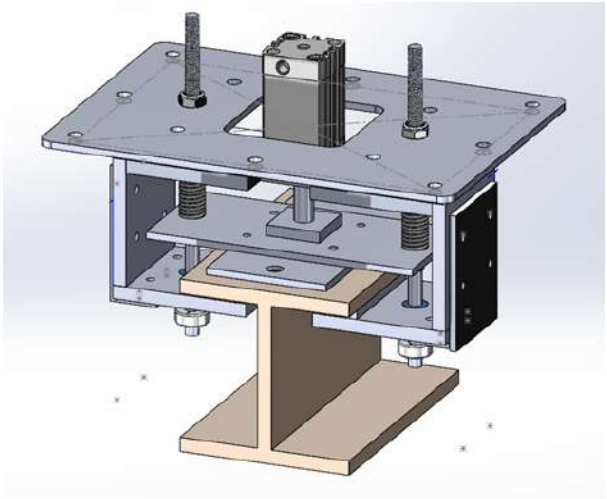

Figure 20: Braking System Overview

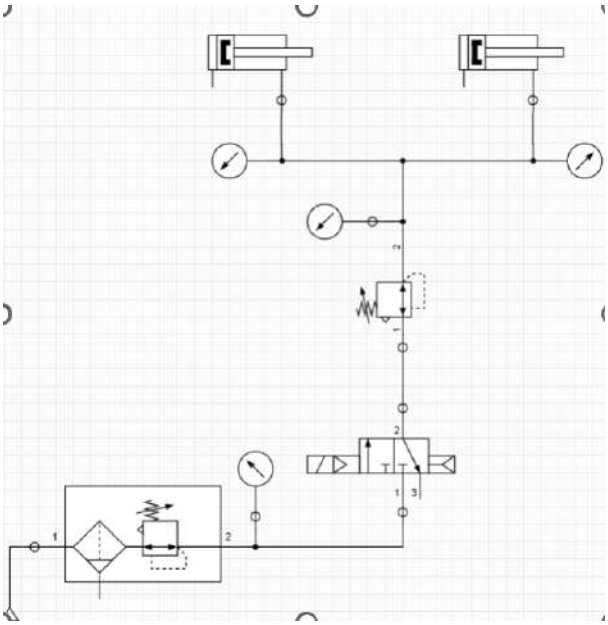

Figure 21: Pneumatic circuit

6 Suspension

6.1 Overview

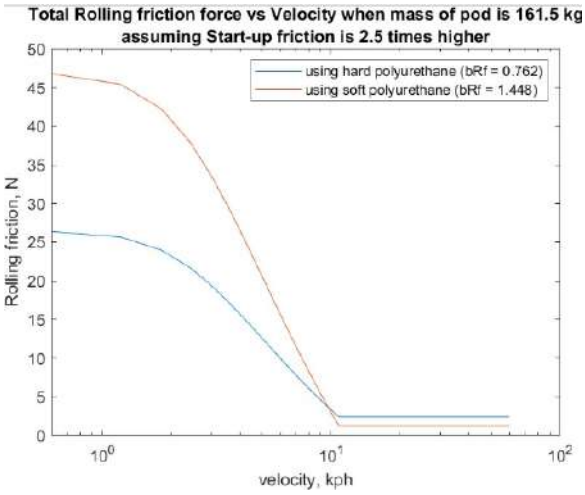

Figure 22: Rolling friction force vs velocity of the pod.

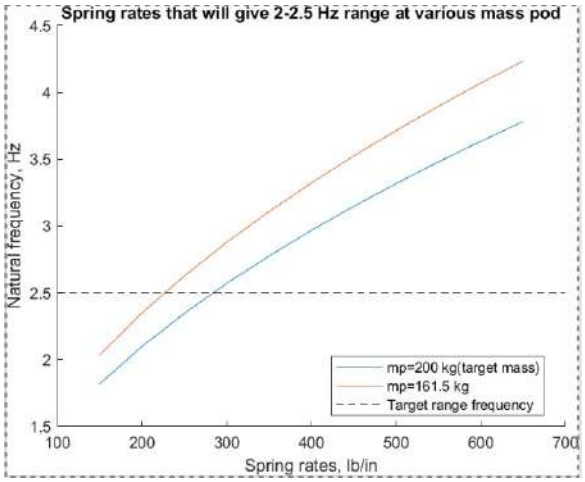

Figure 23: Spring rates for given mass of pod.

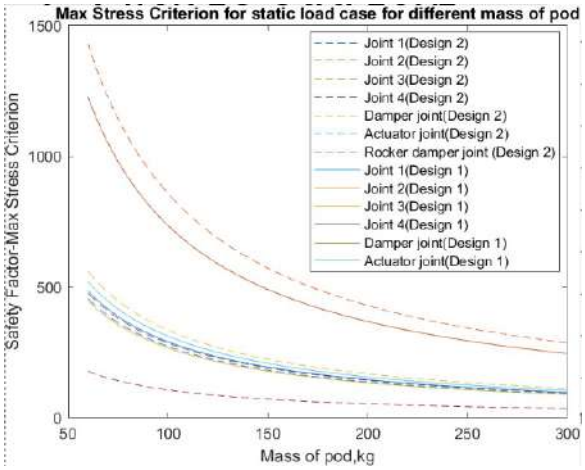

Figure 24: Static load case for mass of pod.

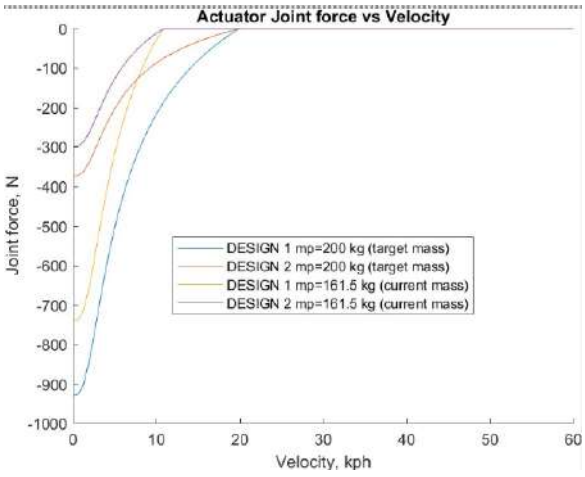

Figure 25: Actuator force vs velocity.

Based on the data presented at the 2022 EHW conference, critical decisions were made regarding the selection of wheels and the suspension system. These decisions were informed by the original metrics used in the suspension design. The metrics took into account several key factors:

Mass: This corresponds to the total weight of the pod, including projections for future iterations such as the addition of a battery pack.

Spring Setup: The weight calculations were used to calibrate the springs, determining the appropriate pound-per-inch value for optimal performance.

These considerations were crucial in developing a suspension system that could effectively support the pod's weight while providing the necessary responsiveness and stability. The wheel selection was similarly influenced by these factors, ensuring compatibility with the overall suspension design and the pod's weight distribution.

By integrating these metrics into the decision-making process, the team aimed to create a more robust and efficient suspension system, capable of handling the pod's current specifications while also accommodating potential future modifications. This forward-thinking approach demonstrates a commitment to scalability and adaptability in the pod's design, which are critical factors in the rapidly evolving field of hyperloop technology.

6.1.1 Vertical Suspension

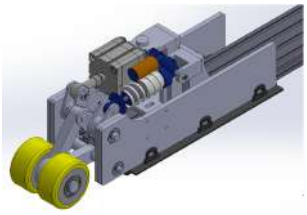

Figure 26: Top suspension design.

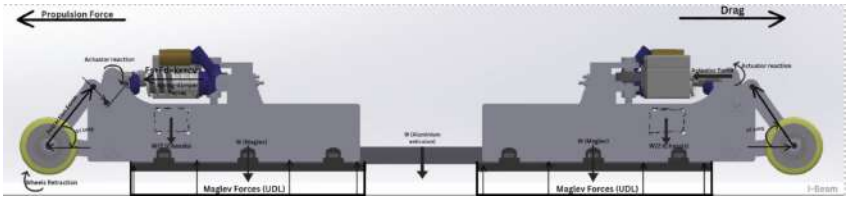

Figure 27: FBD of top suspension.

The focus of the vertical suspension system will be on any vibrations in the vertical direction. To mitigate these vibrations, the system consists of Ohlins TTX25 MkII adjustable spring dampers, pneumatic linear actuators and rocker arms to help translate vertical displacement of the wheels to horizontal displacement of the spring or damper. There will be two vertical suspensions on the front and rear ends of the pod for stability. To determine an optimal motion ratio, we will need to consider that the total wheel travel cannot exceed 15mm, the maximum ride height. This optimal motion ratio will then help determine the dimensions for the rocker arm. The largest forces the pod will experience is the braking force, where there will also be the largest rate of weight transfer of the vehicle. Therefore, the vertical suspension must regulate this rate of weight transfer and prevent the pod from bottoming out during the emergency braking phase, mitigating any damage to the magnetic levitation ski. The vertical suspension also includes a pneumatic linear actuator which helps retract and extend the wheels back on to the track to accommodate for the levitation phase. If the pneumatic linear actuator was to fail in any way, the pneumatic actuator as well as the pre compressed spring damper will default to an extended state, which lower the wheels to ensure the magnetic levitation ski is not damaged. As the wheel is extended during the post levitation phase, there will also be vibrations involved once the wheels touch the track. The spring damper system will dampen any of these vibrations and could act as a safety feature in case the wheels hit the I-beam with a great amount of force.

A key part to the vertical suspension system is the actuator, which is the primary mechanism responsible for retracting the landing gear at the beginning of levitation and at the end of landing. It must oppose the forces from the spring during retraction and support the weight of the wheels and components connecting the wheels to the actuator and damper. This requires significant force, along with additional features to ensure the stability of the wheel during takeoff and landing, as well as a controlled, consistent speed. Actuators possess all these attributes and purchasing them from a trusted company ensures reliability. Producing or manufacturing a makeshift actuator in-house would incur higher costs

due to iterative design, manufacturing, and testing requirements. Such parts are generally purchased to allow resources and time to be allocated to other crucial components that need to be manufactured in-house. Purchasing actuators increases system safety and removes the need for frequent replacement, as they are typically durable.

6.1.2 Side Suspension

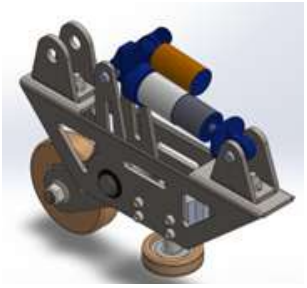

Figure 28: Side Suspension.

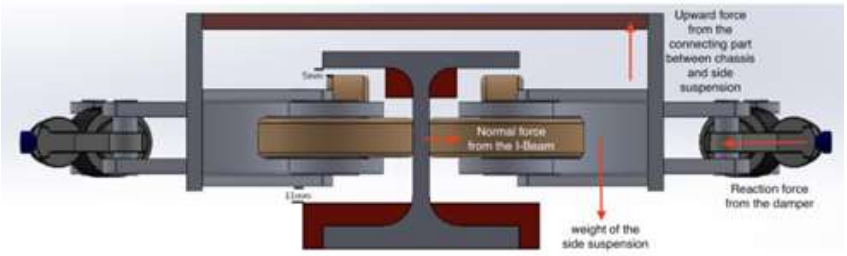

Figure 29: FBD of side suspension.

The side suspension will be focusing on keeping the pod straight and damping vibrations acting laterally. Four of these systems will be placed at each corner of the chassis reducing the motion of the pod in the yaw direction, guiding the pod from the beginning to end of the journey as well as causing a grip effect due to the springs mounted that sets the clamp force on these four corners. Each system is provided with two wheels, the larger one will be the wheel interacting with the mid-section of the I-beam and attached to the rocker plate, whereas the small wheel acts as a fail safe for the pod especially for the braking system, in order to prevent it from hitting the I beam and in the case of levitation exceeding the desired height, in which the small wheel will roll along the underside of the top flange of the I-beam. They are also important in ensuring the pod maintains a maximum gap height in the worst case scenario should the brakes not engage in time, the vertical wheels will impact under the flange of the I-beam, guiding the pod. With the use of a damper attached to a rocker plate (both are designed, chosen and adjusted to give appropriate damping ratio and motion ratio to ensure most of the forces from vibrations are transferred to the damper) the side suspension dampens these resonant forces from magnetic levitation system in the yaw direction. The side suspension damper acts as a compliant element as opposed to being a rigid system, as in the unlikely event of the pod veering off to the side at a high speed, if the system is rigid, it will produce a large amount of stress on the side suspension and joints, which can lead to failure.

The main component to any suspension system is the damper. Damper manufacturers specialize in producing these components and have extensive knowledge and experience in damper design, materials, and manufacturing processes. Those commercial dampers are reliable and function well under operating situations since they have been tested and validated in a variety of applications. Additionally, to save time and money, the team bought off-the-shelf dampers instead of having them manufactured for this particular application. Working alongside the damper is the spring, playing a critical role in driving the overall mechanism of the system. It is therefore essential to ensure they meet all performance

and reliability requirements, minimizing the risk of unexpected failure. Currently, a wide range of reliable, standardized spring systems are available in the market, having undergone rigorous testing and certification by suppliers. Given the significant cost, time, and effort required to design, manufacture, and perform extensive post-testing on house-made springs, we have opted to select and purchase springs with well-documented mechanical properties and failure characteristics from supplier catalogs.

6.2 Specifications

The following table details the mass breakdown of various side suspension components:

Part Name	Amount Needed	Mass (g) [Individual]	Total Mass (g)
L Linkage	24	0.138	3.312
Wheel Axle	2	190.99	381.98
Bottom L Linkage Sleeve	4	24.439	97.756
Side Plate Right	2	1482.89	2965.78
Side Plate Left	2	1482.89	2965.78
Actuator Support Clevis	2	335.269	670.538
Damper Bracket Clevis	2	152.431	304.862
Damper Clevis Spacer	4	1.742	6.968
Damper Spacer	8	0.84	6.72
Actuator Clevis Spacer Cam Shaft	4	1.55	6.2
Actuator Clevis Spacer Back	4	1.858	7.432
Wheels	4	1560	6240
Top Shaft	2	113.392	226.784
Damper Adapter Plates	?		
Actuator Adapter Plates	?		
Cam Shaft Bracket Base	4		
L Linkage Bracket Base	2		
Actuator Bracket Side	4	110.832	443.328
Damper Bracket Side	4	105.44	421.76
L Linkage Bracket Side	4	105.28	421.12
Actuator	2	921	1842
Swivel Flange SNCS-63	2	815	1630
Rod Eye SGS-M12x1,25	2	130	260
Actuator Triangular Ribbed Support	2	709.552	1419.104
Damper Triangular Ribbed Support	2	619.56	1239.12
Bottom L Linkage Shaft	2	97.721	195.442
Aluminium Extrusion	1	3000	3000
Damper	2	394	788
TOTAL			**25172.906**

Table 19: Top Suspension Component Mass Breakdown

Part Name	Amount Needed	Mass (g) [Individual]	Total Mass (g)
Guide Wheel Assembly Body	4	1612.44	6449.76
Front Chassis Bracket	4	282.57	1130.28
Rear Chassis Bracket	4	253.49	1013.96
Main Wheel Shaft	4	203.17	812.68
Rocker Swing Arm	4	302.75	1211.00
Rocker Shaft	4	152.63	610.52
Wheel Shaft Secondary	4	164.63	658.52
Vertical Wheel Shaft Housing	4	114.60	458.40
Vertical Wheel	2	640.00	1280.00
Main Wheel	2	500.00	1000.00
Damper	4	394.00	1576.00
Damper Rocker Spacer	80	0.84	67.20
Damper Bracket Spacer	80	0.66	52.80
TOTAL			**16774.05**

Table 20: Side Suspension Component Mass Breakdown

The following table details the mass breakdown of various top suspension components:

6.3 Budget and Timeline

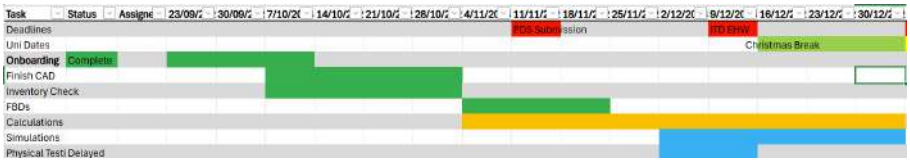

Figure 30: Gantt Chart Suspension. Sem-1

Figure 31: Gantt Chart Suspension. Sem-2

Component	Cost (£)
Complete Suspension System	1,100
Fasteners	749
Aluminium Extrusion	120
Rollers	74
Bearings	291
Total	**2,334**

Table 21: Suspension System Cost Breakdown

The costs listed include components obtained through sponsorship, which contributed to reducing the overall expenditure.

6.4 Design for Manufacture: Suspension

Basic Description The suspension system is broken down into two major components, they are the side suspension systems and the top suspension system. The side suspension is further broken down into two components that are the right-hand side and left-hand side suspension systems. Each individual side suspension system comprises of a compression spring and damper combinational unit. The top suspension unit is additionally fitted with an actuator to maintain contact throughout the pod's traversal. **Top Suspension Description (Primarirly Aluminium 6061 T-6 based)** The top suspension system is designed for optimal and constant contact with the horizontal top surface of the I beam. The construction of this unit system comprises of a 3-bar linkage coupled with a roller wheel which maintains contact with the I beam surface. To ensure lasting contact, the actuator is used to linearly expand the system until sufficient contact is achieved. The compression spring and damper unit provides the necessary freedom for the suspension unit to travel across a certain range during high-speed traversal. The 3-bar assembly consists of a fixed link constrained to the pods chassis, a crank shaft (that supports the spring-damper system and the actuator while transferring motion to the other linkages) and an L-shaped rocker to transfer the subsequent motion to the rollers. **Side Suspension Description(Primarirly Mild Steel**

based) The side suspension system is designed with the consideration for contact towards the vertical thin cross-section and the underside of the horizontal section of the I beam. The main assembly comprises of a 3-bar mechanism with a fixed link, a crank (with an integrated spring-damper system) and a pivot rocker with the fulcrum point located on the fixed link, with the end rocker supporting a roller. This roller supports and maintains contact to vertical thin section of the I beam. A roller constrained via a bearing to the fixed linkage on the 3-bar mechanism provides contact to the underside of the horizonal section of the I beam. Two such complete units are assembled and placed opposite each other to balance out the residual forces and provide dual support to the pod during traversal. In total there are four side suspension assembly, two opposite each other and spaced appropriately across the pods length. **DFM Model** The Design for Manufacturing model has been developed taking inro consideration conventional design principles and manufacturing techniques available at the team's disposal. Manufacturing methods that include the following: CNC lathe, CNC milling, water jet cutting, laser cutting and TAG welding have been unutilized.

Part Name	**Amount Needed**	**Mass (g) [Individual]**	**Total Mass (g)**
Guide Wheel Assembly Body	4	1612.441	6449.764
Front Chassis Bracket	4	282.57	1130.28
Rear Chassis Bracket	4	253.49	1013.96
Main Wheel Shaft	4	203.17	812.68
Rocker Swing Arm	4	302.758	1211.032
Rocker Shaft	4	152.63	610.52
Wheel Shaft Secondary	4	164.63	658.52
Vertical Wheel Shaft Housing	4	161.14	644.56
Vertical Wheel	4	160	640
Main Wheel	4	500	2000
Damper	4	394	1576
Damper Rocker Spacer	8	1	8
Damper Spacer	16	0.841	13.456
Damper Bracket Spacer	8	0.66	5.28
TOTAL			**16774.052**

Table 22: Component Mass Breakdown Side Suspension

6.4.1 Design for Manufacturability (DFM) Principles

Material Selection Aluminium sheets were chosen for their lightweight, corrosion resistance, and ease of machining, ensuring manufacturability and performance. Stainless steel rods were selected for components requiring high strength and durability under mechanical stress.

Process Simplification Water jet machining minimizes the number of secondary processes by providing clean and precise cuts. Standardized use of CNC lathe operations for rod components ensures repeatability and accuracy.

Assembly-Friendly Design Holes and slots are accurately machined to facilitate alignment and minimize errors during assembly. Components are designed with tolerances that allow for easy fitment without post-processing.

Waste Reduction Water jet machining reduces material waste due to its precise cutting capability.

Part Name	Amount Needed	Mass (g) [Individual]	Total Mass (g)
L Linkage	2	400.13	800.26
Wheel Axle	2	190.99	381.98
Bottom L Linkage Sleeve	4	24.43	97.72
Side Plate Right	2	1482.89	2965.78
Side Plate Left	2	1482.89	2965.78
Actuator Support Clevis	2	335.269	670.538
Damper Bracket Clevis	2	152.431	304.862
Damper Clevis Spacer	4	1.742	6.968
Damper Spacer	8	0.841	6.728
Actuator Clevis Spacer Cam Shaft	4	1.55	6.2
Actuator Clevis Spacer Back	4	1.858	7.432
Wheels	4	1560	6240
Top Shaft	2	113.392	226.784
Cam Shaft Bracket Base	4		
L Linkage Bracket Base	2		
Actuator Bracket Side	4	110.832	443.328
Damper Bracket Side	4	105.44	421.76
L Linkage Bracket Side	4	105.28	421.12
Actuator	2	921	1842
Swivel Flange SNCS-63	2	281	562
Rod Eye SGS-M12x1,25	2	130	260
Actuator Triangular Ribbed Support	2	709.552	1419.104
Damper Triangular Ribbed Support	2	619.56	1239.12
Bottom L Linkage Shaft	2	47.721	95.442
Aluminium Extrusion	1	3000	3000
Damper	2	394	788
TOTAL			**25172.906**

Table 23: Component Mass Breakdown Top Suspension

Efficient nesting of parts during sheet cutting further minimizes scrap material.

Tooling and Fixture Efficiency Minimal reliance on custom tooling by leveraging standard machining processes like CNC turning and water jet cutting. Parts are designed to be easily clamped and machined without complex fixtures.

6.5 Conclusion

The hyperloop suspension system is designed with precision and efficiency to meet the unique demands of high-speed transportation. This report demonstrates that the components, including side and top suspensions, are optimized for manufacturability by employing Design for Manufacturability (DFM) principles. Aluminium sheets and stainless-steel rods were selected for their material properties, ensuring lightweight yet robust construction. Advanced manufacturing techniques like water jet machining and CNC lathe machining were chosen to minimize material waste, maintain tight tolerances, and enhance process efficiency.

The cost analysis confirms that material and process selections strike a balance between performance and economic feasibility. Risk assessments addressed potential challenges, such as supply chain delays and manufacturing tolerances, with mitigations like backup machining options and supplier networks. By adhering to DFM principles, the design promotes waste reduction, assembly efficiency, and process

Table 24: Manufacturing Details of Chassis Components

Component	**Material**	**Manufacturing Process**	**Explanation**
Guide Wheel Assembly Body	Aluminium (Sheet)	Water Jet Machining, Sheet Metal Bending	Water jet cutting avoids heat-affected zones, preventing warping. Bending ensures accurate shaping.
Front & Rear Chassis Brackets	Aluminium (Sheet)	Water Jet Machining, Sheet Metal Bending	Water jet cutting maintains surface finish and strength. Bending forms strong brackets with minimal deformation.
Main Wheel Shaft	Stainless Steel (Rod)	CNC Lathe (Step Turning, Thread Cutting)	CNC lathe ensures precise tolerances and threading for critical interfacing components.
Rocker Swing Arm	Aluminium (Sheet)	Water Jet Machining	Clean, thermally-neutral cuts through thick aluminium ensure strength under load.
L-Linkage	Aluminium Plate	Water Jet Machining	Provides precision cuts without microcracks or thermal stresses, ideal for structural linkages.
Wheel Axle	Stainless Steel (Rod)	CNC Lathe (Step Turning, Chamfering)	Provides dimensional accuracy and chamfering for assembly and load handling.
Bottom L Linkage Sleeve	Stainless Steel (Rod)	CNC Lathe (Turning, Nominal Diameter Drilling)	Ensures internal and external precision for alignment and interfacing.
Side Plates (Right & Left)	Aluminium (Sheet)	Water Jet Machining, Drilling	Water jet cutting maintains strength and accuracy; drilling ensures mounting compatibility.
Fasteners	Standard (Outsourced)	Procured	Purchased as off-the-shelf items to reduce production time and cost.

simplification, ensuring a reliable, scalable, and cost-effective suspension system for hyperloop technology.

Table 25: Risk Analysis

Category	**Details**
Material Risks	• Water jet machining prevents distortion in aluminium. • Tool wear in stainless steel machining managed by using high-grade tools and optimal speeds.
Process Risks	• CNC machining requires tight tolerance control to avoid rejections. • Downtime in water jet machines may delay production; alternate machining methods should be prepared.
Assembly Risks	• Misalignment reduced through tight tolerance slots/holes and proper fixturing. • Training assembly personnel helps mitigate human error.
Supply Chain Risks	• Delays in fastener/raw material sourcing can disrupt timelines. Reliable suppliers reduce this risk.

7 Propulsion

7.1 Overview

Parameter	Value
Average Maximum acceleration	4.8 [m/s]
Operating voltage	50 [V]
Nominal current	4.06 A[A]
Maximum current	278 [A]
Maximum power	780 [W]

Table 26: Traction System Specifications

Battery-powered electric motors were selected due to current budget limitations, which postponed the acquisition of a Linear Induction Motor (LIM) system. This approach, however, enables the team to invest in a higher-quality and more effective LIM system in the future, rather than settling for a less capable option within this year's budget. Motor calculations have been conducted for various combinations of pod weight and speed to optimize performance, focusing on parameters such as torque, power output, and energy efficiency under varying load conditions. The motor specifications are as follows: Maxon Brushless DC motor, 260 W, 48 V dc, 964 mNm (nominal torque), 13100 mNm (stall torque), 5000 rpm and 10 mm shaft diameter. This was based on calculations of the specific velocity requirement for the Maglev system to generate sufficient lift to levitate the pod. This provided a basis to design a battery pack that supplies 454Wh, 48 V dc, 90 A discharge current, constructed using Sony/Murata Li1x3pVTC6 Li-ion building blocks. 14 units of the blocks will be used for one battery pack.

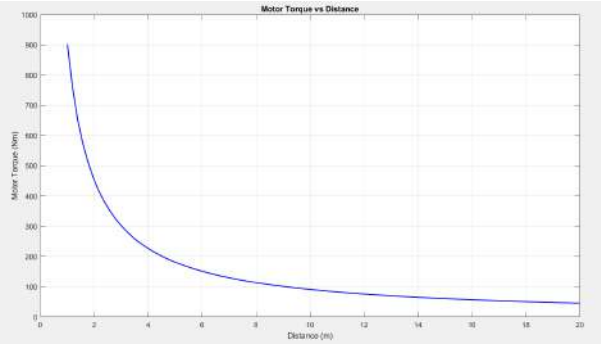

Figure 32: Magnetic levitation and velocity relation.

7.2 Inspiration

The inspiration to utilize brushless DC motors initially came from motorised skateboards and e-bikes, as these systems use them for propulsion. As LIM development and construction was a serious financial and logistical challenge, especially because it is difficult to acquire the small quantities of electrical steel needed for the LIM core, a rotary motor proved to be a much simpler alternative. BLDC motors were chosen over other motor types due to the high starting torques required to accelerate the pod to top speed within a short track length, and high efficiency which reduces energy loss and hence extends battery life.

7.3 Specifications

Motor Torque Calculation

$$T_m = mR_w \left[\frac{v^2 - u^2}{2s} + g(r_r) \right]$$

Parameter	Value
Mass (m)	100 kg
Wheel Radius (R_w)	62.5 mm
Final Velocity (v)	6 m/s
Initial Velocity (u)	0 m/s
Acceleration Distance (s)	8 m
Acceleration due to Gravity (g)	9.81 m/s^2
Rolling Resistance (r_r)	0.009
Gear Ratio (GR)	1
Number of Motors (N)	4

Table 27: Parameters and their Values

The motor torque values obtained were compared against the plot in Figure 31, which guided the team in determining the required motor specifications. This, in turn, influenced the voltage requirements and informed battery selection. The Matlab code used is provided in the appendix.

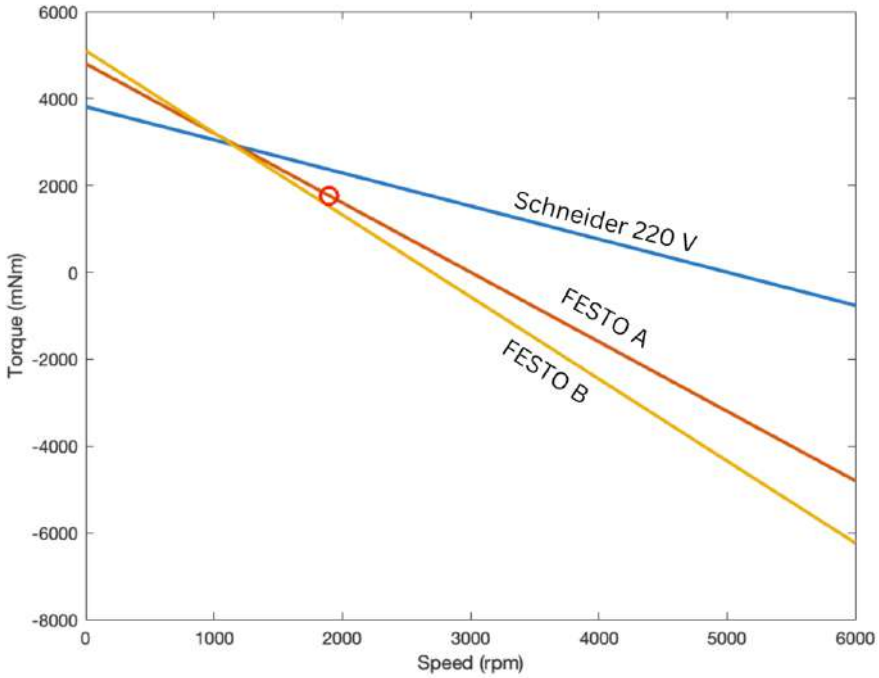

Figure 33: Different motor boundary conditions.

7.4 Timeline

Propulsion system development was separated into two major streams: mechanical and electrical. While the mechanical stream focused on designing structural components such as the motor mounts and conducting FEA analysis, the electrical stream worked on understanding LIM theory for future work, such

Figure 34: Gantt Chart Propulsion.

as construction parameters and power electronic control, as well as battery pack design.

7.5 Challenges

The motor selection process presented a significant engineering challenge. Several critical factors had to be carefully balanced:

- **Torque and RPM:** The motor needed to deliver sufficient torque to meet the performance requirements of the pod, while achieving the desired rotational speed (RPM). This relationship between torque and RPM is crucial for optimal operation.
- **Electrical Requirements:** The motor's voltage and power ratings had to be compatible with the pod's electrical system and power source. This ensured efficient and safe operation without overloading the system.
- **Size Constraints:** The motor's physical dimensions were restricted by the limited space within the pod. This necessitated finding a motor that provided the necessary power and performance in a compact form factor.

To address these challenges, engineers likely employed a combination of methods:

- **Performance Modeling:** Creating mathematical models to simulate the motor's performance under various conditions, predicting its torque and RPM output at different power levels.
- **Graphical Representation:** Plotting motor performance curves (torque-speed curves) to visualize the trade-offs between torque and RPM, aiding in the selection of a motor that met the specific operating requirements.

Through this rigorous analysis and evaluation process, the optimal motor was identified and selected for the pod.

7.6 Future Upgrades

7.6.1 Linear Induction Motor (LIM) Development and Adoption

The development and adoption of the Linear Induction Motor (LIM) has been identified as a key strategic priority, receiving dedicated attention and a specific budget allocation of £4000 for the coming year. This commitment underscores the importance of the LIM technology for future developments.

This focused effort will initially concentrate on foundational work in two critical areas:

- **Motor Selection:** A comprehensive evaluation process will be undertaken to select the optimal LIM for the intended application. This process will involve:
  - Defining precise performance requirements, including thrust, speed, and efficiency targets.
  - Analyzing various LIM designs and configurations, considering factors such as primary and secondary structure, winding arrangements, and cooling systems.
  - Conducting simulations and potentially physical testing to validate performance predictions and assess suitability.
  - Evaluating factors such as cost, availability, and maintainability.
- **Battery Selection:** Parallel to the motor selection, a detailed investigation into suitable battery technologies will be conducted. This will encompass:
  - Determining the required energy capacity and power output to meet the LIM's operational demands.
  - Assessing different battery chemistries (e.g., Lithium-ion, Nickel-Metal Hydride) based on energy density, cycle life, safety, and cost.
  - Evaluating battery management systems (BMS) for optimal charging, discharging, and thermal management.
  - Considering factors such as size, weight, and environmental impact.

This dual focus on motor and battery selection will provide a solid foundation for the successful integration of the LIM system. The outcomes of these initial efforts will inform subsequent design, prototyping, and testing phases, ultimately leading to the effective implementation of the LIM technology.

8 Electronics, Controls and Communications

8.1 Architecture

The embedded system architecture of the pod integrates several critical subsystems, ensuring real-time control and communication. STM32 microcontrollers are used for core control tasks, leveraging their advanced DSP capabilities and integrated ADCs. These microcontrollers manage the levitation, propulsion, and braking systems, enabling precise and reliable operation. A Raspberry Pi 4 single-board computer (SBC) serves as the central processing unit, hosting a web server for monitoring and managing subsystem interactions. The pod's internal communication system is based on the Controller Area Network (CAN) protocol, widely used in safety-critical automotive applications for its fault tolerance, low latency, and robustness against electromagnetic interference (EMI). CAN's differential signalling minimises the effects of EMI, ensuring reliable data transfer. Wireless communication between the pod and the base station is facilitated by a TP-Link access point, enabling high-speed data transmission and real-time monitoring. The system architecture is designed with redundancy in critical areas to minimize the risk of single-point failures. For example, secondary communication pathways provide fail-safe operation in case of primary link failure, and backup controllers ensure the continuity of essential functions. These redundancies, combined with robust fault-tolerant communication, ensure seamless operation under dynamic conditions. This design prioritizes robustness, scalability, and reliability, aligning with the safety-critical requirements of a high-speed pod system. The figure below illustrates the architecture, where green arrows represent serial communication lines, thick red arrows indicate high voltage lines, thin red arrows indicate low voltage lines, orange arrows are wireless communication, and blue arrows signify other communication pathways elaborated upon in the sections below.

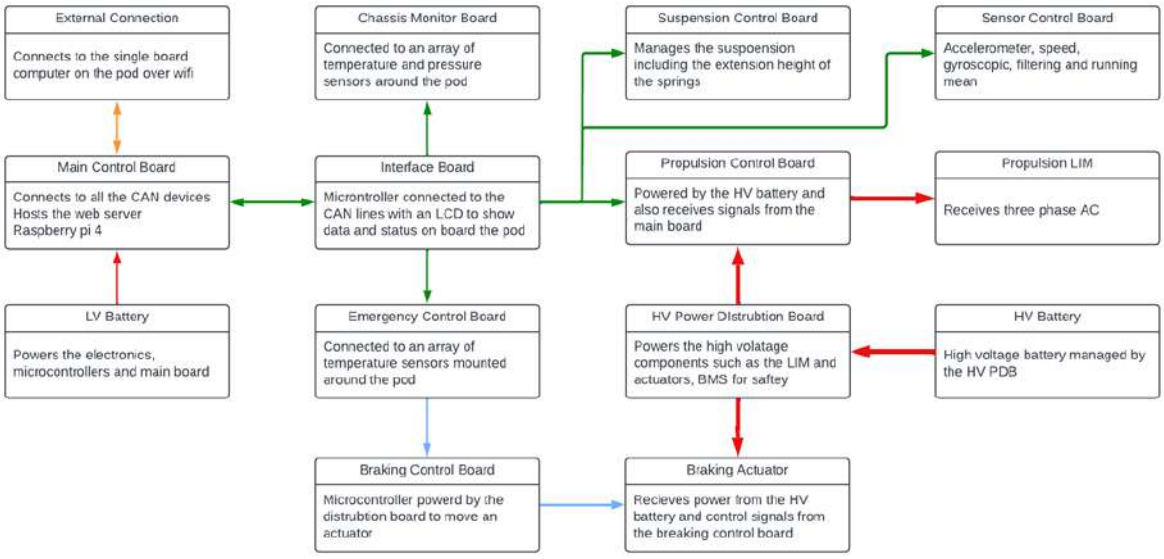

Figure 35: Architecture Diagram.

8.2 Control System

The control system dynamically adjusts the pod's levitation, propulsion, and braking to ensure optimal performance and stability. Real-time inputs from sensors are processed using adaptive control algorithms to maintain precise operation under varying conditions. The modular firmware design ensures scalability, allowing future enhancements without significant hardware modifications. Kalman filter algorithms are implemented for state estimation, providing effective handling of sensor noise, while fault tolerance is achieved through redundant systems and robust communication protocols.

8.3 Data Acquisition (Sensor Network)

The data acquisition system collects real-time information on critical parameters such as levitation height, acceleration, and thermal conditions. The CAN bus serves as the backbone of the sensor network, offering noise-immune, fault-tolerant communication. The CAN protocol achieves reliable data transfer through several key mechanisms:

- Differential Signaling: CAN uses two wires (CAN H and CAN L) for data transmission. This design minimises the impact of EMI, as any noise affects both wires equally, and the differential receiver cancels out the noise.
- Error Detection: The CAN protocol uses cyclic redundancy checks (CRC), bit stuffing, and frame checks to detect and correct transmission errors. Messages with detected errors are automatically retransmitted.
- Prioritised Messaging: Each message on the CAN bus includes an identifier that determines its priority. Critical commands, such as emergency stops, are transmitted with the highest priority, ensuring they are delivered without delay. The sensor network integrates the following key components:
- Inertial Measurement Units (IMUs): Provide acceleration, orientation, and position data for pose estimation.
- Laser Distance Sensors: Measure levitation height with high precision.
- Temperature Sensors: Monitor thermal conditions in the braking and propulsion systems to prevent overheating.
- Barometric Pressure Sensors: Ensure accurate environmental monitoring within the pod. Redundancy is incorporated into the measurement of critical parameters, such as levitation height and IMU data, to improve reliability. This design ensures accurate data acquisition even under noisy or adverse conditions.

8.4 Signal Processing

Signal processing is performed locally on STM32 microcontrollers, leveraging their integrated DSP capabilities and ADCs to refine sensor data efficiently. This decentralised approach minimises latency,

ensuring timely adjustments to the pod's operation. Several advanced algorithms are implemented to support precise control:

- Kalman Filters: Extensively used for state estimation, combining predictions from dynamic models with sensor measurements to reduce noise and improve accuracy.
- Fast Fourier Transform (FFT): Analyses vibration data from the suspension system to detect resonances, enabling corrective measures to prevent structural or operational issues.
- Predictive Control Algorithms: Uses data from laser distance sensors and IMUs to calculate optimal parameters for braking force and levitation height, ensuring smooth transitions and efficient performance.

This localised processing approach reduces communication delays, ensuring real-time availability of actionable insights to the control system. These insights support precise adjustments, enhancing stability and operational efficiency.

8.5 Controllers

The pod's controllers translate high-level decisions from the control system into precise physical actions, such as adjusting levitation forces, controlling motor speeds, and modulating braking torque. STM32 microcontrollers manage these tasks with modular firmware that allows scalability and flexibility. Each module is dedicated to a specific function:

- Levitation Control: Dynamically adjusts magnetic forces based on levitation height data.
- Braking Control: Modulates braking force using real-time speed measurements from tachometers.
- Propulsion Control: Manages motor speed and torque for smooth acceleration and deceleration. Feedback loops ensure precise actuation:
- The levitation feedback loop continuously adjusts magnetic forces to maintain optimal levitation height.
- The braking feedback loop dynamically modulates braking force to achieve smooth and controlled deceleration.

CAN-based communication ensures reliable and timely transmission of commands and sensor data, with prioritisation of critical messages. To enhance safety, redundancy is incorporated, particularly in critical systems such as braking. Secondary controllers take over in case of a primary controller failure. Pre-programmed emergency protocols, such as rapid deceleration, override standard operations when safety thresholds are exceeded. This architecture provides precise, reliable operation while remaining adaptable for future requirements.

8.6 Communication Systems

The communication systems ensure seamless data transfer within the pod and between the pod and the base station, supporting real-time control, monitoring, and diagnostics. CAN is employed for intra-pod communication due to its low latency, fault tolerance, and ability to handle safety-critical data, as detailed in Section 4.2.1. Wireless communication with the base station is achieved through a TP-Link access point connected to a Raspberry Pi 4 SBC, which acts as the central hub for managing intra-pod and external communication. The SBC hosts a web server for real-time monitoring and control by the base station. To enhance reliability, the system includes redundancy for safety-critical operations, detailed in section 4.5. Secondary communication paths ensure connectivity in case of primary link failure. These features collectively ensure robust, uninterrupted communication under all operating conditions.

8.7 Localisation Systems

The localisation system determines the pod's precise position and orientation on the track, enabling real-time adjustments for navigation and stability. A dual-sensor approach is employed, combining IMUs for acceleration and orientation data with laser distance sensors for levitation height measurements. To mitigate drift in IMU readings, fiducial markers along the track are being explored for periodic recalibration, ensuring accurate localisation over long distances. Kalman filtering is used to fuse sensor data, providing accurate state estimation. The team is actively investigating Extended Kalman Filters (EKF) to better handle nonlinear dynamics, such as pose estimation, and improve accuracy. This enhancement is expected to address challenges such as track irregularities and high-speed manoeuvres, further enhancing localisation performance.

8.8 Safety Systems

The safety systems are designed to ensure fail-safe operation under all conditions. The design prioritises redundancy, reliability, and real-time response to minimise risks and maximise operational safety. These choices reflect the high-stakes environment in which the pod operates, where rapid responses to failures are critical. Key safety features include:

- Emergency Braking Protocols: Pre-programmed responses to events such as power loss or communication breakdowns, ensuring the pod is brought to a safe stop. The redundancy in braking controllers ensures the system remains functional even in the event of a hardware failure.
- Battery Management System (BMS): Continuously monitors battery parameters, preventing overcharging, overheating, or other hazardous conditions. Low-level programming allows precise control of hardware, ensuring efficient and deterministic operation.
- Fault-Tolerant Communication: Utilises CAN's error detection and prioritisation features, with an external RF link providing an additional layer of safety for emergency shutdown signals.

The system's redundancy ensures continuous operation by duplicating critical components, such as controllers and communication pathways. For instance, secondary controllers and backup communication

links are ready to take over if a primary system fails. These measures, combined with robust monitoring and fail-safe protocols, ensure the system is dependable and capable of responding effectively to emergencies.

8.9 Other Systems

Additional subsystems, such as diagnostic tools and the Human-Machine Interface (HMI), provide real-time insights into pod performance. The HMI features an LCD screen displaying critical metrics, including subsystem statuses, battery voltages, and error messages. Automated alerts generated by diagnostic tools ensure timely identification and resolution of potential issues, minimising downtime and enhancing operational transparency.

8.10 State Machine Diagrams

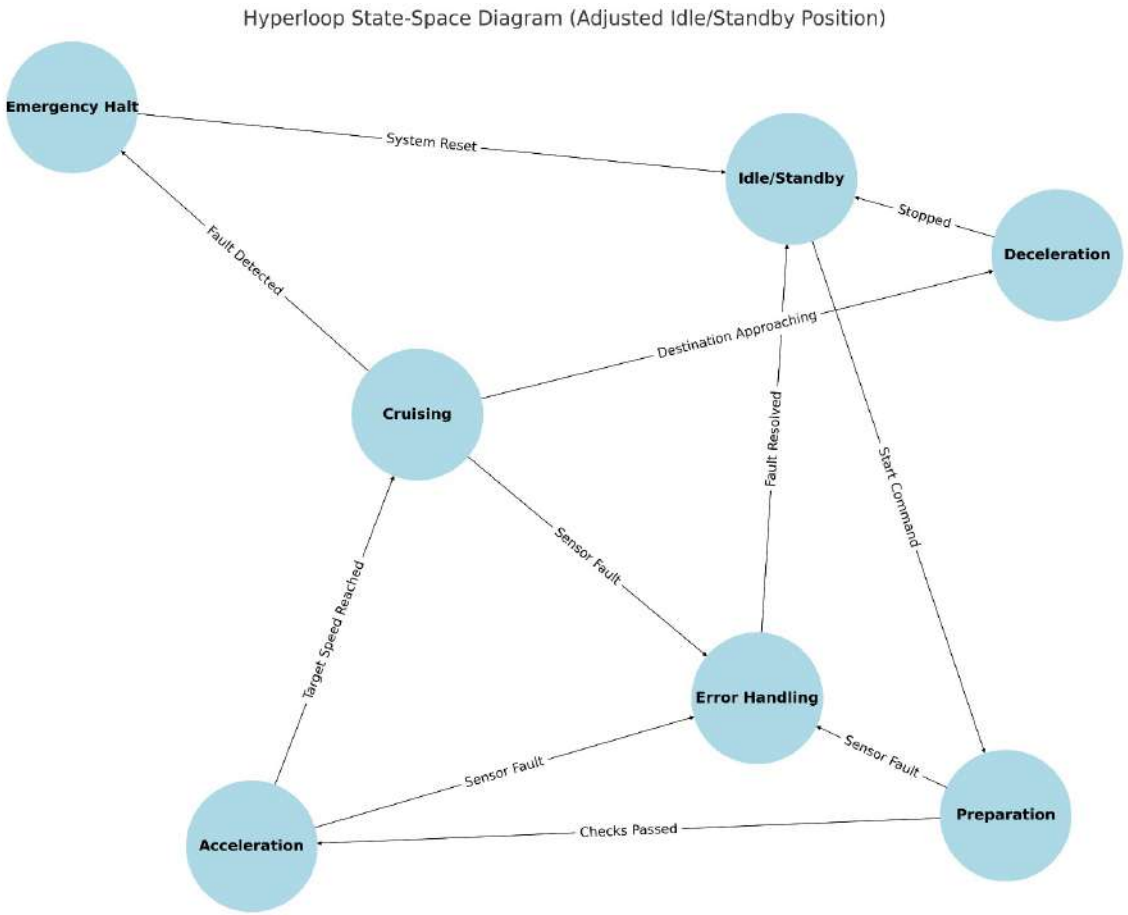

Figure 36: State Machine Diagram.

8.11 Testing Objectives

• Validate UART serial communication from STM32 to Raspberry Pi. • Test Flask server functionality for parsing and transmitting data. • Evaluate wireless signal stability and transmission range. • Measure

data latency and update refresh rates on the user interface.

8.12 UART Testing

All STM32 boards were tested at a baud rate of 115200 bps. UART data transmission was found to be stable across all connections, with no packet loss observed under standard test conditions. The use of UART enabled easy debugging via serial terminals, providing visibility into transmitted packets that would not have been feasible with CAN.

8.13 Packet Format and Parsing

Each board transmitted data using the structured format: ¡BoardID¿—KEY=VAL,KEY=VAL,... This human-readable format proved easy to debug and extend. The Raspberry Pi parsed the data using a dedicated Python module, which sorted values by board ID and relayed them to the frontend interface via WebSocket.

8.14 Dashboard and User Interface

The dashboard displayed live data from all STM32 boards in a structured and user-friendly format. Data updates occurred every 2 seconds, and the latency between transmission and visual update was minimal (typically ¡ 150 ms). Each tab on the dashboard reflected a specific subsystem, with green/red LED indicators showing port status. The Raspberry Pi temperature was monitored locally and triggered a red warning icon if thresholds were exceeded.

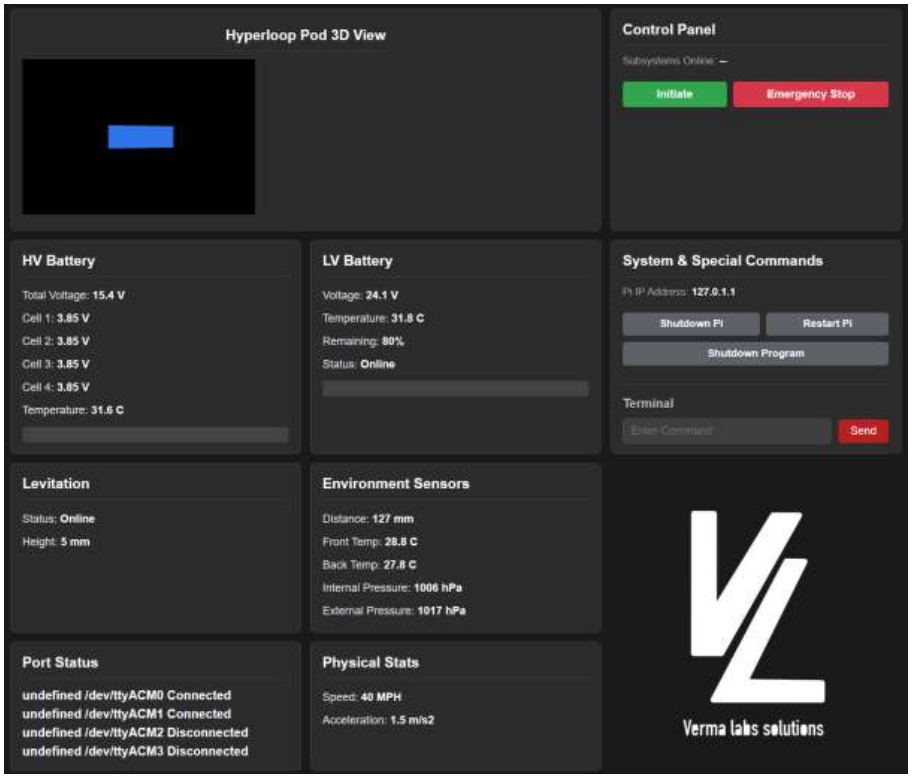

Figure 37: User Interface dashboard.

8.15 Software Design

The wireless communication system software, as shown in the figure below, was developed to enable real-time monitoring of the pod's sensor data through a browser-based user interface. A simple web dashboard was created as the frontend, allowing engineers to view key system parameters during testing and debugging. The backend was implemented using Python, where a primary script, App.py, was responsible for hosting a local web server using the Flask framework. This server managed communication between the STM32 boards and the frontend dashboard. The graphical user interface (GUI) was designed using standard web development tools, including index.html for structure and style.css for styling. Incoming serial data from the STM32 boards was handled by a dedicated Python script, serial_parser.py, which processed, decoded, and arranged the data into structured packets according to the board ID and associated parameters. On the frontend, a JavaScript file, main.js, received the processed data via WebSockets and dynamically updated the relevant values displayed on the user interface in real time. This modular software architecture ensured clear separation between the data processing layer and the user display layer, enabling efficient system monitoring and future scalability.

9 Levitation and Stabilisation.

9.1 Overview

The levitation system of the hyperloop pod can be considered the most important component of all the subsystems that comprise a fully functioning hyperloop train. As the MagLev Team is still maturing and technology with guiding subsystems still improving, a passive magnetic levitation subsystem was chosen due to its safety, reliability and manufacturing aspects. The current design produced consists of running 2 large Halbach arrays with relative motion of a large conductor plate. The prior is aimed to be fixed to the moving pod, and the latter will act as the 'rail' equivalent in the electromagnetic system. By continuing research done in 2023, by analysing an overview of the system from relevant research papers, a decision was made to go ahead with a passive levitation system. The research conducted comprised of analysing versatile analytic dependencies of the system, for example running several simulations to determine the maximum velocity and the most optimal Halbach array formation to produce the most lift force. Additionally, with communication with the other subsystems, a finalized CAD design had been produced of the magnetic levitation 'skis' and manufacturing of these 'skis' have been completed by one of the sponsors. Before the passive magnetic levitation system 'activates', mechanical wheels will supplement the electromagnetic design, which has been designed for operational use during the low velocity phases of the pod when the lift force does not overcome the weight force. As the velocity of the pod increases the lift force, FL, will increase until levitation is possible. Following this, the mechanical suspension subsystem will stabilise the pod at a fixed suitable height.

9.2 Specifications

Parameters	Definition	Chosen Value
l	Total Length of Halbach Array	0.4 m
d	Total Height of Halbach Array	0.01 m
s	Total Width of Halbach Array	0.12 m
λ	Halbach Wavelength	0.08 m
k	Halbach Wavenumber: $\frac{2\pi}{\lambda}$	$78.53\ m^{-1}$
M	Number of Magnets per Wavelength	8
y	Distance from Surface of Conductor Plate	0.015 m
h	Thickness of Conductor Plate	0.007 m
μr	Relative Permeability of Conductor Plate	1
σ	Conductivity of Conductor Plate	$3.5 \times 10^7\ \frac{S}{m}$
B_r	Remnant Magnetization of Magnets	1.28 T

Figure 38: Parameters of Halbach Arrays.

9.3 Budget and Timeline

Maglev System: Estimated Cost £2,000

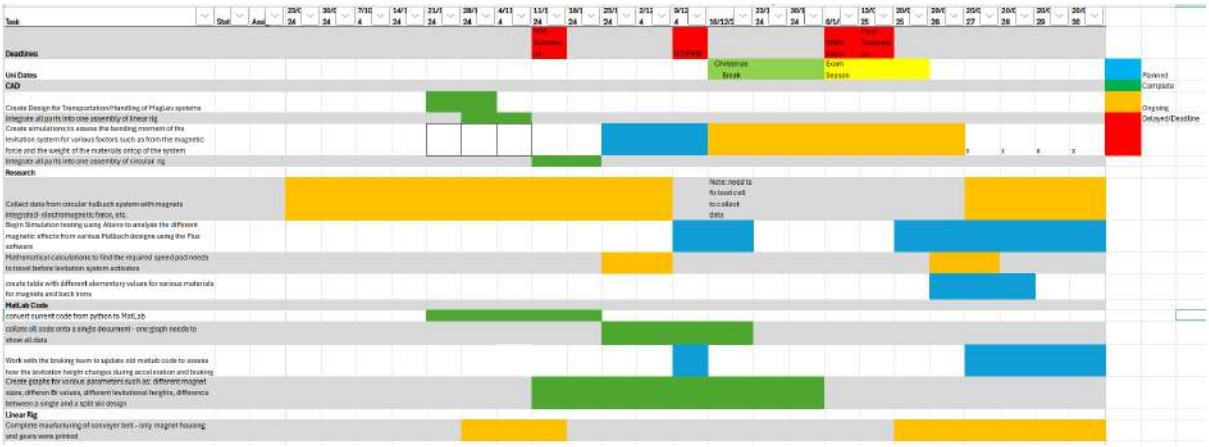

Figure 39: Gantt Chart Maglev.Sem-1

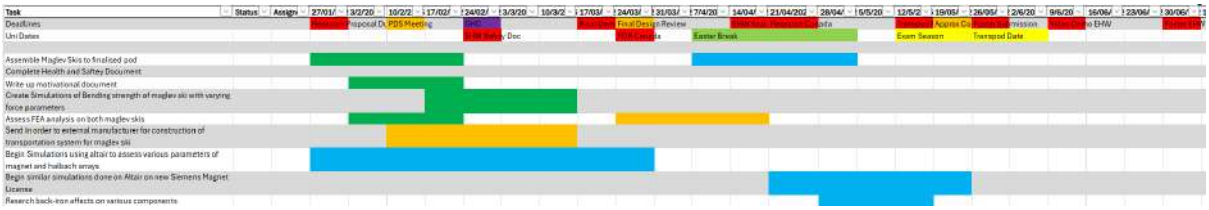

Figure 40: Gantt Chart Maglev. Sem-2

9.4 Inspiration

After assessing the differences between the pros and cons between a split ski or a single ski design, a decision had to be made for the levitation system. Considering both design options and experimental simulations carried out, a conclusion was set forth for the manufacturing for a split ski design. As seen in the research section, the lift force between a split ski and a single ski design is exactly the same but the change in lift force between the two designs would only come from changes in the magnetic field distribution. Moreover, the choice of designing a split ski design was mainly due to cost and the ease of manufacturing. Instead of creating one long ski, two individual skis would be manufactured, halving the amount of material used and thus reducing costs.

By also considering the weight of a split or a single ski design, a single ski would be too heavy for skeletal structure of the chassis, thus the manufacturing of a split ski design would allow for better weight distribution on the chassis design and the overall weight distribution for the entire Hyperloop pod. By also assessing the weight, it was concluded that both skis that would be eventually manufactured would be connected to the suspension systems. This would allow for more stability of the Hyperloop pod as the suspension system is firmly attached and integrated to the chassis base.

Adding on to the previous section, a split ski design has been created as each ski would be located close to the braking system allowing for better control for the levitation height between the pod and the

track during acceleration and braking. This is crucial as the pod's levitational height is ideal between 5 – 10mm from the track. If the pod touches the track, damage could be caused to major systems such as the suspension, braking and even the levitation system.

In addition, a split ski design allows for better manoeuvrability of components within the chassis, allowing for ease of design and manufacturing of the whole Hyperloop pod.

Now that a split ski design has been chosen, it was also crucial to decide on the type of Magnets that would be used in each ski. From additional simulations carried out, it can be seen that magnets of a cubic size of 1 cm would be most optimal for levitating the pod at a desired levitation height of 10 mm. Smaller magnets are also ideal for the design for one ski as they are most cost efficient and are a lot lighter than larger magnets. They also take up a lot less space, which is optimal for a smaller Hyperloop pod design. Additionally, a Halbach array with smaller magnets would create for a more uniform distribution in magnetic force, creating more stability and control of the pod for the required challenge. By also using smaller magnets, design alterations for the ski are a lot easier allowing for various designs for one ski. Thus with a split ski design (and by using smaller magnets), one ski design can be configured differently to the other ski. Lastly, smaller magnets would allow for less power requirements in different levitation systems. By assessing various magnet types from different materials and magnetic remanence strength, N52 Neodymium magnets were chosen. While these magnets are more expensive than weaker grades, using them as smaller magnets is ideal as they can offset original costs. This is because their magnetic strength is exceptionally strong in any magnet size. The most important reason for choosing these magnets is for their ability to alter the magnetic polarity within each magnet. This is crucial as the whole levitation system is based on the Halbach array theory. Because of this, the polarity in each magnet has been altered with a 45 degree angle, allowing each ski to have a suitable implemented Halbach configuration within.

9.5 Challenges

The main challenge faced with creating the ski design was ensuring that the back brackets would be aligned correctly in correspondence with the suspension system. If not, both skis would not be able to be connected to the suspension system, and thus won't connect to the Hyperloop pod. Another challenge faced was to ensure that of the 2 x 456 magnets ordered that they would fit into the ski. Research was done for the most optimal and strength-resistant glue. Because of there being so many magnets, it was made mandatory that when operating both skis, all electronic and metal items were removed from the body. Additionally, a transportation/handling system was created to reduce the amount of injuries that could occur when handling both skis. This system was created after an injury occurred whereby one of the engineers cut themselves while handling a ski. Adding on, because of the weight of the ski, being around 9 kg in total, the ski couldn't be handled by hand, thus an easy attachment was created.

9.6 Results and Graphs

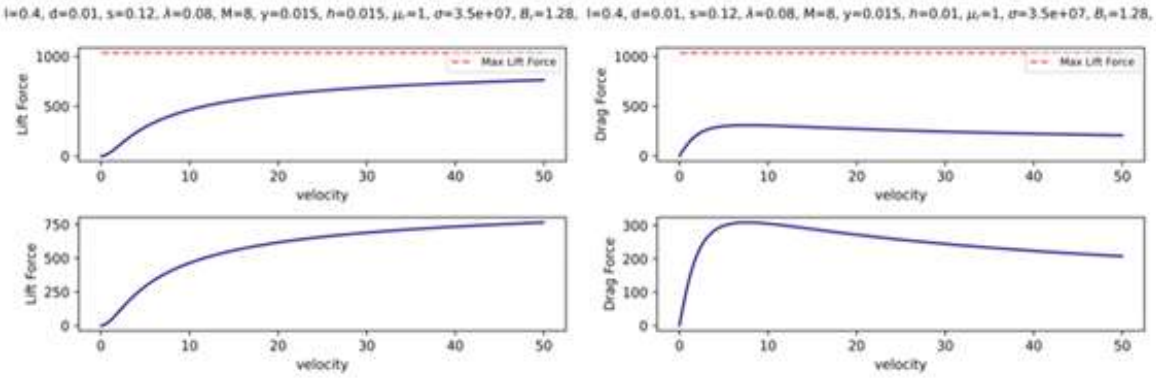

Figure 41: Simulated Plots of Passive Lift Forces and Drag Forces (N) against Velocity with maximum lift force written in MATLAB.

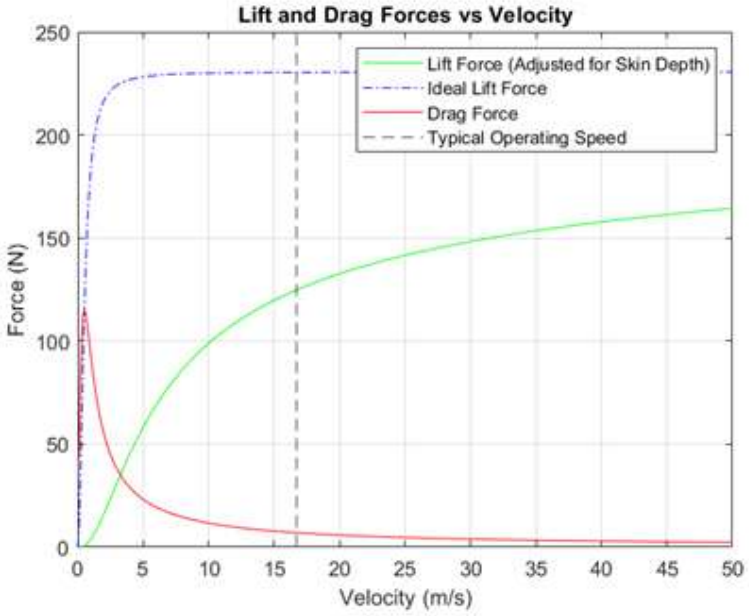

Figure 42: Lift and Drag Forces as a Function of Velocity with parameters: M=4, d= 0.01m, Br = 1.28 T

9.7 Simulation and Theoretical Framework.

The simulations carried out were used to assess how different parameters would affect the lift force and the drag force created by the designed 'skis'. These simulations would provide a better insight to why the proposed design was manufactured and the different affects it would have on the overall pod during propulsion. A MATLAB code was written by analysing the lift and drag force equations in Figure 1, and inputting different parameters to assess the variation in lift and drag force.

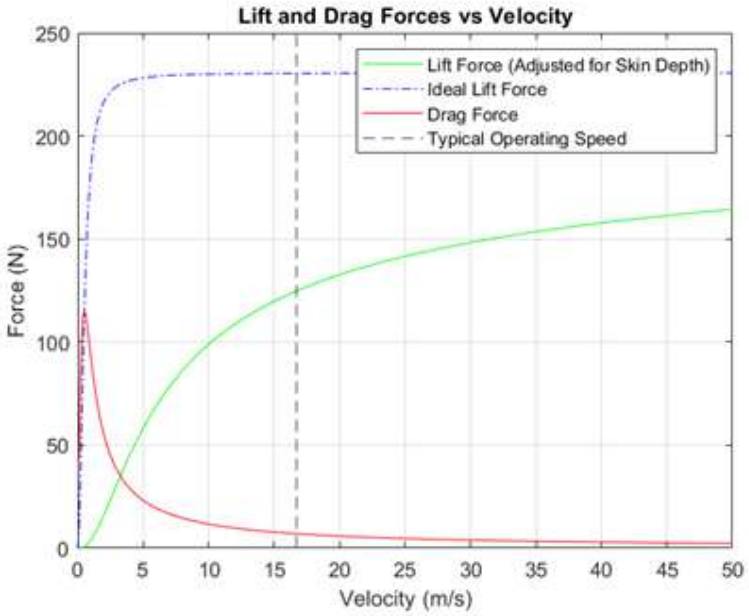

Figure 43: Lift and Drag Forces as a Function of Velocity with parameters: M=4, d= 0.01m, Br = 1.28 T

Initially, it is observed that the lift force increases and grows rapidly to a speed of 5 m/s. Beyond this peak, the lift force declines and stabilises as the velocity increases. This is when it is adjusted for skin depth which is the distance into a conductor at which the electromagnetic wave decreases to a certain value. The blue line indicating ideal lift force assumes theoretical conditions which neglects skin depth. The drag force, in red, increases to a peak as velocity increase but decreases as velocity increases. This is due to eddy currents in a conductor reaching a peak value as velocity increases. The dashed black line indicates a typical operating speed at which the lift force is suitable enough for levitation and the drag force is minimal. This speed is assumed to be 15.6 m/s. This graph indicates the initial parameters of a preliminary design. More simulations results were produced by varying the M number, Br, and the levitation height.

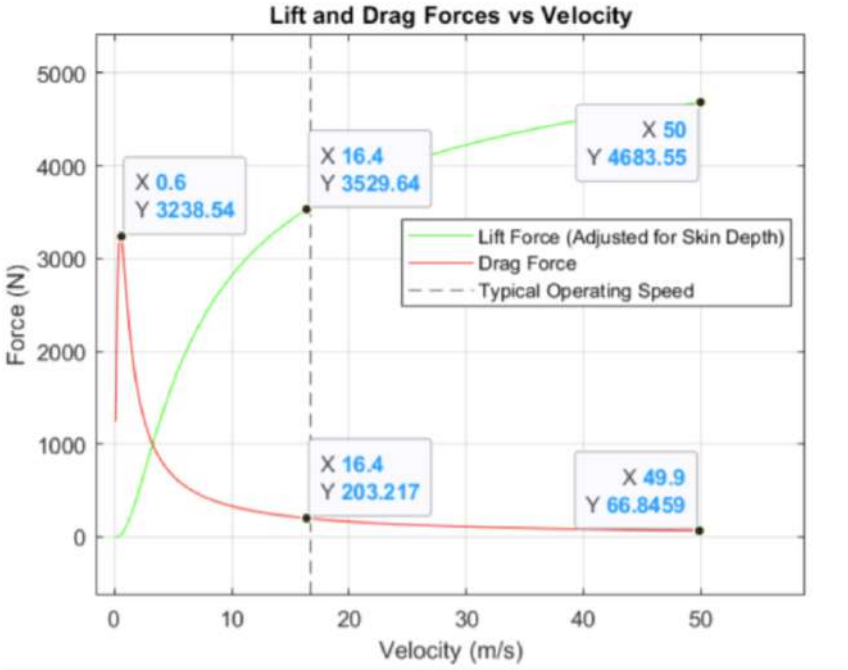

Figure 44: Lift and Drag Forces as a Function of Velocity with parameters: M=4, d= 0.05m, Br = 1.42 T

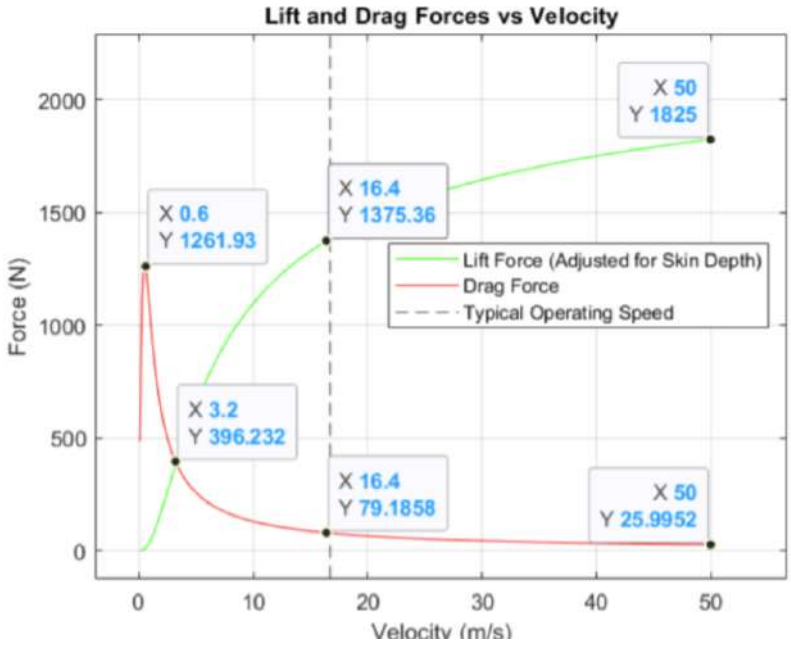

Figure 45: Lift and Drag Forces as a Function of Velocity with parameters: M=4, d= 0.005m, Br = 1.42 T

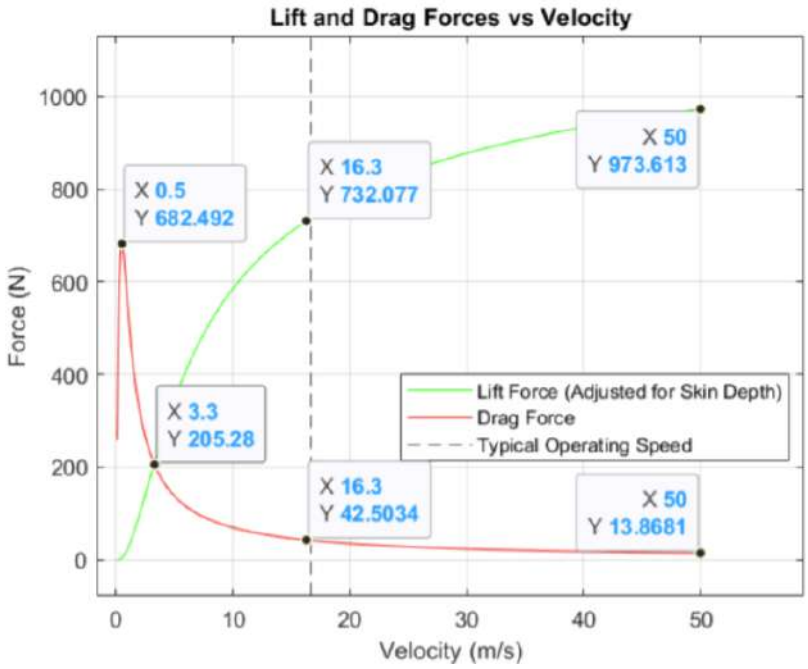

Figure 46: Lift and Drag Forces as a Function of Velocity with parameters: M=4, d= 0.008m, Br = 1.42 T

As seen in the above Figures by varying different parameters the lift force changes as the velocity changes. This can also be said for the drag force acting on the pod during linear motion. As seen with all of the figures, the difference between the peak drag force and the lift force where velocity is optimal, are marginally very close to each other. However, when analysing the lift and drag force values at the optimal velocity point, the difference between the lift and drag force is greatest when the levitation distance is 0.005 m and M=4. The parameters with an associated levitation distance of 0.005 m. produces the highest peak lift force when velocity is equal to 50 m/s.

After assessing the different factors such as different M numbers and levitation height, it was also important how different magnet sizes would affect the lift and drag force of the ski's being used. By manipulating the MATLAB code and assessing the various graphs being produced by the simulations, the code and graphs would provide a better insight to which magnet size would provide the most lift force with the most minimal drag force being produced. The magnet sizes being plotted in the graphs are 1 cm , 2 cm, 3 cm and 5 cm.

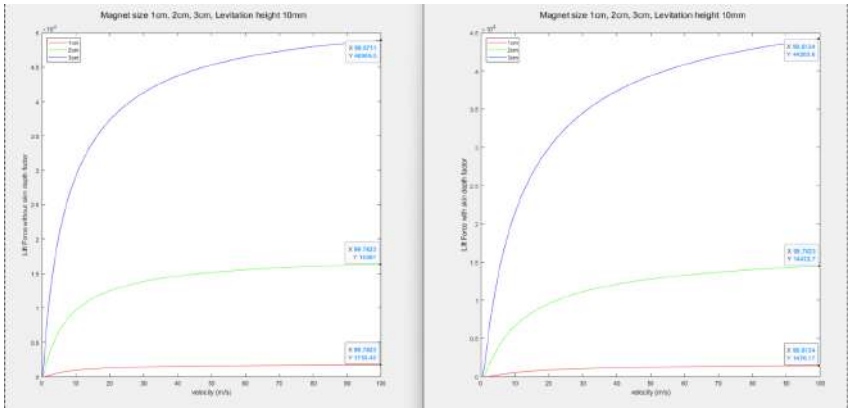

Figure 47: Lift force with skin factor in relation to velocity.

As seen in the above, the greatest lift force being produced is from the 3 cm magnet. However, due to the whole Hyperloop pod weighing just less than 100 kg, a lift force of more than 48000 (N) is not needed. Additionally, this would also increase cost for manufacturing and altering the polarity of the magnets would be a lot harder. From this a magnet size of 1 cm was chosen as it provided enough lift force to levitate the Hyperloop Pod. The lift force produced from the 1cm magnet size (without the skin depth factor) is 1752.42 (N). The force produced by this magnet size is related to one ski. Assuming that the lift for produced by two skis is exactly twice as much, it would result in a total lift force of 3504.84 (N), which would be sufficient enough to levitate the entire Hyperloop pod with a levitation height of 10 mm. The magnetic remanence included in Figure 7 is 1.42 (T), with a total of 456 magnets in each ski. Even though the lift force produced by the magnets is sufficient enough to levitate the pod, it was crucial to see if the lift force produced including the skin depth factor would be sufficient enough with different magnet sizes. Analysing the graph on the in Figure 7, it is clear to see that the total lift force produced by one ski is sufficient enough to levitate the pod, with a lift force of 1476.17 (N). Additional graphs representing lift force with various magnet sizes and levitation height can be viewed in Figures below.

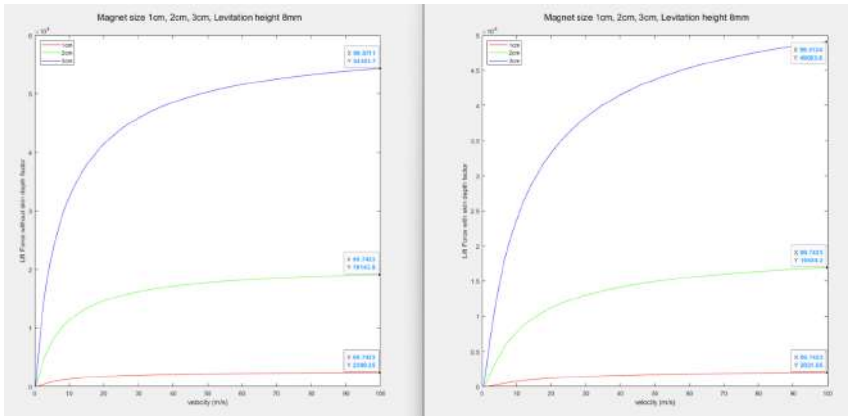

Figure 48: Lift force with skin factor in relation to velocity. LH=8mm

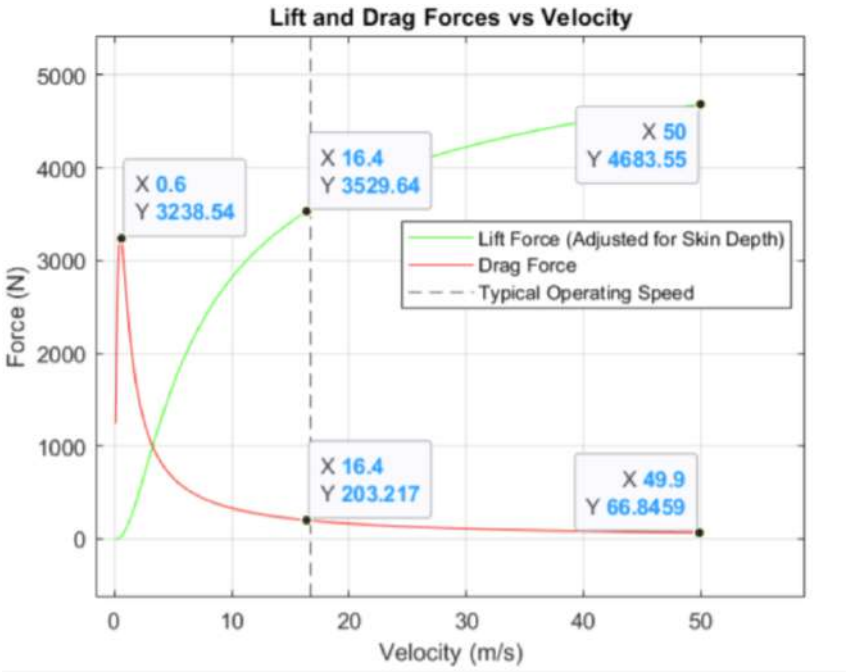

Figure 49: Lift force with skin factor in relation to velocity. LH=5mm

As observed in Figures above, the lift force for a 1 cm magnet has changed with a change in the levitation height. The levitation heights have been changed to 8mm and 5mm from a 10mm levitation height. Again, the lift force produced in these graphs are of the same magnet remanence and magnet quantity in the ski. A change lift force produced could be due to a change in the eddy currents generation, with a lower levitation height imposes a greater opposing force due to Lenz's law, resulting in a stronger magnetic field from Faraday's Law resulting in a stronger lift force. Since the Halbach array geometry has been kept constant throughout, a change in lift force has not been caused by this but could also be resulted from greater losses from resistivity or from the skin depth. With a lower levitation height, the field variations are a lot stronger and Eddy currents being more concentrated. If the levitation height is increased, the penetration of weaker fields is greater causing a loss in lift force and lift force efficiency. Lower levitation heights are also related to a higher drag imposed on the Hyperloop pod, whereas a higher levitation height causes for loss in stability.

Consequently, the assumption of the lift force being proportionally twice that of one ski for a split ski combination cannot be taken for granted. Graphs have been simulated using MATLAB to analyse the difference between the lift force produced from a single and a split ski combination. These can be viewed in Figures below.

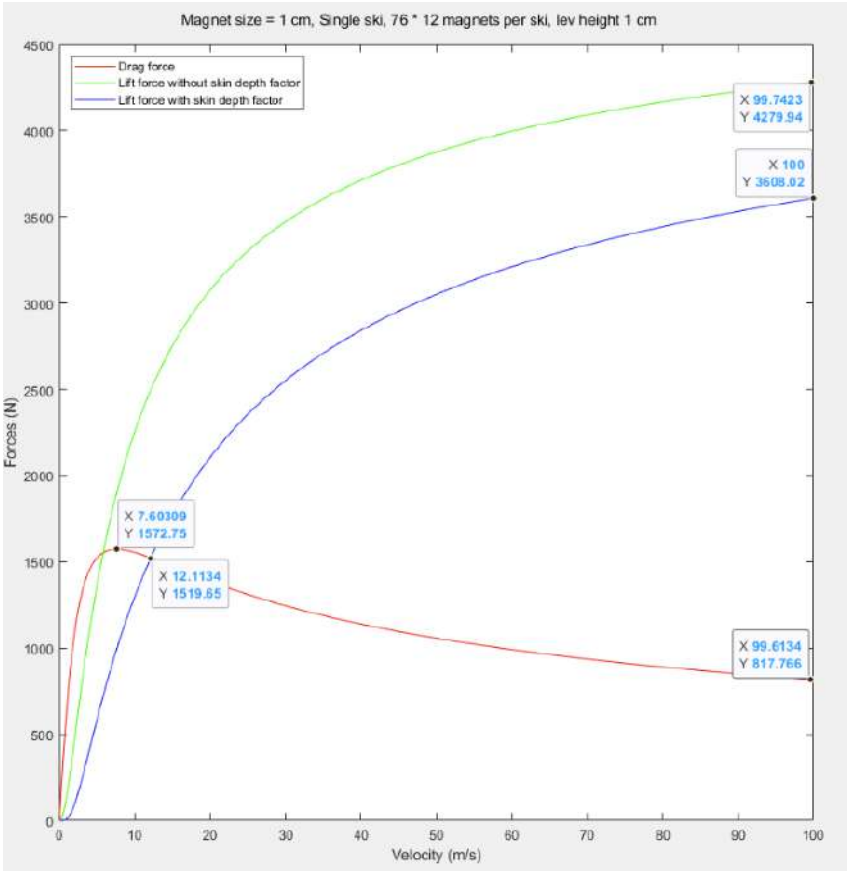

Figure 50: Lift force with skin factor in relation to velocity. LH=5mm

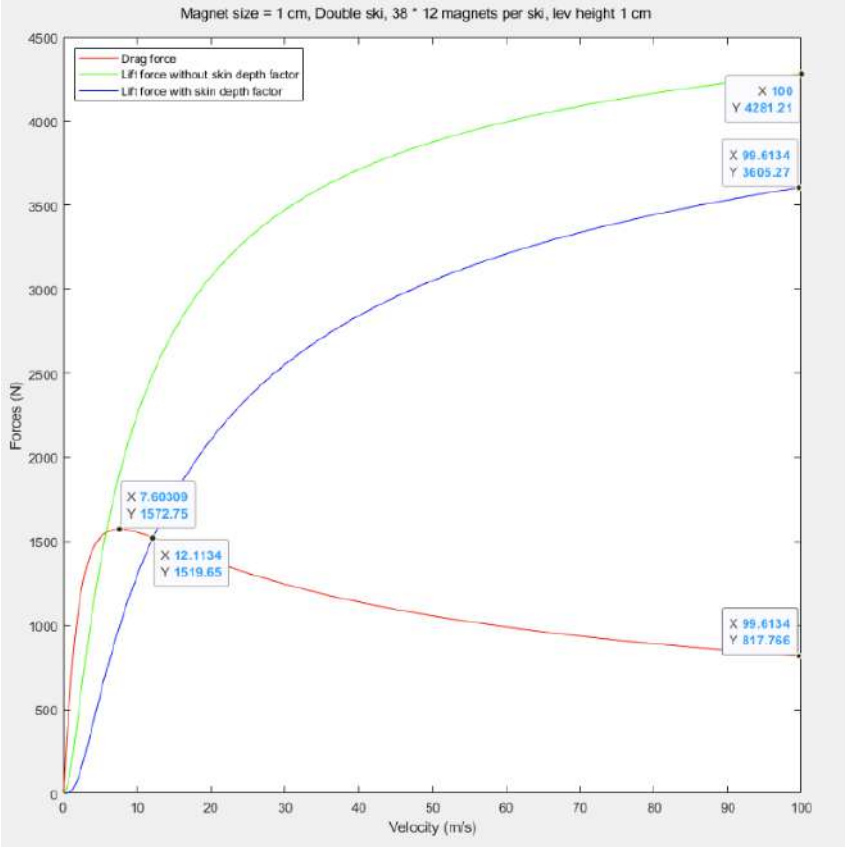

Figure 51: Lift force generated with split ski design.

As seen in both figures above, the difference between the lift forces generated in a single ski design and a split ski design is close to identical. This is the same for various changes in levitational height. Thus, choosing between a single or a split ski design will come down to the pros and cons between them both an what is most suitable for task at hand. The pros and cons can be viewed in the table below.

9.8 Comparison Between Single and Split Ski Halbach Levitation Systems

Aspect	Single Ski Halbach System	Split Ski Halbach System
Design Simplicity	**Pro:** Simpler design with fewer moving parts. **Con:** Less flexibility in adjusting lift dynamics.	**Con:** More complex design requiring precise alignment of skis. **Pro:** Independent adjustment of each ski enables more control.
Lift Distribution	**Pro:** Uniform lift force over a single surface. **Con:** May struggle with terrain irregularities.	**Con:** Uneven lift distribution if one ski misaligns. **Pro:** Better adaptability to uneven or curved surfaces.
Maneuverability	**Con:** Less maneuverable due to single, rigid structure.	**Pro:** Enhanced maneuverability, especially on curved tracks.
Weight	**Pro:** Lighter, as there's only one ski.	**Con:** Heavier due to dual skis and additional components.
Stability	**Pro:** Greater stability on straight and flat tracks.	**Con:** Requires careful balance between skis to maintain stability.
Energy Efficiency	**Pro:** Concentrated magnetic field reduces energy loss.	**Con:** Potentially higher energy loss if both skis are not perfectly aligned.
Complexity of Maintenance	**Pro:** Easier to maintain due to fewer components.	**Con:** More components to inspect and maintain.
Cost	**Pro:** Lower cost due to a simpler, smaller design.	**Con:** Higher cost due to increased material and manufacturing complexity.
Noise and Vibration	**Pro:** Likely lower vibration as the system is one cohesive unit.	**Con:** Potential for more vibration if skis are not synchronized.

Table 28: Comparison of Single and Split Ski Halbach Levitation Systems

9.9 CAD Drawings.

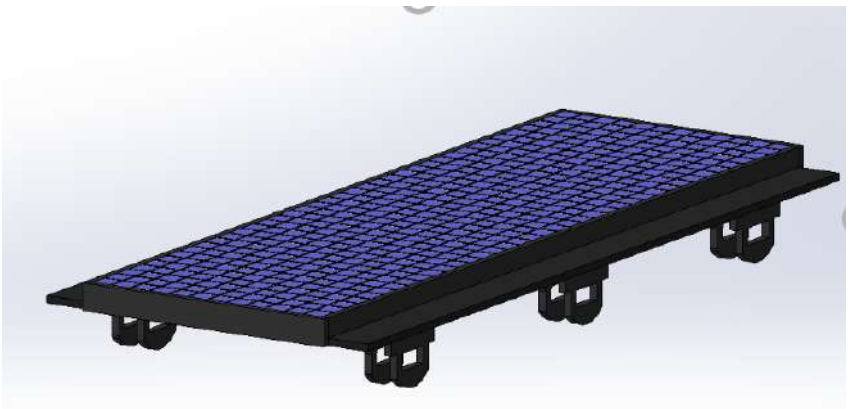

Figure 52: Lift force generated with split ski design.

Figure 53: Lift force generated with split ski design.

9.10 Future Work

Additional testing and simulation work will be conducted to assess variations in the magnetic field. This analysis will be performed using **Altair** simulation software, where different Halbach array configurations will be examined to compare magnetic field variations and their impact on system performance. This is still ongoing.

9.11 Safety Features

Many considerations were considered during the design process of the magnetic levitation system. As there are more than 400 magnets being used within the system, and wrought iron being used as the back iron and frame, the system is considerably heavy. To take this into account, the system will be carried using a crane to avoid any injuries for uncontrollable scenarios such as dropping the system. Additionally, a very important factor when handling the system is removing any metal objects connected to the body due to the strong magnetic field from the magnets. Storing both systems contains encasing them separately in wooden boxes with thick Styrofoam within.

Working with the rotation rig in the workshop involves high velocities from the motor. To ensure any injuries from happening, the motor is capped at a maximum velocity of 1000 rpm. In addition, the casing spinning at such a high rpm, contains magnets which are prone to being released from their housing. Thus, when testing the rig, precautions such as wearing goggles is applied and the rig is clamped to a secure surface to avoid any vibrations and unwanted scenarios. Lastly, when handling both 'skis', ant-cut gloves must be worn due to the sharp edges of the system.

Both of the magnetic levitation devices will be separately stored in wooden boxes with a thickness of 1 cm. Within the boxes, it has been ensured that the magnetic levitation ski sits in the middle surrounded by Styrofoam. Surrounding the Styrofoam, thin metallic plates cover the outline of the wooden box for extra protection from the magnetic levitation device. Before the magnetic levitation device is removed from the box, the person handling the device must ensure that all metallic items and devices are removed from the person – as mentioned in the previous sections. When handling the system, it is crucial to maintain a sufficient distance away from other metallic objects to ensure that the maglev

ski is kept clean.

54 illustrates the exponential decay of the magnetic flux density with increasing distance from the surface of the magnets on the ski. At the surface, the flux density is at its maximum, decreasing sharply within a short distance. Analyzing the gradient of the graph, it can be seen that the curve is initially very steep. However, the rate of decrease gradually lessens meaning that while the absolute drop in magnetic flux density per unit distance is high near the magnet, it becomes progressively smaller further from the magnet.

This behavior is crucial in mitigating the possible adverse effects of high flux density on surrounding components. Although the Halbach array produces a very strong magnetic field at the surface, the rapid exponential decay ensures that the field becomes negligible within a short distance. This limited reach, coupled with the use of back irons to prevent any magnetic flux leakage from the reverse side of the ski, protects the surrounding electronics and other sensitive equipment from unwanted interference during operation, even at the edges of the ski where the back irons are not effective. It confirms that while the magnets can generate the high flux required for levitation, they also inherently confine their field to a very localized region, ensuring the safety of nearby components and indicating the safe distances to keep objects at from the skis whilst handling and transporting them.

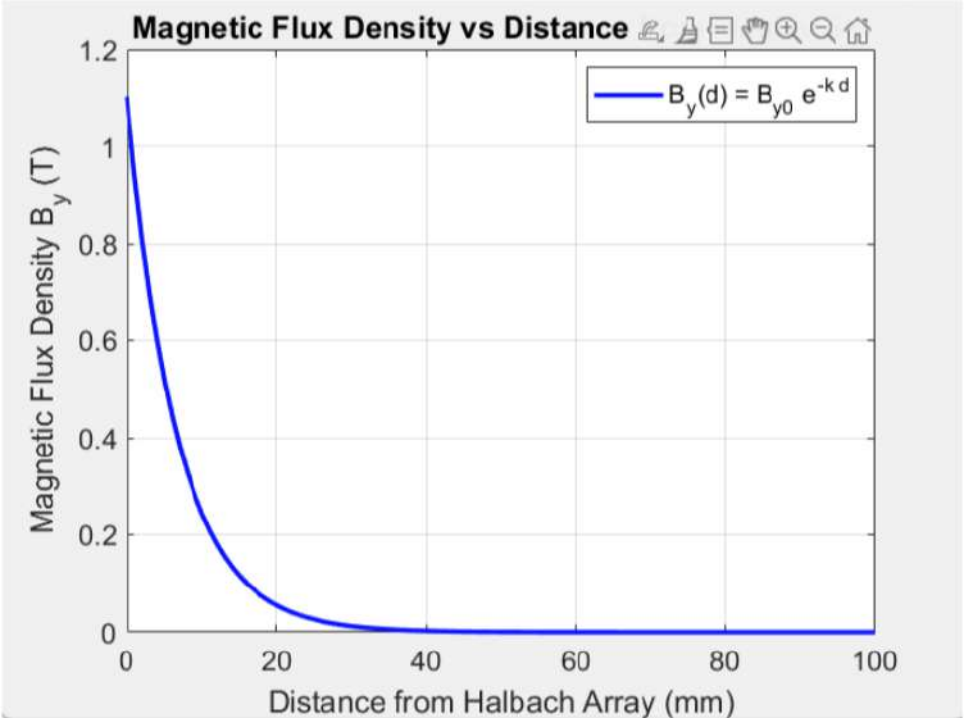

Figure 54: Lift and Drag Forces as a Function of Velocity for different configurations

10 Testing

The pod is planned to be tested at the University of Manchester, utilizing the 12m Aluminium 6061 T6 track belonging to the society. The purpose of these tests is to ensure the safe and expected operation of the mechanical and electromagnetic systems.

Delays in assembly: There were significant delays in acquiring the necessary components due to administrative processes and supplier coordination issues. Additionally, sponsorship agreements took longer than anticipated, as securing support required continuous negotiations between the society and partnering companies.

At present, we are in the process of assembling and integrating the subsystems into the pod, with the majority of sponsorship agreements finalized. We remain on schedule to complete the assembly and begin testing by Week 12 of the academic year (second week of May), ensuring the pod is competition-ready.

The upcoming Easter break is crucial for finalizing the assembly, as it will provide an open schedule and full access to university resources, enabling us to conduct the necessary tests before the competition. To mitigate the impact of these delays, we have attached the FEA design below.

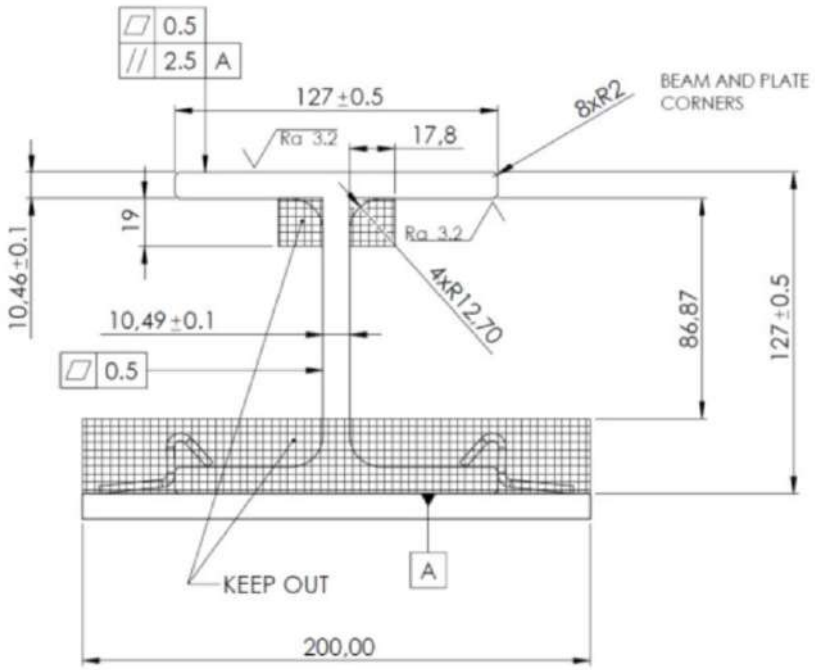

Figure 55: I beam dimensions.

10.1 Mechanical Systems

All mechanical systems are designed with a safety factor of 2 or more to account for the forces acting on the system and the material properties of the load-bearing components. This ensures structural rigidity while minimizing the impact of bending moments, shear forces and cyclical loads.

Chassis: The chassis will undergo bending and torsional stiffness to validate its ability to withstand the forces and moments experienced during acceleration, braking, and varying loading conditions. The

chassis shall also undergo impact hammer tests to determine its vibrational attitude. The measurement instruments to be used are laser vibrometer, piezoelectric gauges, strain gauges, ICP type accelerometers and LVDT. These tests ensure the displacements of the chassis align near the results of the extensive Finite Element Analysis (FEA) performed using ANSYS & Altair. Additionally, the modular nature of the chassis and its brackets witnesses the integration of different sub-assemblies at one location which requires validation with experimental testing.

Braking System: The braking system has been designed as an absolute fail-safe. A test version of the system, configured to handle lower loads with a more elastic spring, will be employed for initial testing. This approach allows for subsystem-specific evaluations before integrating all components into the pod. We have the ability to configure spring stiffness's by means of adjustor to preload the spring and also the ability to modulate the gas pressure. Friction materials will be tested to optimize performance at the tribology lab at the University, and pneumatic testing involves bench testing the system before mounting it on the pod for functioning. The use of a double-acting actuator enables tensioning of the spring to achieve the required compression and expansion during operation. This will also be used to validate the results from the FEA analysis conducted.

Suspension System: The suspension system is designed to dampen vibrations experienced by the pod and to support its full weight in the event of a failure. The suspension damper is a 4-way adjustable rebound, that can be tuned for various acceleration and braking situations. A pneumatic setup, allows the lifting of the wheels at activation of maglev. The spring damper units are adjustable allowing passive energy management. Since the springs sleeve over the dampers, we have dampers that account for different spring stiffnesses. The top and side suspension will undergo a weight test with ballast weights to account for different behaviour and settings. The pneumatic system will be bench-tested in coordination with the shaft assembly, linkage and wheels. This configuration protects the chassis's bottom section and the sensitive Halbach arrays attached to it during failure scenarios. This will also be validated with the FEA results as have been conducted by the FEA and shown above.

10.2 Electrical Systems

Motors: Electric motors powered by a battery were chosen due to budget constraints, delaying the acquisition of a Linear Induction Motor (LIM) system. This decision allows for careful budget management to secure a LIM system in the future. Motor calculations have been conducted for various combinations of pod weight and speed to optimize performance, focusing on parameters such as torque, power output, and energy efficiency under varying load conditions. The motor specifications are as follows; Schneider Electric 220 V dc 400 W Servo Motor, 5000 rpm, 3.81 Nm Max Output Torque, and 14mm Shaft Diameter. This selection was based on calculations of the specific velocity requirement needed for the Maglev system to generate sufficient lift force to levitate the pod. this was then used as a basis to find the voltage to source of a battery pack 2200mAh 18.5V 5S 35C Supersport Pro LiPo Battery 12 batteries will be used.

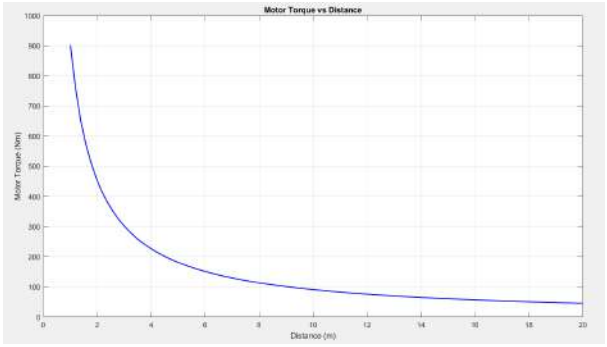

Figure 56: Magnetic levitation and velocity relation.

Motor Torque Calculation

$$T_m = mR_w \left[\frac{v^2 - u^2}{2s} + g(r_r) \right]$$

- $m = 100$ kg
- $R_w = 60$ mm
- $v = 6$ m/s
- $u = 0$ m/s
- $s = 8$ m Acceleration distance
- $g = 9.81$ m/s^2
- $r_r = 0.009$
- $GR = 2$
- $N = 4$ Number of Motors

The motor torque calculations allow for the required plots to allow the scoping of motor selection, leading to battery selection that depends on the voltage selection. The attached matlab code is provided in the appendix.

10.3 Magnetic Levitation

10.3.1 Theory

The Active MagLev System consists of a circular disc that mimics a rotating circular Halbach Array, positioned beneath a conductor plate. The circular disc was fabricated in-house using a 3D printer to test the fit of magnets supplied by our sponsor, GoudSmit UK, into the casings. Due to the brittleness of PLA material, the casings were constructed from a more durable material.

This circular disc is connected to a Maxon 160W EC90 Brushless DC motor. When the motor is activated, the magnets within the casing generate a lift force. This force is measured using a compression load cell.

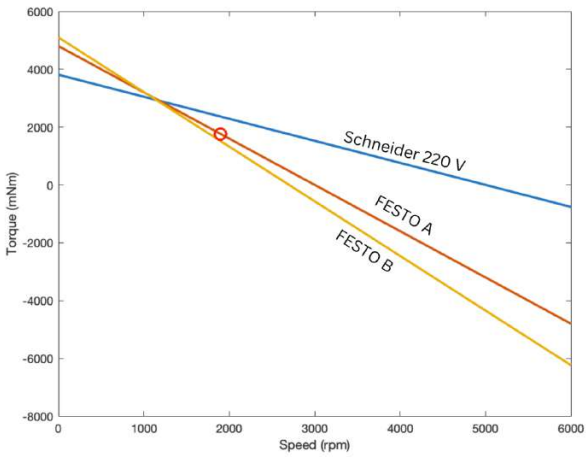

Figure 57: Different motor boundary conditions.

10.3.2 Experimental Setup

The compression load cell, selected for its variable resistance properties, measures the generated lift force. The applied load alters the resistance of the load cell, resulting in a voltage drop. As this voltage drop is minimal, an amplifier is used to process the signal.

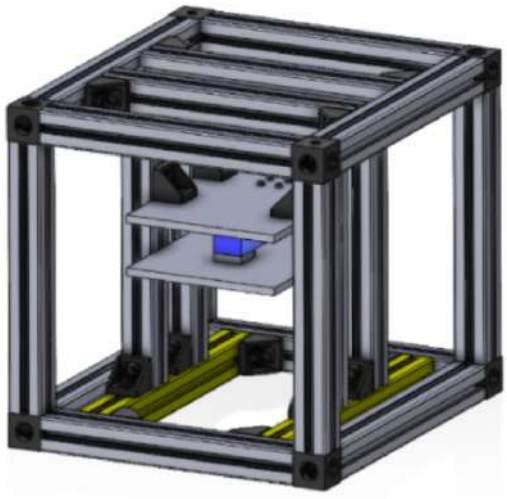

Figure 58: Magnetic Levitation test-rig.

Motor Data		
Values at nominal voltage		
1 Nominal voltage	V	24
2 No load speed	rpm	3170
3 No load current	mA	658
4 Nominal speed	rpm	2720
5 Nominal torque (max. continuous torque)	mNm	457
6 Nominal current (max. continuous current)	A	6.39
7 Stall torque[1]	mNm	7910
8 Stall current	A	111
9 Max. efficiency	%	85

(a) Motor specifications

(b) Motor image

Figure 59: Magnetic Levitation test-rig.

The load cell is sandwiched between two thick aluminum plates and is secured with brackets to prevent any vertical movement along the rig.

To ensure a stable connection between the motor and the disc, the disc is designed with mounting points for M4 bolts, providing a secure attachment.

10.3.3 Magnet Configuration

The current disc design houses 12 N52-grade neodymium magnets arranged in a circular configuration. The magnets are aligned such that their polarities alternate with a 45-degree angular shift between consecutive magnets. This configuration maximizes the magnetic flux and lift force generated during operation.

11 FEA analysis for Mechanical Subsystems.

11.1 FEA

Finite Element Analysis (FEA) is a simulation technique used in engineering that helps with the prediction of an object's response to external forces, heat, and various other physical effects. It is possible to divide the simulated object into smaller, easier-to-understand components known as elements or finite elements. The digital object's elements create a mesh of elements and nodes. The nodes refer to the points located at the tips of the elements. The elements can be made of a variety of shapes: triangles, quadrilaterals, etc. The meshing process in FEA involves the creation of the mesh. The finer a mesh is, the more accurate the results it outputs will be. However, this comes at a computational power cost. The reason for this is that a simulation with a large mesh will take longer to be solved (9).

A set of equations and properties govern each element in the mesh. In structural applications, the properties are related to the material used, and the equations dictating the behaviour of the mesh are usually derived from Newton's laws of motion (9).

When performing FEA simulations, boundary conditions need to be defined. The boundary conditions are restraints on the system, which act as the surrounding environment's interaction with the system. An example of such a condition is structural FEA, which is a fixed support or a distributed load. Once the mesh is created and the boundary conditions are set, the simulation's solution can be solved, which shows the reaction of the nodes and elements. To solve the problem, values such as displacement, strain, and stress are solved all across the mesh. The results from the solution can then be used to analyse the performance of the object simulated. In the field of structures, stress and displacement maps can be created to allow the user to better understand the behaviour of the object under the load simulated. The maps can be useful in identifying large stress concentrations and altering the object's design to reduce them (9).

11.1.1 SimSolid

SimSolid is meshless FEA software that can perform structural simulations on a variety of parts or assemblies. The meshless aspect of the software makes it a very useful tool in analysing structural problems and significantly reduces the time required to pre-process simulations. SimSolid is capable of directly using a CAD file, no matter if it's a part or assembly. This removes the need for simplifying geometries such as fillets or small holes and drastically reduces the need for preprocessing (10).

It is important to note that, although the user does not manually create a mesh, SimSolid automatically meshes the geometry. The software automatically, or "intelligently," increases the mesh density based on the analysis required. This involves using polyhedral mesh elements, which better adapt to irregular shapes. The software produces initial simulation results that are less sensitive to mesh quality. The program is capable of producing accurate and reliable results even using coarser meshes that are adaptively refined depending on stress concentrations and error estimates (10).

11.1.2 Vibrations

The FEA technique for vibrations begins with the construction of the equation of motion for the structure. This equation represents the relation between the mass, damping, stiffness of the structure, and the dynamic forces that are applied. This equation helps with understanding the vibrational loads over time that will be experienced (11).

Modal analysis allows for the finding of the inherent frequencies and mode configurations that the structure has. This is accomplished by solving the eigenvalue issue obtained from the undamped equation of motion which is equal to the squares of the natural frequencies, whereas eigenvectors are for the mode shapes. By solving the equation the eigenvalues and eigenvectors can be found; those offer valuable information on the resonant frequencies of the structure and the corresponding deformation on structure (11).

11.1.3 Buckling

Buckling analysis in FEA uses the stability equations for the structure. This entails comprehending the relation between the exerted loads and the pivotal buckling load. This equation allows for determining the structural response to increasing compression loads (12).

Eigenvalue analysis is crucial for buckling FEA and it entails calculating the critical load factors and the structure's related buckling modes. This is done by solving the eigenvalue problem that comes from the stability equations. In this case, eigenvalues show the load factors at which buckling occurs, whereas eigenvectors show the related buckling modes (12).

11.2 Analysis and Testing of Chassis

11.2.1 Simulation and Optimisation of the Chassis

As previously mentioned, a finer mesh produces more accurate results. In real-life applications, a certain level of accuracy is needed for the specific application. Therefore, a mesh convergence study is performed

to increase the accuracy to the desired level. For the particular accuracy needed, the mesh convergence study ensures that the solution created is independent of the mesh. The study also ensures that the solution requires the least amount of computational power while still maintaining the needed level of accuracy (10).

11.2.2 Material Selection

The material selected for the chassis is aluminium 6061 T6. It has the properties shown in Table 29 (13).

Property	Value
Density	2.70 g/cm^3
Ultimate Tensile Strength	310 MPa
Yield Tensile Strength	276 MPa
Modulus of Elasticity	68.9 GPa
Shear Strength	207 MPa
Fatigue Strength	96.5 MPa
Thermal Conductivity	167 W/m-K
Melting Point	582-652°C
Hardness (Brinell)	95 HB

Table 29: Material Properties of Aluminium 6061-T6

The chosen material needed to be weldable due to manufacturing constraints, which limited the possible choices. In Figures 60, 61, and 62, Ashby plots of Aluminium 6061 T6 in comparison with a variety of other materials are shown. The plots examine the relationships between density, Young's modulus, and yield strength and show that the chosen material has a relatively low density and performs very well in terms of yield strength and Young's modulus. The figures show that better-performing materials exist; however, their price is much higher than the cost of the chosen aluminium.

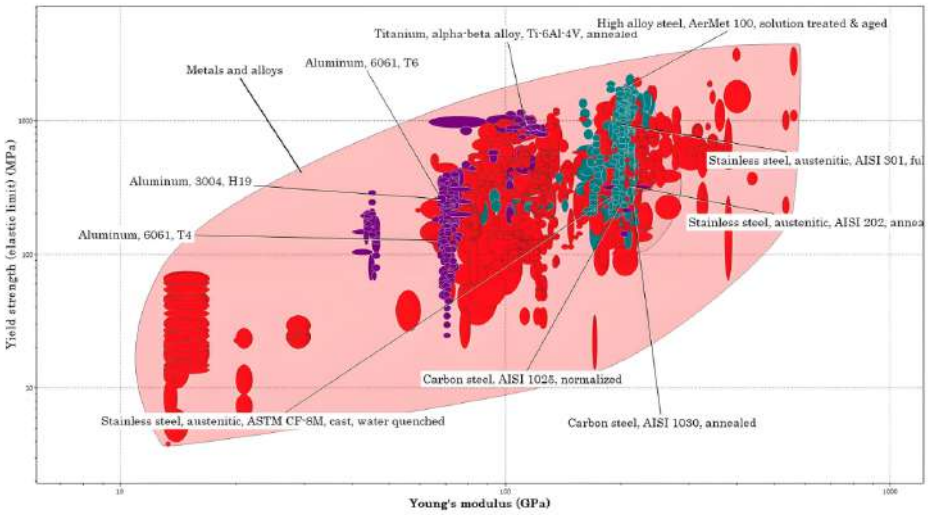

Figure 60: Ashby plot of Young's modulus vs yield strength

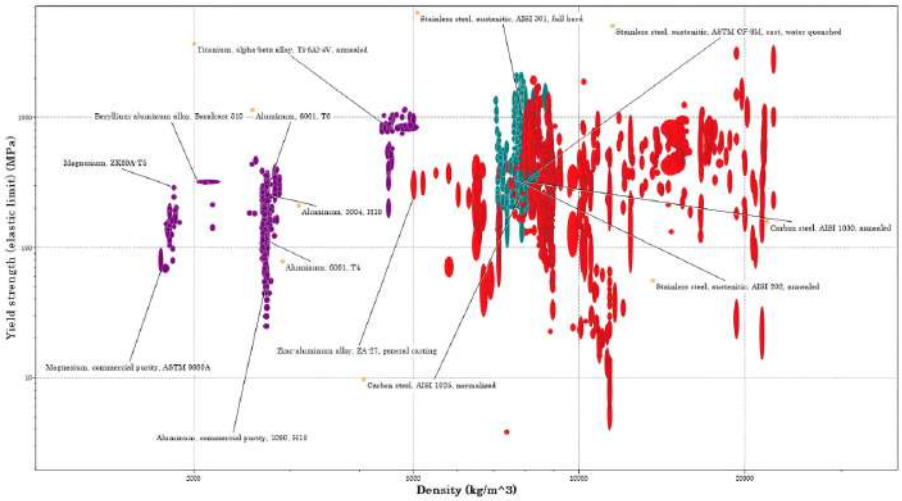

Figure 61: Ashby plot of density vs yield strength

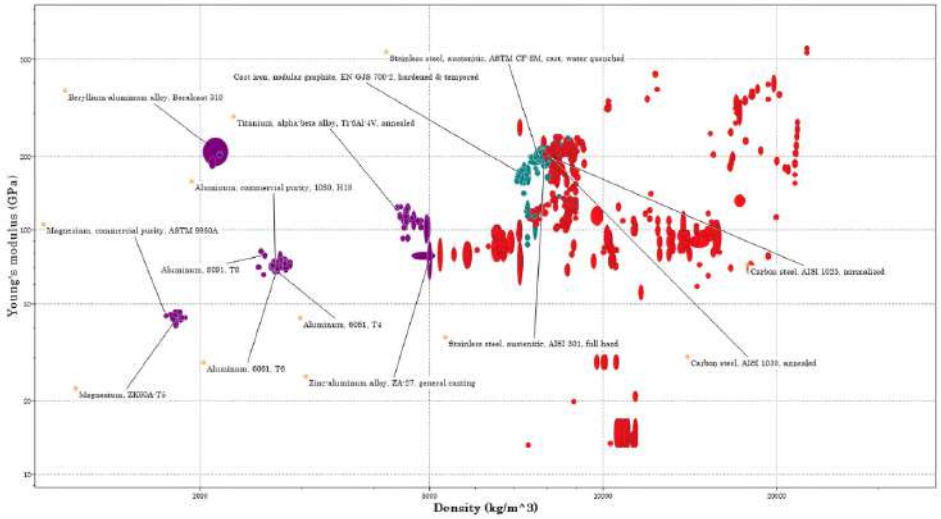

Figure 62: Ashby plot of Young's modulus vs density

11.2.3 Chassis Simulation Method and Strategy

To optimise the chassis design for weight, the simulation strategy outlined below has been undertaken. The simulations have been split into three separate phases: the main chassis structure simulations, the side suspension weldments, the side and vertical suspension mount simulations, and finally, the braking mounts and weldments simulations. The simulation phases have been carried out in the aforementioned order.

During each simulation phase, the complete pod assembly is simulated together. If any component of the assembly has not been designed in detail at this point in the simulation process, its preliminary design is employed in the assembly. This collective rather than isolated simulation approach ensures that the loads applied to the chassis are realistic and allows for better visualization of the effect of the chassis design on the complete pod's structural behavior. It is important to note that this approach increases the computational power requirements.

For each phase, the iterative optimisation process shown in Figure 63 has been undertaken.

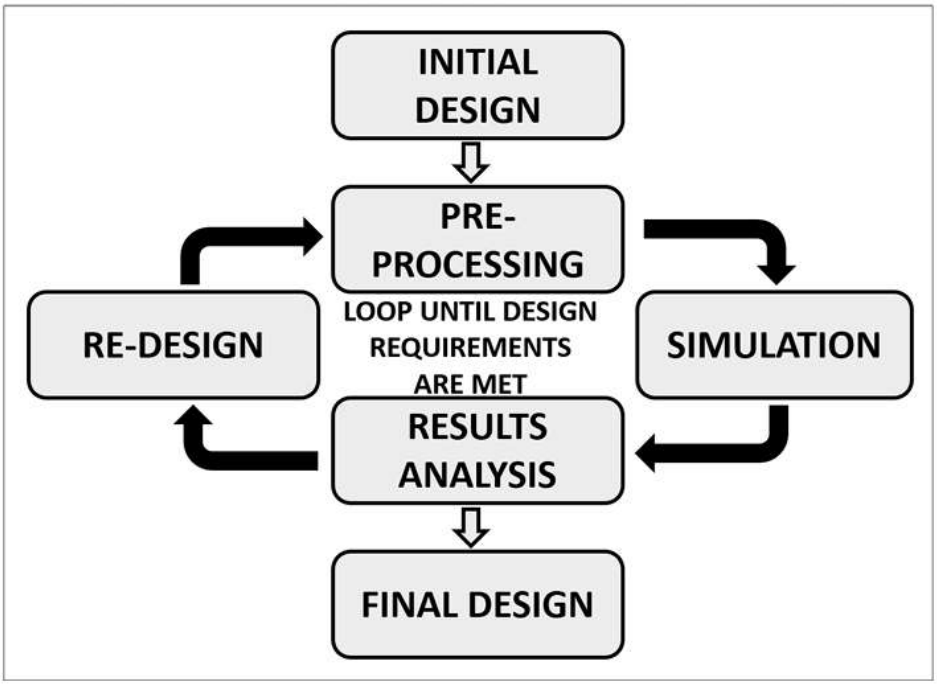

Figure 63: Optimization strategy

Several types of simulations have been performed for all phases; however, there are two main ones that have been carried out on all iterations. The first one is the acceleration load case simulation. This simulation shows the behavior of the structure when the linear induction motors accelerate the pod. The applied inertia loads are 59.92 m/s^2 in the z-direction and -19.62 m/s^2 in the y-direction to simulate gravitational acceleration. Additionally, a load of 30 N with an angle of 30 degrees has been applied to the outer shell mounts.

The brake load case is the other main simulation case. This simulation shows the behavior of the structure when the braking units decelerate the pod. The same aerodynamic loads have been applied as in the acceleration case, assuming their value does not change due to rapid deceleration. A fixed support in all three axes has been applied to the braking units.

During all simulations, the vertical suspensions, side suspensions, braking units, middle components, maglev units, LIMs, and LIM mounts have been assumed to be fully rigid bodies. This ensures body mass is preserved while preventing deformation. For reference, the vertical suspension consists of shafts holding together two 10 mm-thick iron plates attached to the aluminium extrusion, providing high stiffness. Fasteners, bolts, and nuts have also been assumed to be fully rigid bodies due to their high stiffness.

11.2.4 Conclusion of FEA analysis

In **??** can be seen the final iteration of the main chassis structure. In this iteration, additional reinforcing members have been added to counteract the braking unit moments. In this iteration, the main structure's mass is 2804 grams. This is a 234-gram increase from the previous iteration. Upon examining the stress

and displacement contours, it can be seen that the maximum displacement during braking is 0.82 mm and the maximum stress is 70.53 MPa. Upon acceleration, the maximum displacement is 0.70 mm, and the maximum stress is 22.52 MPa. In both load cases, the maximum stresses are once again significantly lower than the yield strength of the material, which is 241 MPa. However, the displacement is lower than the maximum allowed value of 1 mm. Therefore, the mass of the structure can be once again further reduced at the cost of a higher displacement that is still below 1 mm.

The displacement contour shape is very similar to the previous iteration. The stress contours also bear a striking resemblance to the previous iteration. The added member further counteracted the braking unit moment, reducing the displacement to an acceptable range. The location of the highest stress has changed between the left and right sides. This can be explained by the small inaccuracy of Simsolid. The symmetry of the chassis should theoretically result in the same stress at two symmetrically opposed points (the symmetry plane runs lengthwise and vertically). However, the solver creates minute differences in the values, and hence the stress of an opposing point on one side is insignificantly bigger and gets marked by the software as having the largest stress. This is further confirmed by the symmetric shape of all the displacement and stress contours.

The final mass of the chassis comes to 12.2 kg. This is lighter than the set target of 15 kg and hence this optimization has been successful. It can be seen in the buckling and vibrations that the structure will not fail due to those effects, the reason for this is that the buckling factor is higher than 1 and the lowest natural frequency is higher than the requirement of 25 Hz. It is important to note that negative buckling factors have been ignored, as they do not mean the structure will buckle under the simulated conditions. Finally, it can be seen from the other figures shown that the displacement is lower than 1 mm for all iterations. Hence, the structure will not fail.

Table 30: Natural Frequencies and Buckling Factors

Buckling: Braking	Buckling: Acceleration	Freq: Maglev and LIM Fixed (Hz)	Freq: Braking Fixed (Hz)	Freq: Suspension Fixed (Hz)	Freq: Suspension Fixed (Hz)
-1.4	-2.32	38.27	28.5	88.25	-1.79
-2.2	38.56	31.23	88.36	-3.8	3.18
61.87	54.8	90.79	-8.35	4	62.19
80.46	91	-1.04	5.13	81.65	84
119.4	12.49	-5.69	82.36	108.11	120.1

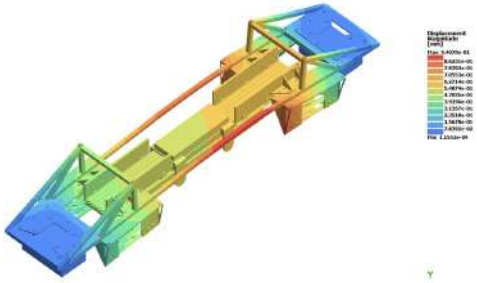

Figure 64: Final Displacement at Braking.

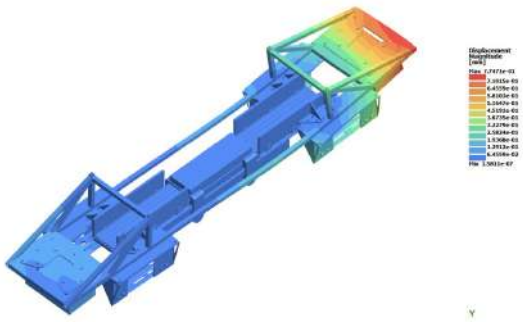

Figure 65: Final Displacement at acceleration.

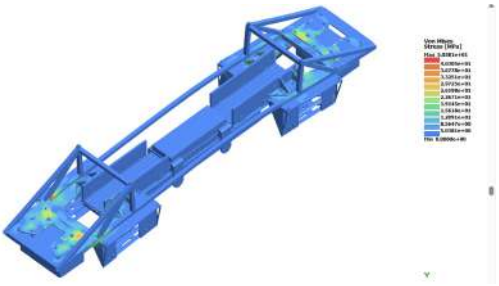

Figure 66: Final Stress at Braking.

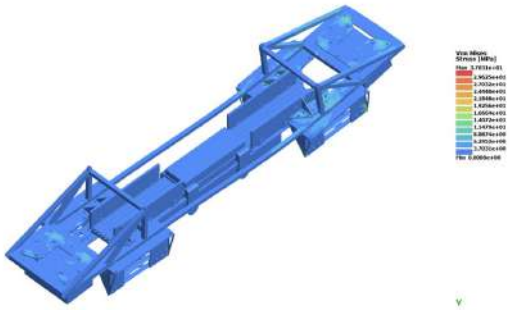

Figure 67: Final Stress at acceleration.

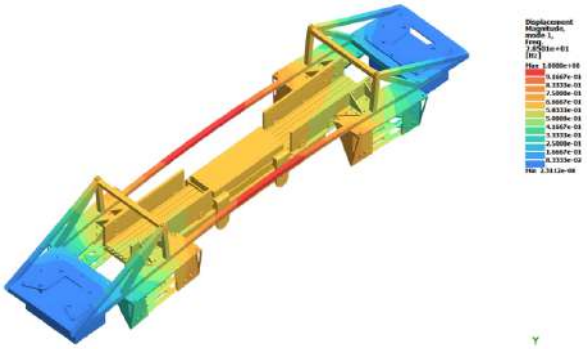

Figure 68: Lowest Natural Frequency

11.3 Braking and Suspension: Testing and Analysis

The objective of this Finite Element Analysis (FEA) is to identify potential stress concentrations and points of failure within the friction braking system. This includes analysis of the rods, casing and attachment plates in the braking system. The FEA is set up with the assumption that the shear forces as a result of the braking forces are taken up by the liner rails. This is to take into account the worst case scenario where the rods are not supported by the rest of the casing. Thereafter, the normal force (green arrows) is simulated on the rest of the casing and assembly. The normal force FEA was set up as seen in the image above and the results from the shear force analysis on the rod is below.

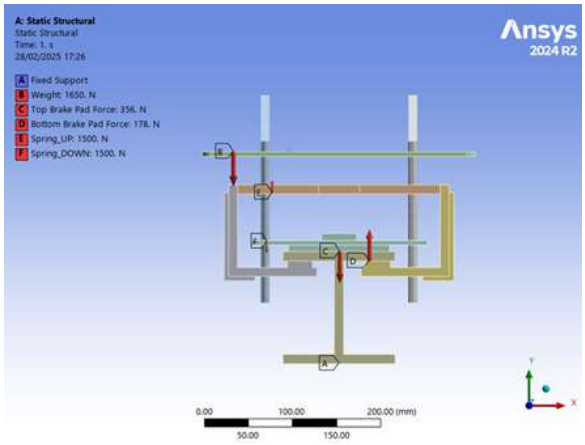

Figure 69: Supports and Forces acting on the braking system.

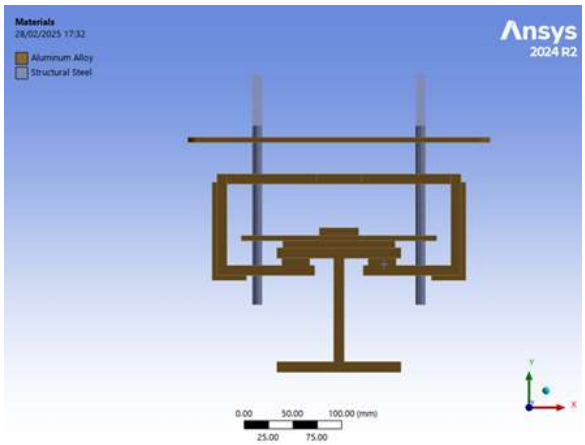

Figure 70: Material properties of the system.

11.3.1 Braking System Failure Mode and Effects Analysis (FMEA)

Component	**Failure Mode**	**Effect of Failure**	**Possible Cause**	**S**	**O**	**D**	**RPN**	**Recommended Action**
Pneumatic actuator	Pressure lost	Brake doesn't apply	Leak or valve stuck	9	5	3	135	Use fitting rated to operating pressure with safety factor
Spring	Breaks or weakens	Not enough force to stop	Metal fatigue or bad material	8	4	4	128	Use tested springs, check regularly
Brake pad	Wears down or falls off	Low braking or total failure	Too much heat or vibration	9	6	4	216	Secure pad with bolts and ensure melting temperature is not reached
Bushing	Warps or comes loose	Parts don't align, may jam	Loose fit or hit during use	6	3	5	90	Tighten tolerances, inspect during maintenance
Linear rails	Jammed or bent	Brake actuator gets stuck	Misalignment, debris, overload	8	3	4	96	Conduct FEA to ensure rails do not shear
Solenoid valve	Stuck open or closed	Brake stays on or off	Dirt, faulty part, no power	7	4	4	112	Conduct regular valve inspection

Component	Failure Mode	Effect of Failure	Possible Cause	S	O	D	RPN	Recommended Action
Actuator housing	Cracks or deformation	Misalignment, internal jamming	Impact or overload	7	1	4	28	Use actuator within operating pressure with safety margin
Mounting brackets	Loosen or shear	Brake falls off or moves under load	Vibration, poor fastening	8	2	3	48	Use locking nuts/bolts, inspect torque settings regularly

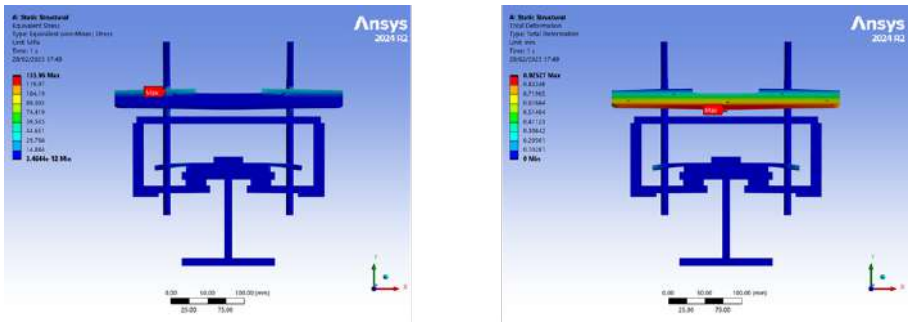

Figure 71: Stress and Deformation of the brakes.

It can be seen that the stresses reached in the majority of the rod are below the yield stress. The normal force FEA provides the following results where the rest of the assembly does not yield.

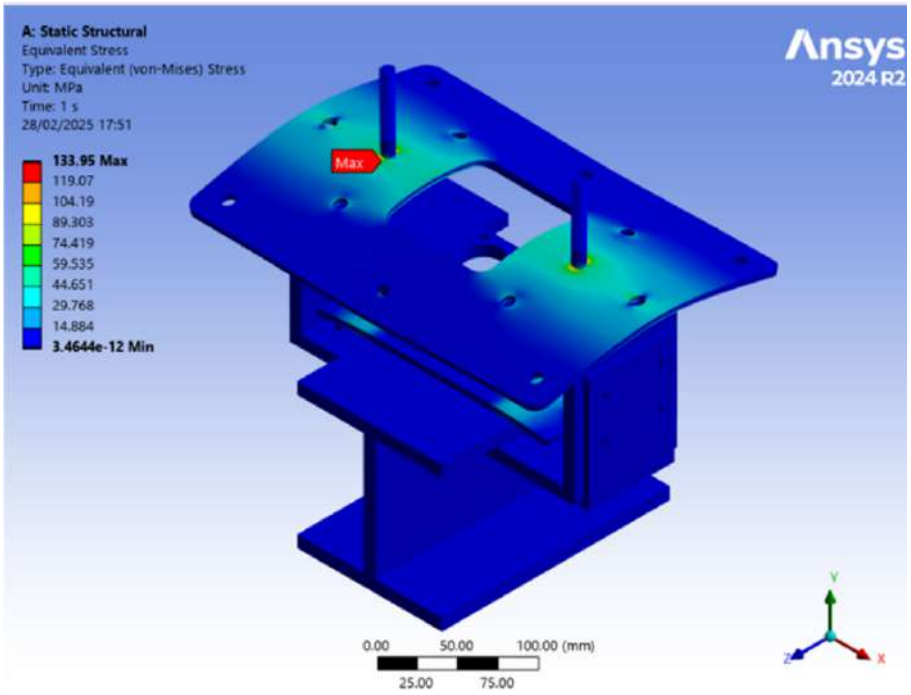

Figure 72: Von-mises stress acting on brake

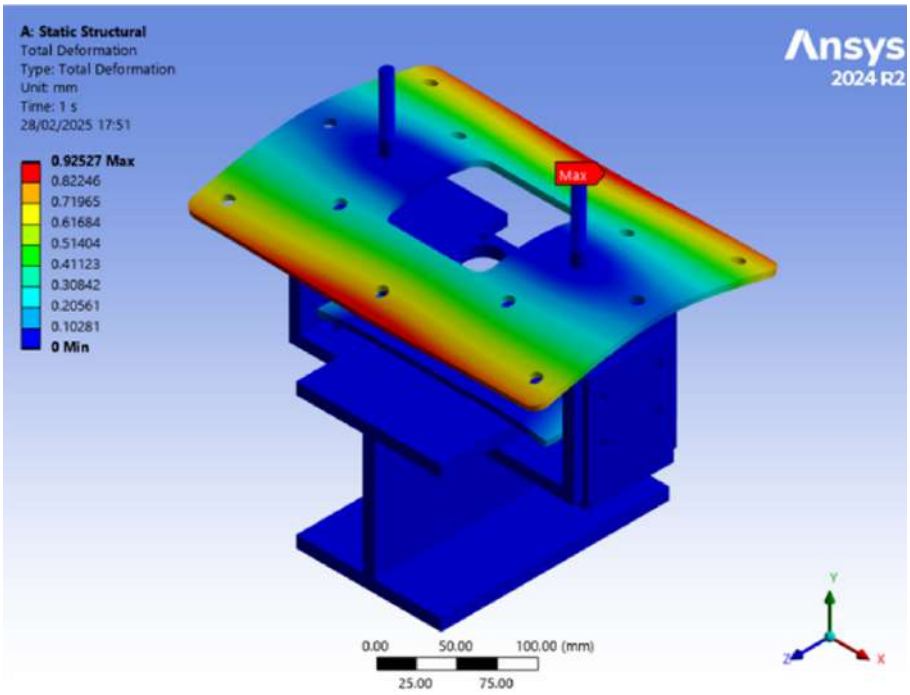

Figure 73: Total deformation of the brakes

11.4 FMEA Suspension

Top Suspension Failure Mode and Effects Analysis (FMEA)

Mode of Failure	Cause of Failure	Effect of Failure	O	S	D	RPN	Required Action
Actuator fails to retract wheels	Actuator cannot overcome damper force, air leakage, seal degradation, control signal loss	Wheels remain extended during levitation	3	9	4	108	Use powerful actuator, regular maintenance, control checks
Damper loses damping effect	Fluid leakage, incorrect adjustment	Excessive vibration to structure, mechanical failure	4	8	4	128	Use quality Öhlins dampers, maintenance, vibration monitoring
Incomplete or slow retraction	High compression force, underpowered actuator	Incomplete retraction, compromised lift-off	3	6	3	54	Use powerful actuator, test timing under load
Rocker arm, wheel shaft, side plates fracture	Overload, poor motion ratio, fatigue	Structural failure or collapse	5	10	5	250	Proper material selection, fatigue testing

Bottoming out during emergency braking	Spring too soft, low damper force	Pod hits track, damages maglev ski	4	10	5	200	Spring redesign, dynamic braking testing
Bearing jam prevents retraction	Bearing slides or gets stuck	Wheels stay deployed, levitation failure	2	8	2	32	Check alignment, lubrication, tolerance adjustments
Incorrect retraction motion	Rocker arm sliding instead of rotating	Unpredictable motion, misalignment	3	8	4	96	Tolerance adjustment for side plate-rocker arm interface

Side Suspension Failure Mode and Effects Analysis (FMEA)

Mode of Failure	**Cause of Failure**	**Effect of Failure**	**O**	**S**	**D**	**RPN**	**Required Action**
Main wheel bearing seizure	Inadequate lubrication, contamination	Wheel stops, friction, guide damage	3	8	4	96	Lubrication schedule, inspection, bearing quality
Wheel surface degradation	Friction, fatigue, poor material	Inconsistent guidance, vibration	5	6	3	90	Regular inspection, wear thresholds, better material
Shaft fatigue failure	Cyclic loading, keyway stress	Wheel loss, derailment	3	9	5	135	FEA, fatigue testing, inspections
Vertical wheel misalignment	Poor install, bolt loosening, impact	Vibration, reduced stability	4	7	4	112	Precision install, alignment checks
Damper spring failure	Fatigue, defects, overextension	Poor stability	3	7	5	105	Material testing, cycle analysis, replacements
Rocker shaft shearing	Lateral forces, defects, fatigue	Loss of suspension function	2	10	4	80	Strength verification, diameter optimization
Rocker arm fracture	Impact, fatigue, defects	Geometry loss, wheel movement	3	9	4	108	Reinforcement, fatigue analysis, inspections
Front chassis bracket failure	Vibration, fatigue, poor install	Misalignment, potential failure	3	8	4	96	Bracket reinforcement, secure fitting, vibration check
Rear chassis bracket failure	Fatigue, impact	Instability, mounting loss	3	8	4	96	Material and stress analysis, inspections
Secondary shaft shearing	Shear stress, defects	Reduced redundancy	2	8	5	80	Diameter optimization, material review

Damper spacer dislocation	Vibration, poor install	Damper misalignment	4	5	3	60	Locking mechanism, secure fit
Wheel shaft housing crack	Stress, impacts	Shaft misalignment	3	7	5	105	Reinforcement, stress optimization
Wheel-beam friction loss	Surface issues, wear	Slippage, poor control	4	7	4	112	Surface treatment, monitoring, protection
Rocker spacer failure	Load crushing, install error	Geometry issues, damping variance	3	6	4	72	Strength verification, correct install
Fastener loosening	Vibration, improper torque	Misalignment, noise, failure risk	5	7	3	105	Locking fasteners, torque protocols

11.5 Suspension FEA

This FEA simulates the load case when the actuator is retracted and is acting against the forces of the damper. In this simulation we used a force of 1980 newtons for both the actuator and damper, this was done with the assumption that the pod has a mass of 200kg (to take a safety factor of 2 into consideration).

We can see from the stress contours that the maximum stress occurs between the clevises on the rod, this is expected as the damper and actuator exerts forces in opposite directions. In reality the maximum stress will most likely occur on the welded joints between the clevis and the rod. The maximum stress is at 149 MPa, with a maximum displacement of 0.14mm

This FEA simulates the load case when the side suspension wheels are clamping the middle part of the I beam due to the forces of the damper, however we have made the wheel a fixed support to simulate the stresses within the rocker arm itself.

From the contours we can see that the maximum stress is 153.83 MPa, which tells us our rocker arm will be able to withstand the loads due to the damper.

11.5.1 Side Suspension FEA

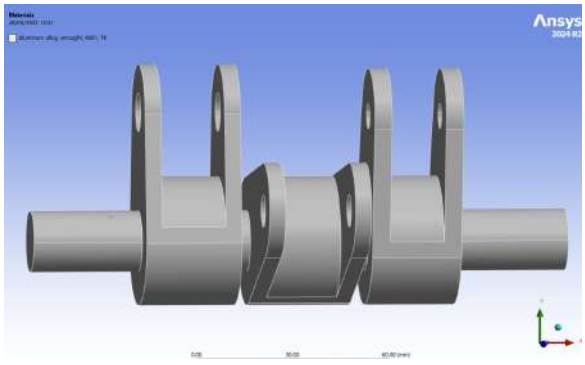

Figure 74: Material Suspension.

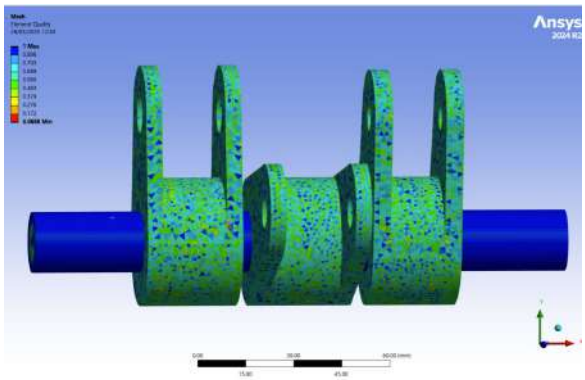

Figure 75: Mesh Suspension.

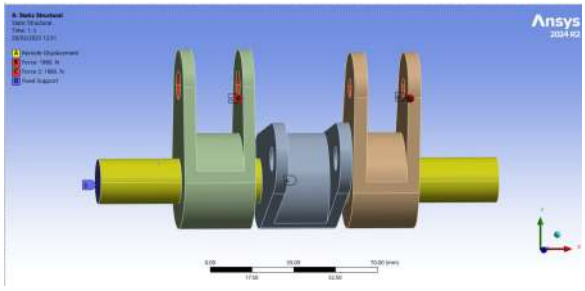

Figure 76: Supports FEA.

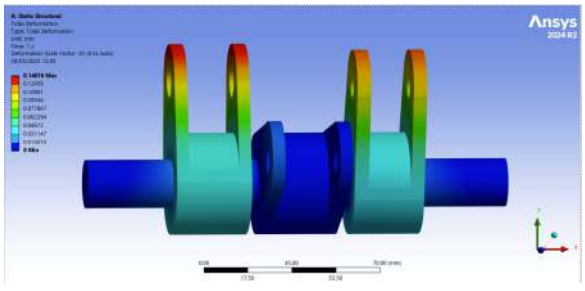

Figure 77: Deformation FEA.

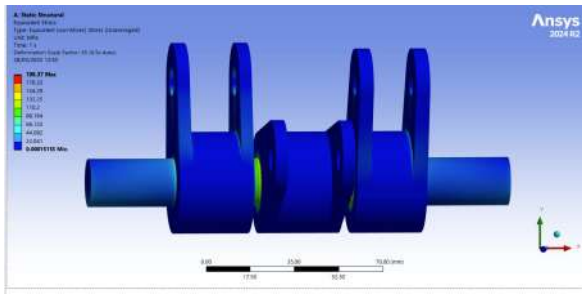

Figure 78: Stress FEA.

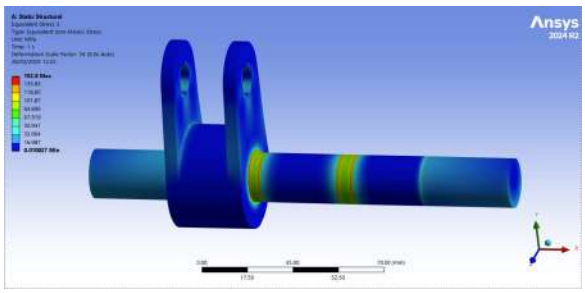

Figure 79: Stress combination FEA.

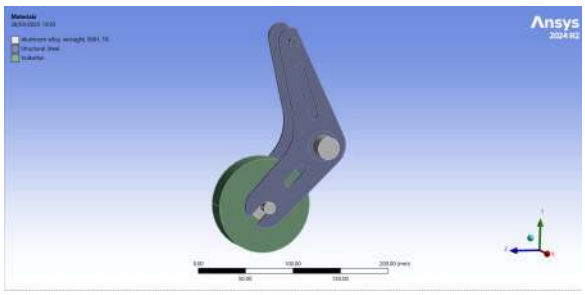

Figure 80: Wheel material.

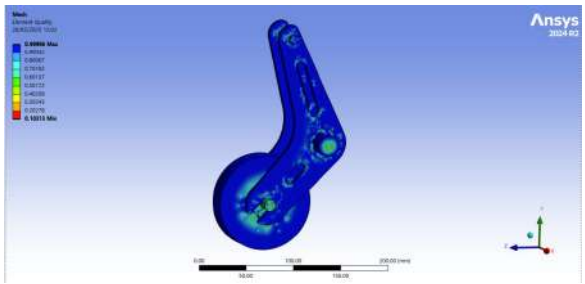

Figure 81: Wheel mesh.

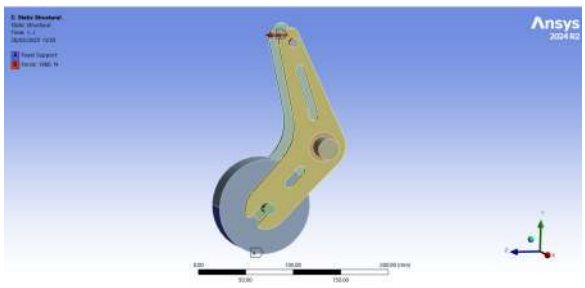

Figure 82: Wheel supports.

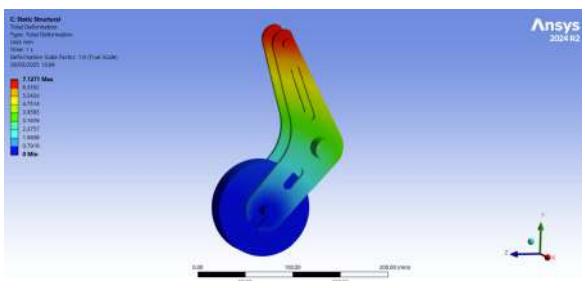

Figure 83: Wheel deformation.

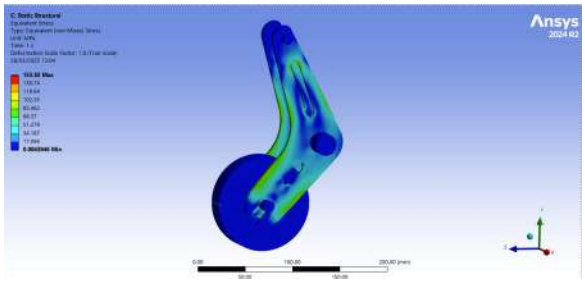

Figure 84: Wheel stress.

11.5.2 Top Suspension FEA

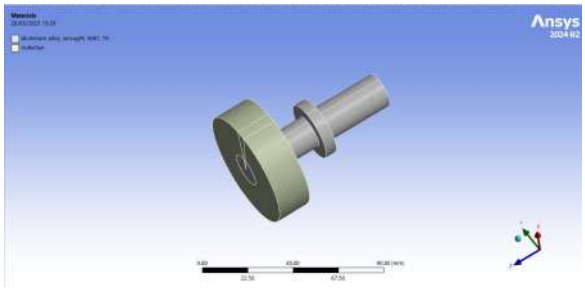

Figure 85: Wheel Material.

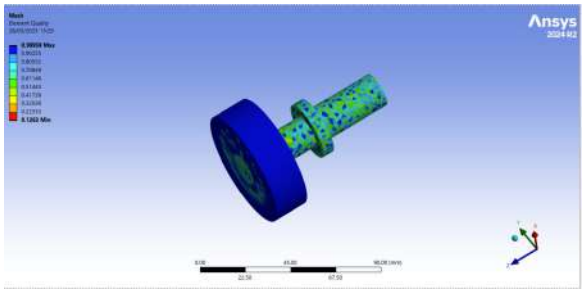

Figure 86: Wheel Mesh.

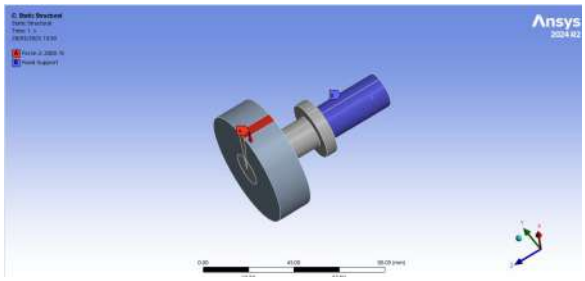

Figure 87: Wheel Supports.

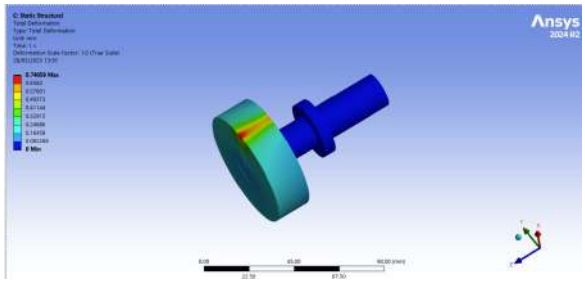

Figure 88: Wheel Deformation.

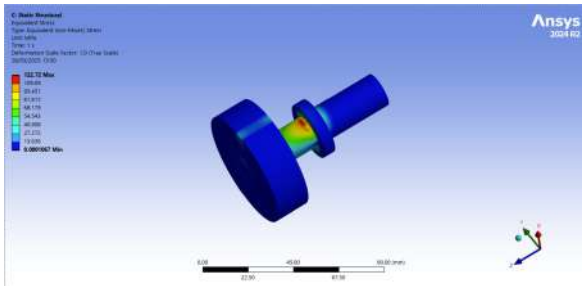

Figure 89: Wheel Stress.

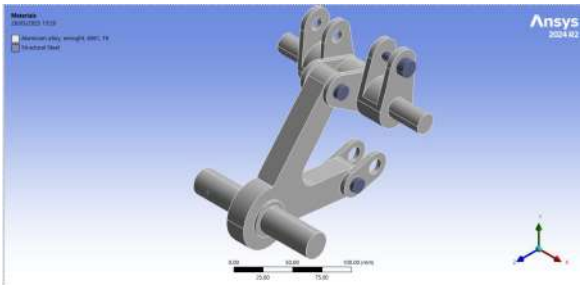

Figure 90: FEA for top suspension.

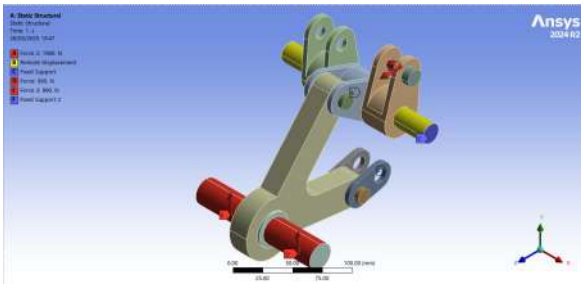

Figure 91: Support top suspension.

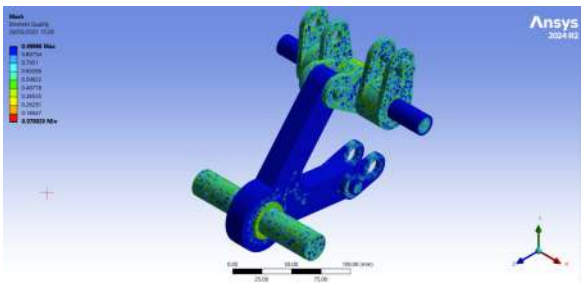

Figure 92: Mesh top suspension.

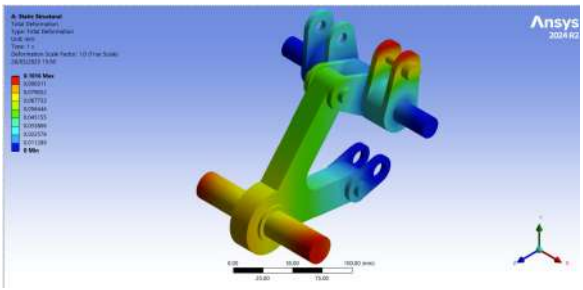

Figure 93: Support top suspension.

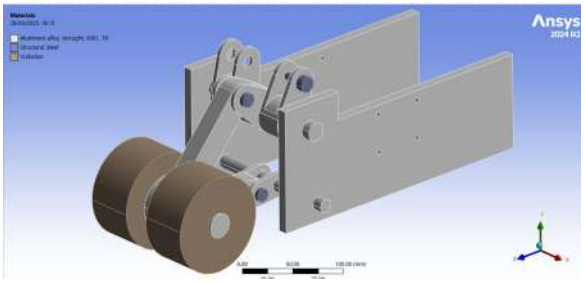

Figure 94: Material rough top suspension.

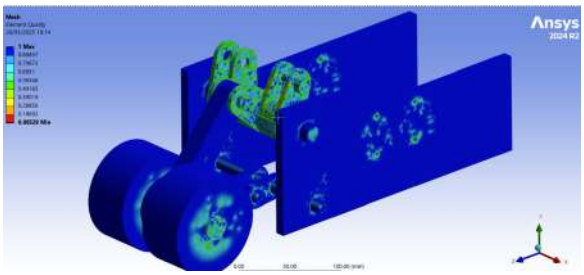

Figure 95: Mesh top suspension.

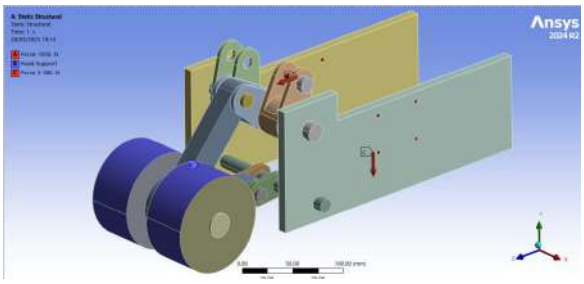

Figure 96: Supports top suspension.

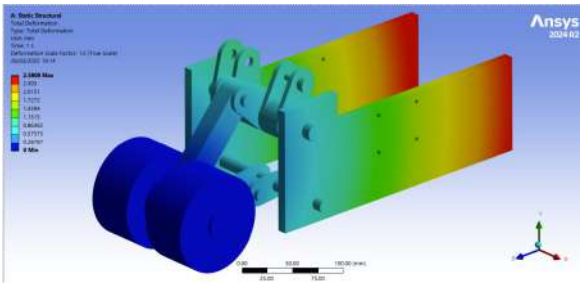

Figure 97: Deformation of top suspension.

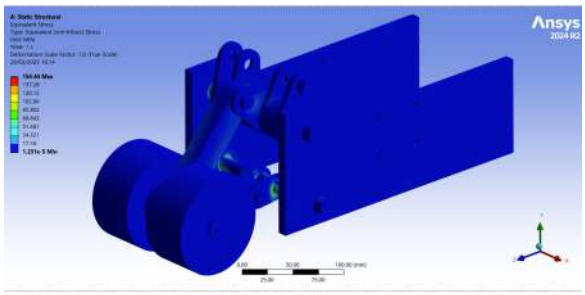

Figure 98: Stress top suspension.

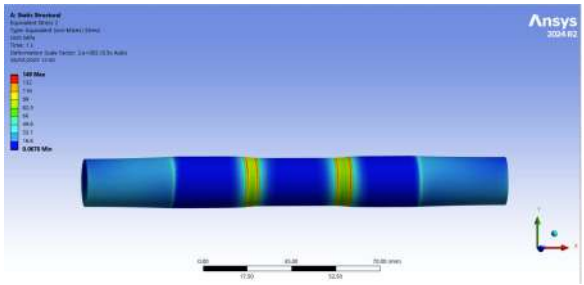

Figure 99: Stress rod FEA.

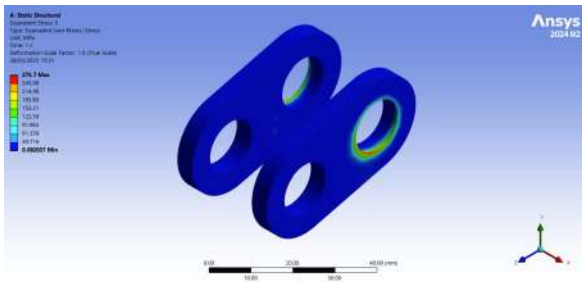

Figure 100: Stress top suspension holder.

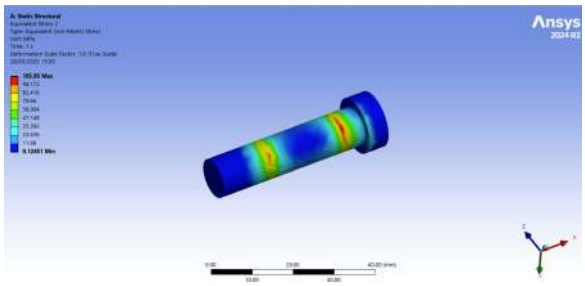

Figure 101: Stress holder pin.

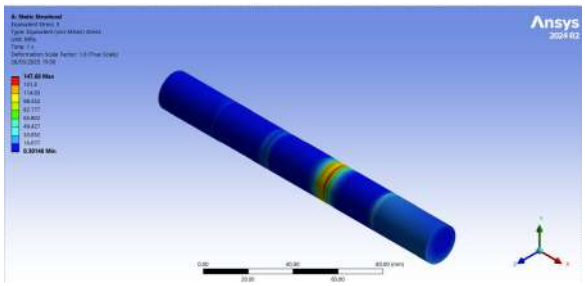

Figure 102: Stress connecting rod 1.

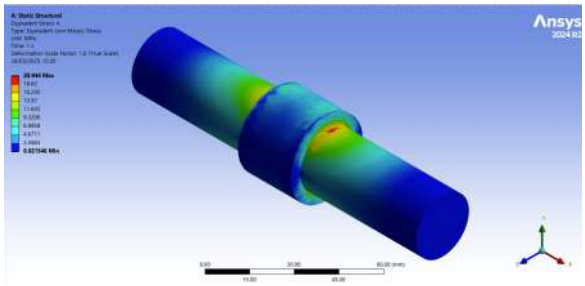

Figure 103: Stress connecting rod 2.

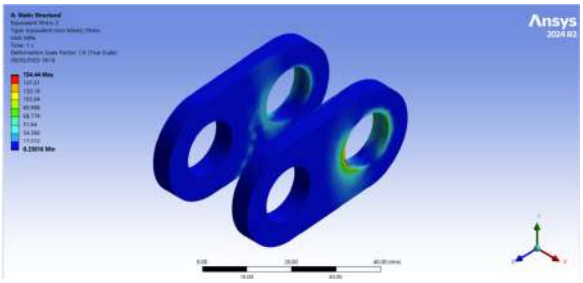

Figure 104: FEA of connecting holder 1.

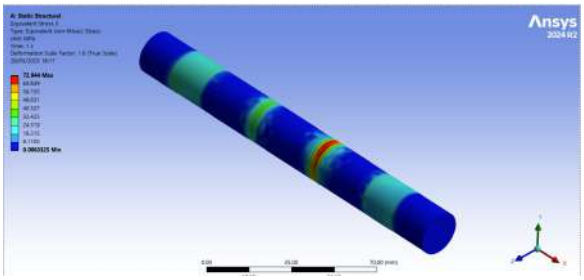

Figure 105: FEA of connecting holder 2.

This FEA simulates the load case when the pod levitates too high, and the safety wheel on our side suspension hits the underside of the top flange of the I beam. We have taken a worst case scenario of 2000 newtons from the force generated from the lift due to the maglev that each wheel has to be able to endure. This simplified model does not show the housing to which the shaft is connected to, but we can still simulate it by making the end of the shaft a fixed support.

From the contours we can see that the maximum stress occurs right on the edge of the larger diameter of the shaft, with a maximum value of 122.72 MPa, this tells us that our shaft will be able to endure the loads of the pod levitating too high. We can also see from the displacement contour that the wheel has the maximum displacement of 0.741mm, as our wheel is made out of Vulkollan, a type of polyurethane, allowing it to deform slightly and absorb some of the forces.

12 Braking FBD

During acceleration weight transfers from the front and the rear. The magnetic acceleration provides the forward thrust transferring the load through the suspension. Under steady conditions the pods total weight will be split evenly between the front and rear of the suspension system.

The reaction force due to the contact between the wheels and the rail.

The spring damper ensure controlled vertical and longitudinal movement of the top wheel relative to the pod body, smoothing out any shocks while transmitting braking loads.

Text BoxThe spring damp force resists the relative motion between the wheel and chassis. This controlled resistance helps manage large dynamic loads that can occur during abrupt braking at high speeds.

The central rail supports the actuator and connects to the pods main body. The actuator applies a vertical force this force can control the position of the pod relative to the rail.

The Springs also supply vertical support, When the wheel moves up or down the spring extends of compresses smoothing the ride.

When the pod breaks friction is generated due to the contact between the wheel and rail exerting a horizontal force opposing the motion of the pod causing it to decelerate.

Similar as with 107 but where the suspension system is under breaking

During breaking the weight transfers from the rear to the front of the system. The brake pads are in contact with the rail generating a frictional force that oppose the motion of the pod causing it to decelerate.

The during breaking the front spring compress and the rear spring extends by some displacement (x) and the spring exerts some force ensuring ride stability absorbing shock during breaking.

13 Suspension FBD

Top Suspension

The wheel interacts with the guide rail under braking, transferring frictional forces into the spring–damper system and ultimately into the pod chassis, all while the magnetic levitation from below provides the main lifting force.

Each labelled arrow indicates a force contributing to the overall balance, normal reaction, friction (braking), spring force, damper force, and the net propulsion/braking force ensuring controlled motion and safety at high speeds.

The total weight of the pod acts downwards. The mag lev force, the magnetic levitation system generates upwards force. The Reaction force N supported force from the wheel.

The sum of the upward forces must equal the downwards force. Ensuring that the system is in equilibrium (W=MaglevForce + ReactionForce).

F propulsion is the net driving force accelerating the pod. F drag is the force due to aerodynamic resistance. F friction is due to the rolling resistance of the wheel.

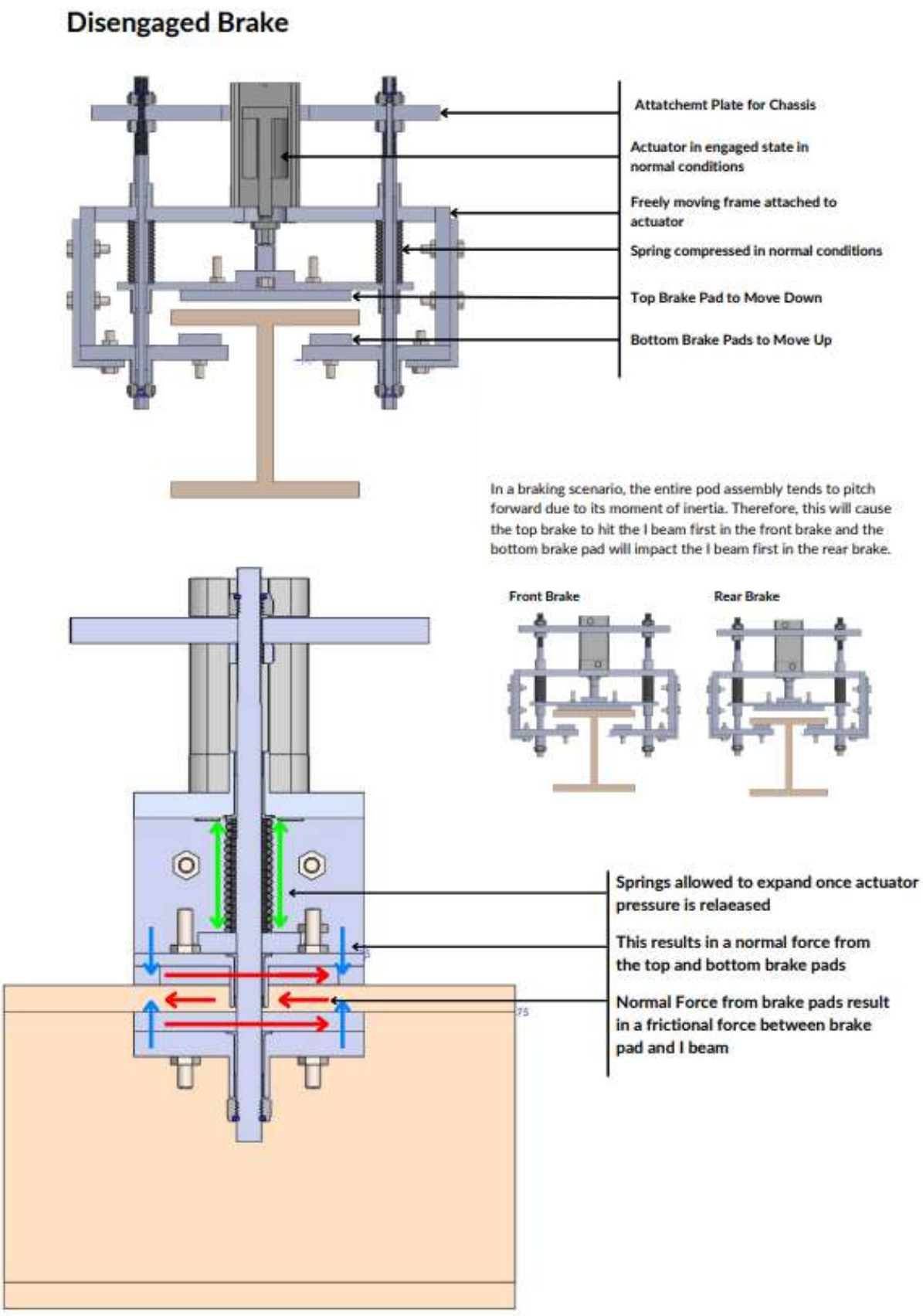

Figure 106: Free body diagrams for braking.

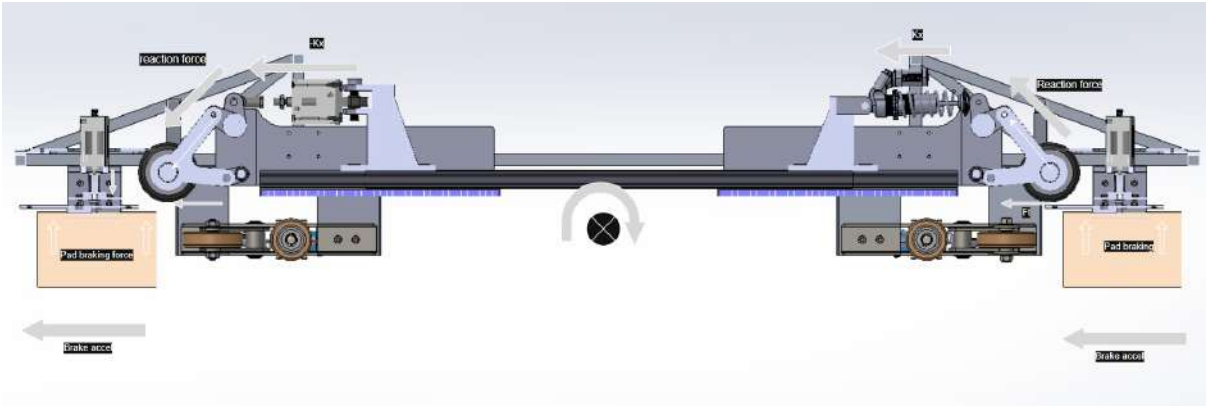

Figure 107: Chassis FBD

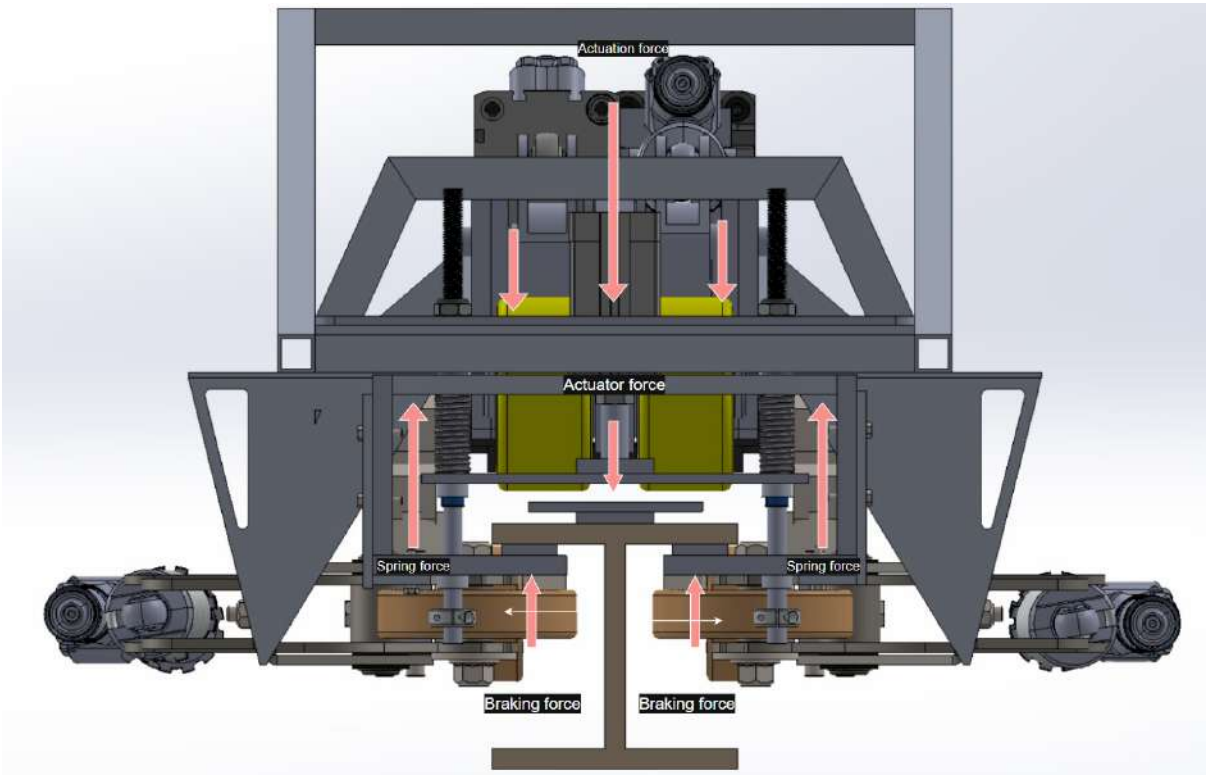

Figure 108: Braking and Suspension FBD with combined loads

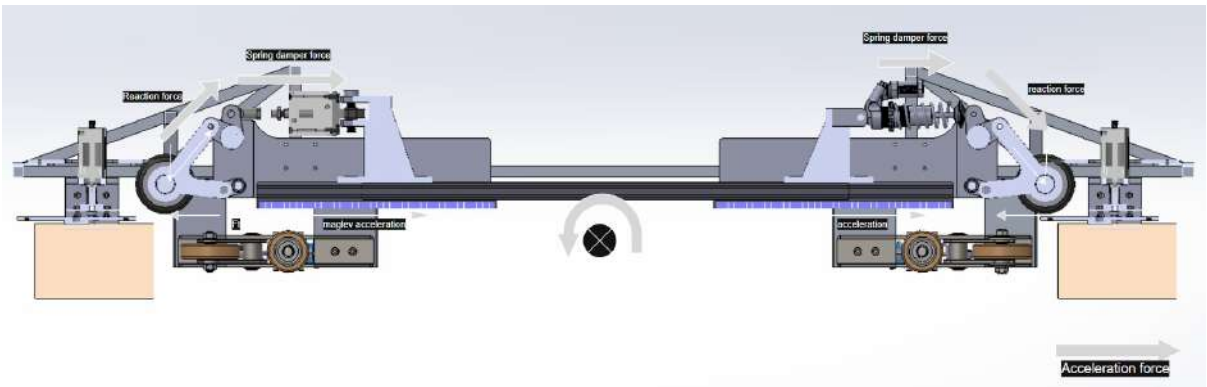

Figure 109: Suspension FBD

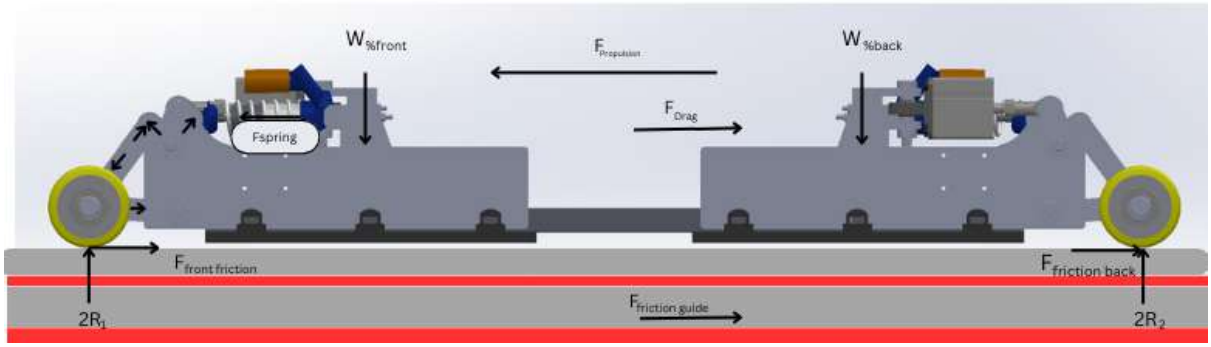

Figure 110: Free body diagrams of Suspension with acceleration and without Maglev.

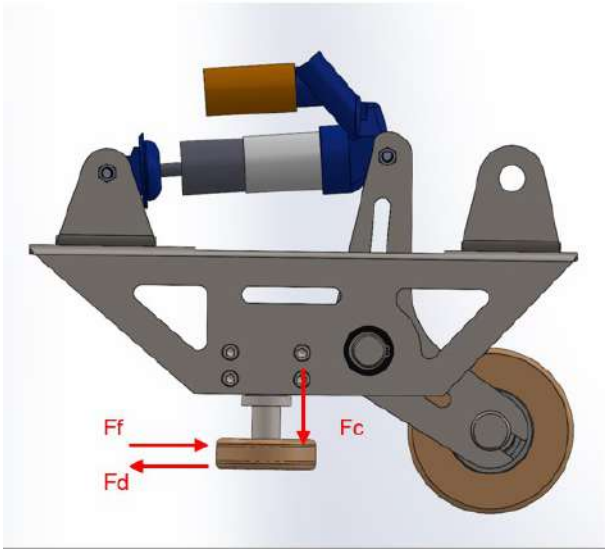

Figure 111: Free body diagrams of Suspension with side view.

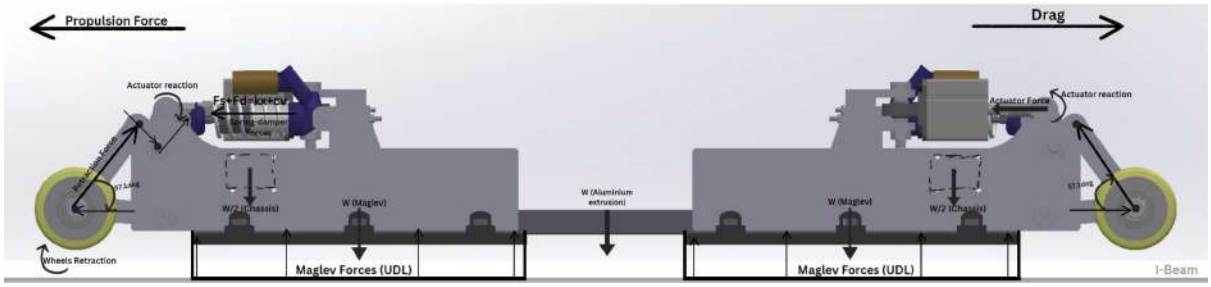

Figure 112: Top Suspension acceleration with maglev.

Text BoxA person in a blue hat and blue suit on a machine

The normal forces on the wheels are defined as: Nfront=k[Wmaglev] and Nback=(1k)[Wmaglev]

The total normal force must equal W-mag lev force this force is split by k ensuring the front and rear carry the same proportion of the load. So that Nfront+Nback=Wmaglevforce.

The damper force is defined as: F damper=Nsin()cos()+F friction

The damper force is dependent on the normal load and geometric factors that account for the angle of the damper relative to the wheel and any friction from the dampener or linkages.

Wheel friction caused between contact between the wheel and the track and rotational friction, friction

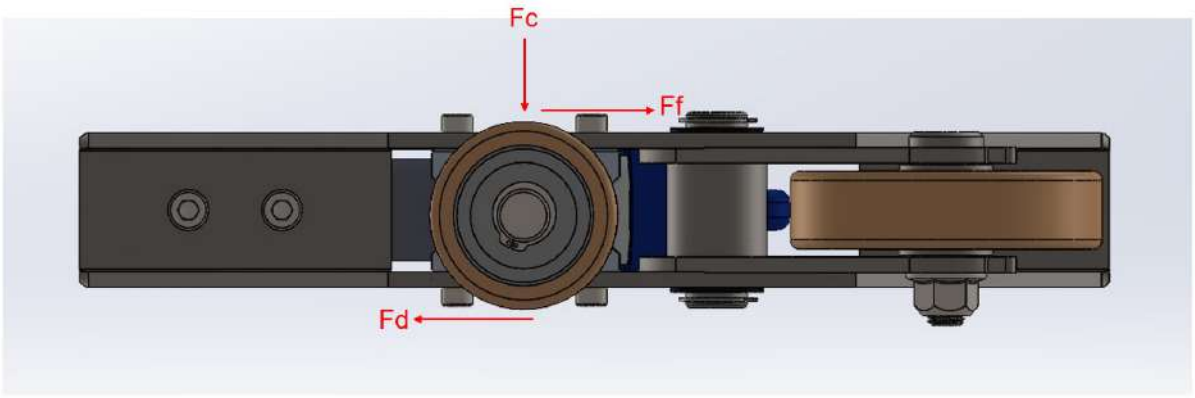

Figure 113: FBD suspension Topview

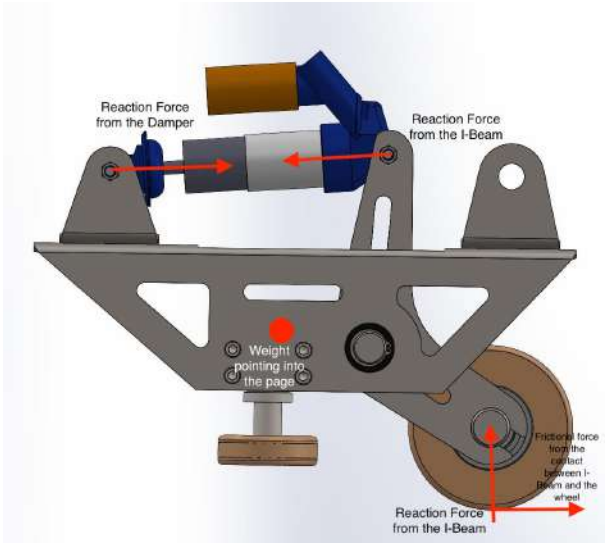

Figure 114: Side suspension acceleration

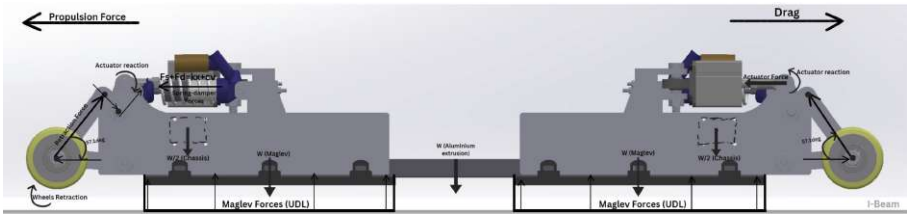

Figure 115: Suspension acceleration FBD

caused in the wheel bearings, axle friction and internal rolling resistance due to wheel rotation so that Friction=Wheelsfriction + Rotationalfriction.

The sum of wheels friction (contact patch) and rotational friction (bearings/axle) forms the total frictional resistance

The pod's horizontal acceleration is determined by Ma=Fpropulsion(frictions). If Fpropulsion¿frictions, the pod accelerates.

During Certain phases e.g. emergency scenario, maintenance the hyperloop relies on the wheel as apposed to the levitation. In this scenario the wheels support the pod's full weight, which is distributed between the front and rear suspension systems.

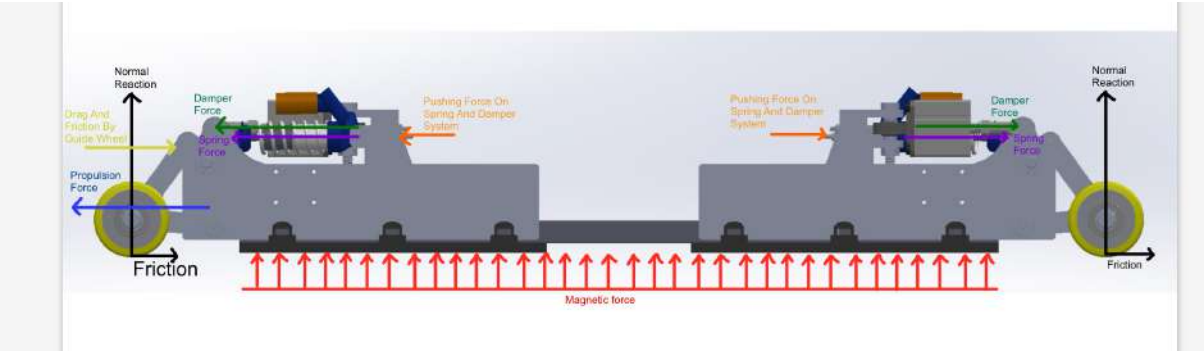

Figure 116: Top suspension FBD

The vertical reaction at each wheel is represented by 2R ensuring that without magnetic lift, all of the weight is carried by the front and rear wheels.

F propulsion is the net forward driving force, while F drag opposes the motion of the pod caused by aerodynamic drag and F friction caused by rolling friction due to the wheels.

Under load the spring either compresses or extends a force on the system (F spring) absorbing any vibrations and transmitting forces in the system ensuring the pod travels smoothly along the rail.

The pod's total weight is the sum of several components, these represent the total downward forces acting on the pod:

W total=W(Aluminiumextrusion)+W(Maglev)+Top Suspension under breaking + W (chassis)

Upward magnetic lift the magnets produce a combination of upward and downward forces to keep the pod levitated and laterally/vertically stable. The upward magnetic force supports most of the pod's weight. The downward negative lift controls the pitch preventing the pod from rising too high.

If the maglev system does not carry 100% of the weight, then a portion of the load is still on the wheels. Wheel's Reaction Force each wheel contact at the front and rear of the suspension system exerts a normal reaction on the chassis.

F Actuator ensures dynamic response under breaking and smoothing out any shocks.

Under braking, the suspension assembly is pushed backward (due to friction) and downward (due to the normal force), transferring the load into the spring and damper. Together, the spring and damper ensure controlled vertical and longitudinal movement of the top wheel relative to the pod, smoothing out shocks while effectively transmitting braking loads. The magnetic force represents the pod's levitation system that normally supports most of its weight.

During breaking the wheel makes contact with the rail where the rail exerts a normal reaction force on the wheel. This contact generates friction opposing the motion of the pod (propulsion force). The friction is transmitted through the suspension system to the main chassis providing the breaking force slowing the pod. The magnetic force represents the pods levitation system.

The spring and damper ensure controlled vertical and longitudinal movement of the top wheel relative to the pod body, smoothing out any shocks while transmitting braking loads.

The spring is compressed or extended depending on the wheels relative position to the chassis working to restore equilibrium. The damper force resists the relative motion between the wheel and chassis. This

controlled resistance helps manage large dynamic loads that can occur during abrupt braking at high speeds.

Side suspension

Side suspension design is crucial for high-speed stability, ride comfort, and overall safety ensuring the pod maintains the correct alignment preventing any lateral drift.

The wheel supports the pod during emergency and maintenance and ensures that the pod is correctly aligned due to the horizontal normal force and the friction force. The I bean exerts a normal contact force where the wheel contacts the rail, providing sideway support to guide the pod.

Where the wheel contacts the rail the rail exerts a normal reaction force on the wheel. The friction force acts tangentially to the surface providing traction during breaking.

If the wheel moves up or down the dampener exerts a resistive force. Fdamper[Equation] (where c is damping coefficient, [Equation] is the relative velocity). Preventing abrupt motion.

Weight pointing into the page is the gravitational force acting on the assembly

The friction force acts tangentially to the surface. Opposes lateral motion between the wheel and the beam ensuring the pod dose not drift off of the track.

When the wheel assembly moves relative to the pod the dampener resits the motion providing a dampening force. Transmitted through the dampener to the bracket, controlling the lateral motion absorbing shock. Smoothing out vibrations

The triangular metal bracket connects the wheel axel to the dampener and the rest of the chassis ensuring the forces from the wheel and dampener and transferred correctly into the chassis.

Fd The dampening force providing the resistive force proportional to the relative speed of movement. Fc represents the contact force that is perpendicular to the rail surface. Ff is the friction force acts parallel to the contact surface helps ensure the pod dose not drift ensuring correct alignment.

14 Appendix 1: Aeroshell

14.1 Overview

The outer shell is designed as a lightweight, aerodynamic structure intended to optimize performance while providing a protective and aesthetically pleasing exterior. The smooth, streamlined contours are aimed at reducing air resistance, with the design carefully balancing form and function. Composite materials have been chosen to manufacture this design for their lightweight and durable properties, ensuring the shell can withstand external forces without compromising efficiency.

14.2 Specifications

14.3 Budget and Timeline

Item Description	**Cost (£)**
Outer Shell Tooling	1500
Outer Shell Machining	1000
Outer Shell Fabric	300
Outer Shell Core Material	200
Outer Shell Consumables	600

Table 34: Cost breakdown for Outer Shell

The outer shell team works under the umbrella of the chassis sub-team hence their timelines are combined together. Furtheremore, we have some sponsorships and in house facilities that eliminate costs like consumables.

15 CFD Simulations

15.1 CFD and how it works (1)

Computational fluid dynamics, otherwise known as CFD, uses computational methods to solve complicated fluid flow and fluid mechanics problems. This method of simulating flows is crucial in various engineering industries, such as automotive and aerospace, as it helps define the aerodynamic behaviour of various objects and vehicles.

Conservation of mass is one of the most important concepts in CFD. The latter ensures that the amount of fluid entering a volume is equal to the amount exiting. This principle ensures that the flow is consistent and that no part of it is lost. Another important concept is momentum conservation, which can be derived from Newton's second law of motion. This principle ensures that the change in momentum in a fluid equals the sum of all forces acting on it. Using this principle, the acceleration and deceleration of fluids are affected by various forces, like gravitational forces, pressure gradients, and friction. The CFD algorithm can predict the interaction between solid and fluid boundaries. The concept of energy conservation is another important one. This principle ensures that no energy is destroyed or created and is derived from the first law of thermodynamics. The principle states that energy can only

be converted from one form to another. In the realm of fluid dynamics, this is related to the conversion between various types of energy, such as potential, kinetic, and thermal energies. This concept is crucial in comprehending heat transfer problems and, hence, fluid flow problems.

The main governing fluid dynamics equations are called the Navier-Stokes equations. They are solved by discretizing the domain of the fluid into a mesh. The mesh uses smaller volumes that are continuous to discretize the domain; those volumes are called elements. The mesh, otherwise known as a grid, can be structured or unstructured. The structured mesh uses a regular pattern, whereas the unstructured ones use an irregular one. Some of the common discretizing methods are the finite volume method, the finite element method, and the finite difference method. The aforementioned methods find approximations of the fluid property values at discrete points. This allows for a numerical solution to the governing equations.

In many fluid dynamics problems, turbulence occurs. This is a chaotic and complex fluid phenomenon that occurs when velocities are high, resulting in Reynolds numbers above 3500 Re. It can be very challenging to correctly and accurately model turbulence. A variety of models exist that assist in solving fluid dynamics problems involving this phenomenon. Those include direct numerical solution (DNS), large eddy simulation (LES), and Reynolds averaged Navier-Stokes (RANS). The most accurate of those models is DNS, but it has significant computational requirements. RANS, however, provides a more practical solution that balances accuracy and computational cost. It involves averaging the volatile turbulence behaviour, hence why it is called RANS. The flow is decomposed into mean and fluctuating components. This decomposition ensures that the complex, time-dependent turbulent flows have a more manageable form, with averaged effects over time. The equations that come from this account for the mean flow add new terms that are referred to as Reynolds stresses. Those terms represent the turbulent fluctuations over time. Those stresses need to be modelled for the RANS model. Turbulence models like k-omega SST can help us with that.

K-omega is the most widespread model for turbulence in RANS. It uses two transport equations. The first equation accounts for turbulent kinetic energy, k, and the second one accounts for the turbulent dissipation rate. The model assumes that the turbulence is isotropic, which implies that its properties are the same in every direction.

To correctly and accurately model turbulence using this model, the walls next to boundary layers need to be treated specifically; this involves particular mesh refinement. The dimensionless wall distance (y+) from the wall to the first computational cell centre is employed to ensure that the treatment of the mesh near the wall is correct. The fluid layer closest to the wall is referred to as the viscous sub-layer. For it to be very accurately resolved, the y+ value must be at least one. Such a y+ value will ensure that the mesh's first layer is in the viscous sub-layer. Higher values of y+ would mean that the first layer would be in the buffer or logarithmic layers, which could provide less accurate solutions. The calculation of the y+ value is the friction velocity times distance from the wall to the first cell center times density over the kinematic viscosity.

In CFD, an important factor that must be monitored is the continuity residual. This represents the imbalance in mass conservation throughout the entire computational domain. The residuals gauge how

well the solver's numerically produced solution satisfies the governing equations. For residual convergence to occur, the value of the residuals must drop, which shows that the solution is approaching equilibrium. The continuity residual is crucial to monitor, as its value needs to be very low. For the purposes of this dissertation, a value of ten to the power of minus one is adequate. Such a low residual in continuity ensures that the mass has converged over the entire domain.

To perform CFD simulations, the correct boundary conditions need to be applied. They ensure that the fluid and solid interactions are correct. Among these boundary conditions are the specification of inlet and outlet velocities or pressures, the definition of solid walls, the absence of slip conditions, and the presence of moving walls. The symmetric boundary condition is extremely useful. This condition uses the symmetry of the model and allows for only half of it to be solved. For it to be accurate, the real-life flow on the other side of the symmetry plane must be completely similar to the flow that is simulated. In terms of fluid flow, this condition is valid when the velocity components perpendicular to the plane are zero.

15.2 CFD Simulations Methodology

The following text outlines the methodology used for the CFD simulations performed on the outer shell.

Ansys Fluent was chosen to simulate aerodynamic behaviour due to its robustness, reliability, and fast amount of instructions on its use. The solver provides a multitude of turbulence models, such as the K-omega SST model that was used in this report. The software also allows for parallel processing and four computer cores. The software, however, comes with one important drawback: its limitation on the number of elements with the student license, which was used in this report. The limit imposes that no more than roughly 1 million elements can be used. It is important to note that the simulations were heavily simplified in order to save computational power and fit within the element limit. This is why the pod was simulated to be glued to the ground. Furthermore, most simulations were run on non-moving ground. This does not represent the aerodynamics of the pod correctly, as an additional boundary layer is formed on the ground. However, this simplification allowed for a validation study to be performed using the wind tunnels provided by the university, which do not have the resources to represent a moving floor. The CFD results can then be compared to the wind tunnel data to assess their accuracy. Using the validated CFD methodology, other simulations were performed using a moving floor; however, they were only partially validated due to the wind tunnel testing the static floor. The simulations described below simulate the scaled outer shell to allow for comparison with the wind tunnel data. The approach used is employed for a scaled-up shell. More will be explained in the paragraphs and sections below.

The first step in the simulation procedure is to set up the geometries and bounding boxes. The center of the shell's base is the frame of reference for the coordinate system's origin. The distance from the inlet to the origin was 600 mm, whereas the distance between the origin and outlet was 400 mm. The geometry of the shell was cut in half along the length of the shell. The width and height of the bounding box are 100 mm and 150 mm, respectively. The refinement box used had a length of 125 mm upstream starting from the origin and 150 mm downstream starting from the origin. The width and height of it were set to 50 mm. The bounding and refinement boxes can be seen in figure **??**. It is important to note

that for highly accurate simulations, the size of the boxes might be too small; however, due to the harsh element limit imposed, the previously defined dimensions were chosen as they allowed for a bigger mesh density, which could help with improving the accuracy of the simulations close to the boundary layers.

During the meshing stage of the simulation, a hybrid mesh was utilised. Tetrahedral elements were used in the fluid domain, hexahedral in the boundary layer, pyramid elements for transitioning, and prism ones for inflation layers. Using a y+ value of 1, the first layer thickness was calculated to be 0.023 mm at a velocity of 15 m/s and a length of 20 cm. There were 15 years used for the inflation layer to simulate it. To ensure the quality of the mesh was sufficient, the following mesh metrics were used: skewness less than 0.95, orthogonal quality above 0.1, aspect ratio ideally less than 10 for tetrahedral elements, and element quality close to 1. Named selections were then created on the mesh with the following names: inlet, outlet, symmetry plane, ground, and shell surface (14).

The chosen boundary conditions included an inlet velocity of 15 m/s, an atmospheric pressure outlet, a symmetry condition across the pod's symmetry, a stationary no-slip floor, and moving walls. The moving walls prevent the formation of boundary layers in unwanted regions, but they still pose limitations as they create a blockage. The density of air used was 1.225 kg/m^3. The turbulence model k omega SST was chosen. A turbulent length of 2 cm was used, as it is 0.1 times the length of the body (14). The initial relaxation factors used were the following: pressure 0.5, momentum 0.5, density 1, body forces 1, turbulent kinetic energy 1, specific dissipation rate 0.75, and turbulent viscosity 1. Those are the default relaxation factors, and they were altered when necessary to get better and faster residual convergence.

To start the simulation, it was initially initialised using hybrid initialisation, which provides a balanced starting point. The solution was first solved using a first-order solution. The first-order solution's level of accuracy is unacceptable, but it improved the initial guess. Next, a more accurate second-order solution was performed. If these conditions were met, the solution was said to have converged: continuity of 10^{-4}, momentum of 10^{-3}, turbulent kinetic energy of 10^{-3}, and a specific dissipation rate of 10^{-3}. Those convergence criteria ensure a sufficient level of accuracy, as they ensure that, numerically, the solution has converged well. Lower residuals can be required for other purposes that require high precision and accuracy; however, for the purpose of this report, the aforementioned values suffice (**?**). It is important to note that lower residual convergence values would result in more iterations being required, and hence the simulation would take longer to simulate. As mentioned before, the relaxation factors were adjusted to help the simulation converge.

Then, a mesh convergence study was performed, which checked if the solution was mesh-independent. Drag and lift values and coefficients were monitored to assess mesh convergence. Every refinement in the mesh convergence iteratively increased the meshes' size by a factor of about 2. This was done to ensure that each mesh increase is significant enough to have an effect on the mesh convergence (14).

The results from the simulations were then extracted in the form of lift and drag forces as well as velocity and pressure contours. Another form of data that was extracted were the velocity profiles at targeted locations (the middle of the pod and the front tip of the pod) along a line.

16 CFD mesh convergence study

During the CFD mesh convergence study, 3 iterations of the mesh were made. The size of the various meshes can be seen in table 35. The values of lift, drag, coefficient of lift, and coefficient of drag for the moving floor and not moving floor can be seen in tables 36 and 37.

Table 35: Mesh parameters for different iterations

Mesh iteration	Elements (#)	Element size (mm)	Refinement box size (mm)	Floor size (mm)	Shell size (mm)
1	312593	15.000	10.000	10.000	10.000
2	582525	15.000	4.000	4.000	4.000
3	1043182	15.000	2.350	4.000	1.200

Table 36: Mesh iteration results for static floor setting

Mesh iteration	Cd	D (N)	Cl	L (N)
1	0.094	0.023	0.010	0.079
2	0.104	0.087	0.011	0.093
3	0.110	0.103	0.121	0.114

Table 37: Mesh iteration results for moving floor setting

Mesh iteration	Cd	D (N)	Cl	L (N)
1	0.099	0.135	0.119	0.128
2	0.123	0.116	0.108	0.119
3	0.129	0.142	0.119	0.131

From the results, it can be seen that the meshes do not converge well, as the final difference in the values between iterations 2 and 3 is roughly 10% for almost all the values. This level of change suggests that mesh convergence has not been reached. The values of drag and lift were chosen as they are very representative of the flow.

Further mesh convergence cannot be done due to the element limitations, but it is required to achieve accurate simulations. The third mesh can be seen in figure 117. The velocity and pressure contours at the symmetry plane can be seen in figures 118 and 119.

The pressure contour suggests that stagnation pressure occurs at the front of the pod. The velocity contours clearly show a wake aft of the shell. More will be commented on the contours in the wind tunnel comparison section.

16.1 Wind tunnel testing

16.1.1 Particle Image Velocimetry (PIV)

Particle image velocimetry (PIV) is an optical flow diagnostic tool that can examine flow fields without creating flow disturbances. The technique works by seeding the flow with particles referred to as tracer particles. When illuminated, the particles can scatter light, allowing for flow visualization. The light source can come from a thin plane of laser light, otherwise known as a laser sheet (15).

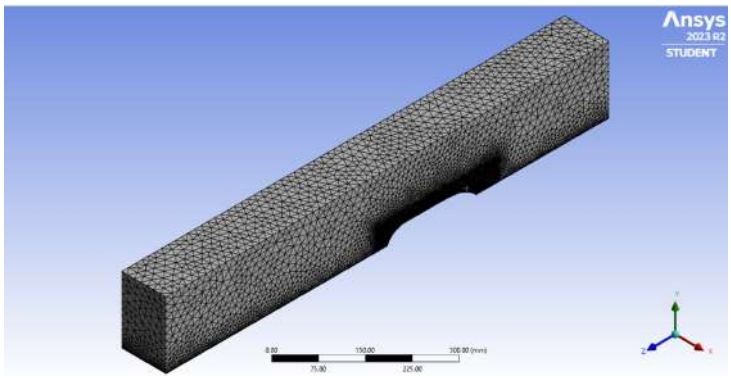

Figure 117: Photo of mesh in iteration 3

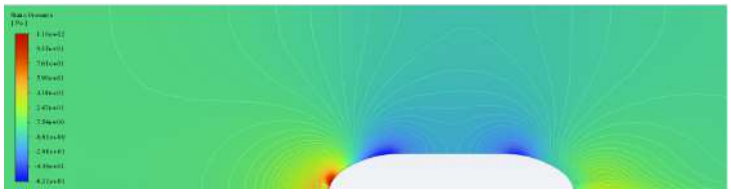

Figure 118: Pressure contours for mesh iteration 3

Common PIV testing systems have five systems that are integral to the testing procedure. These systems include a seeding system, an imaging system that uses high-resolution cameras, and a synchronization system that coordinates the laser pulses and the camera's exposure (**?**).

The seeding particles added to the fluid must have properties consistent with the airflow's dynamics. Some of the available seeding materials include aluminium flakes, hollow glass spheres (typically used in airflow with a high Mach number), soap bubbles, and oil bubbles for flows with a relatively low velocity. The camera tracks the location of the laser-illuminated particles (**?**).

To find the displacement of the particles, the camera tracks them in two photos, one after another, within a brief amount of time. This taking of a pair of photos is done many times over for a specific amount of time. Using two pairs of particle locations derived from the image, the displacement of the particles is found. When combined with the time interval between a set of image pairs, the velocity of the particles is calculated. The velocity of the particles is averaged using all the pairs of images taken. PIV testing can provide highly accurate velocity contours, which can be used to validate CFD data (**?**).

Therefore, to sum everything up, PIV provides a highly accurate and non-intrusive way to measure airflow characteristics. It is used in a variety of industries, including the aerospace industry and the automotive industry (**?**).

16.1.2 Wind tunnel testing methodology

The wind tunnel testing was done on a non-moving floor, as mentioned previously. This is a very different situation from a moving floor in regards to aerodynamics. This was done due to the limitations of the testing resources available. A test involving a moving floor would require a moving belt to simulate the moving ground and prevent the formation of a boundary layer on the ground.

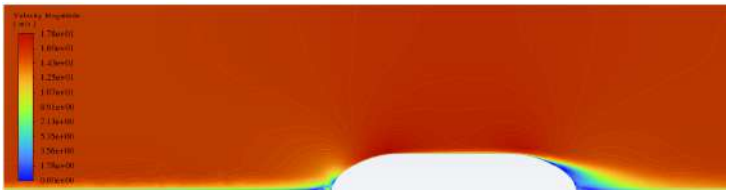

Figure 119: Velocity contours for mesh iteration 3

To perform the wind tunnel testing, the method outlined below has been used. First, the geometry of the shell was scaled down and 3D printed using an FDM printer. In the shell, there was a 0.125 scale factor reduction. This ensured that its length was 20 cm, which ensured that the PIV camera used was able to capture the flow around it. After that, the form was sanded using high-grit sandpaper to increase its smoothness. Special care was taken to ensure that the shape of the shell was not sanded too much as to change its aerodynamic behaviour.

Once the model was prepared, it was placed in a location in the wind tunnel that was painted black and was in the camera cross-section. Using a pointed leveler and ruler, the model was angled to directly face the flow, after which it was taped down using double-sided tape. The laser pointer was first straightened out, after which the shell was rotated to ensure both its front and back tips were on the laser line, as can be seen in figure 120.

This allowed for the next step to be carried out, which involved aligning the PIV laser to illuminate the required section of the shell, which in this case is its middle along the length. This was done using the appropriate safety gear (such as safety glasses) needed to operate high-power lasers. This part is critical to ensuring the correct part of the flow is illuminated. The laser used can be seen in figure 121.

Figure 120: Procedure for setting correct outer shell angle

The next step in the procedure involved introducing particles into the air that the laser sheet would illuminate. The seeding particles are introduced at the inlet of the tunnel and diffused through the use of smoke generators. After the seeding is started, the free stream velocity in the tunnel must be set to exactly 15 m/s. This velocity was chosen because it was the highest speed that the wind tunnel could

Figure 121: PIV laser

reach. It is important that sufficient time be provided for the flow in the tunnel to stabilise and develop.

The next part of the experiment involves the PIV measurements. The camera needs to be synchronised to capture multiple image pairs to obtain velocity fields that statistically converge. Furthermore, the time between laser pulses must be adjusted based on the flow velocity and the expected particle displacement (**?**).

The next and final step of the experiment involves data processing of the results. This entails locating the different particles in each image pair and creating vector maps from them. All the vector maps for all the pairs are averaged to give the final results. The software that processes the results is able to locate the individual particles and track their new location change between each image pair. The test's final output is a contour map of the tested object, which in this case is the hyperloop shell.

The velocity contours for the wind tunnel test can be seen in figure 122.

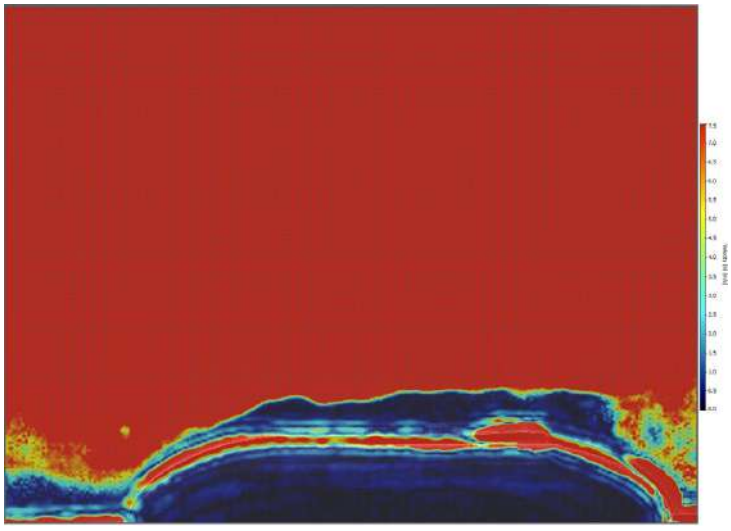

Figure 122: Wind tunnel vector plots

16.2 Aerodynamic Results Analysis and Comparison

In summary, although the CFD solution is not mesh-independent, its velocity contour has similarities to the wind tunnel contour in terms of the shape of the wake. It is important to note that the dark spots on the wind tunnel contour represent areas with zero air velocity. However, as a result of the outer shell's surface reflecting the laser beam, more dark spots appeared close to the surface. It is important to note that this does not necessarily mean that the air velocity is zero.

A more detailed comparison was made using the velocity profiles at two specific locations: the front tip and the middle of the pod. The contours shown do not account for a moving floor due to the wind tunnel's inability to provide a moving floor.

When inspecting the contours, it was noticed that the growth rate of the boundary layer is very rapid in the CFD compared to the wind tunnel data. This suggests that the mesh needs to be more refined close to the boundary layer. Hence, the mesh convergence results and the wind tunnel data show that the simulations could significantly benefit from an increase in the mesh size, particularly close to the boundary layers. It is important to note that the simulation procedure taken has not been disproved, and hence the method used for the CFD is not necessarily wrong but just suffers from a lack of elements.

The final simulation case to show is one of the moving floor; its velocity contour can be seen in Figure 125. Similarly to the case with the static floor, it has not reached mesh convergence, as shown in the table in the upper pages. However, the mesh has converged better, which can be explained by the lack of a boundary layer that needs to be resolved at the ground. A scaled-up version of the CFD simulations was not performed as mesh convergence was not reached, and hence future simulations would also be limited by the mesh size and would be inaccurate.

Overall, the aerodynamic analysis performed has produced some results with limited accuracy due to the constraint on the mesh size. Some similarities exist between the test and simulations; however, they are limited, and hence the aerodynamic behavior has not been predicted accurately. There were initial plans in the scope to simulate the deflection of the outer shell structure using the pressure distribution on it. However, this was removed from the scope due to the inaccuracy of the CFD and hence the potential boundary conditions for the shell deflection simulations.

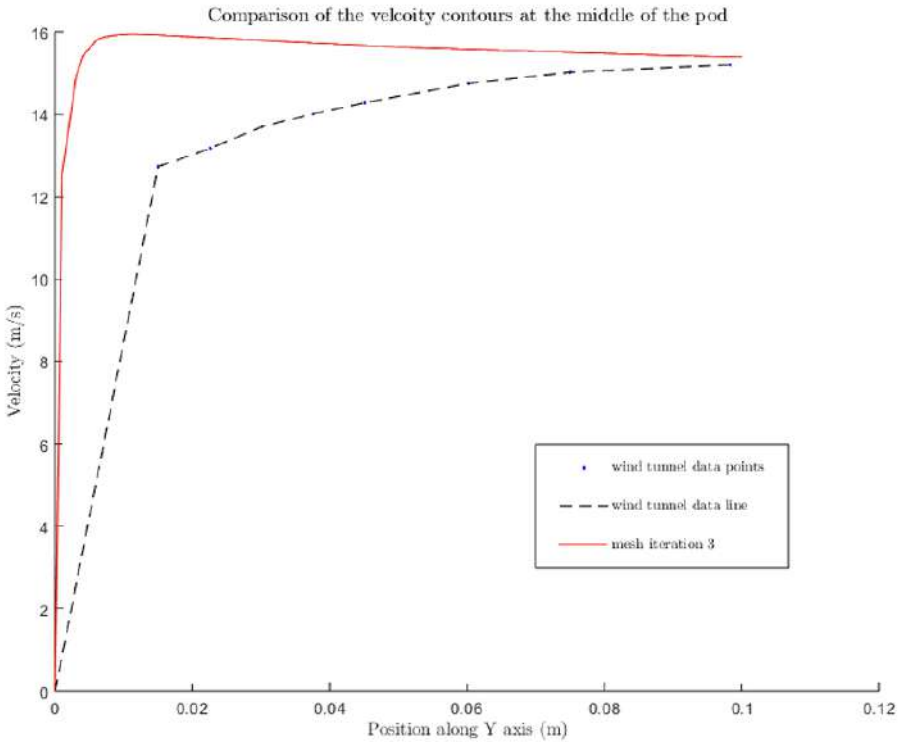

Figure 123: Comparison of the velocity contours at the middle of the pod

16.3 Braking Manufacturing

16.4 Chassis Manufacturing

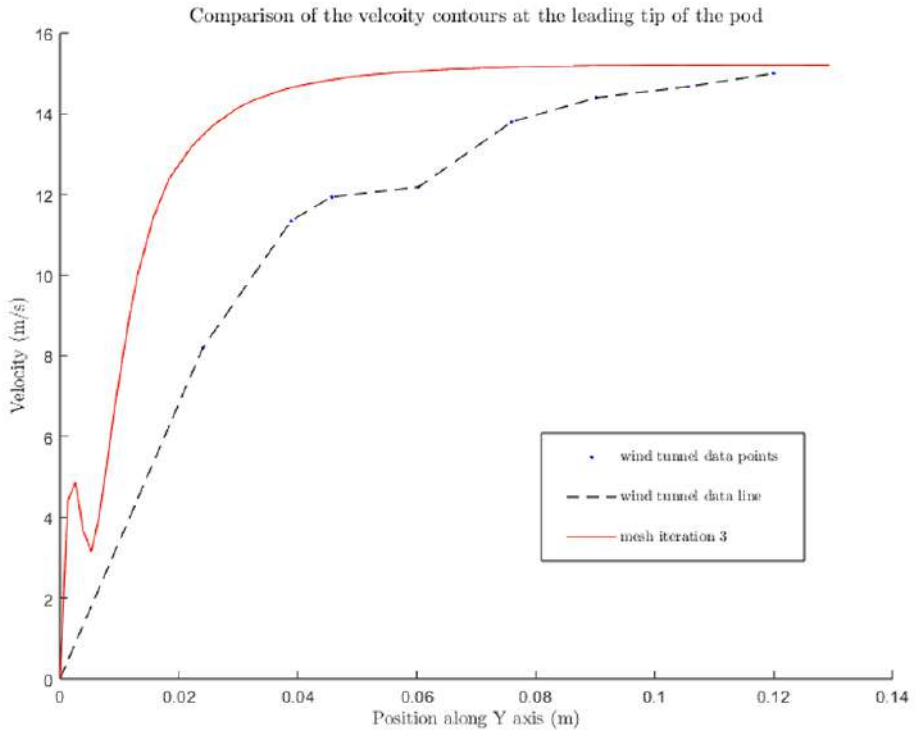

Figure 124: Comparison of the velocity contours at the front of the pod

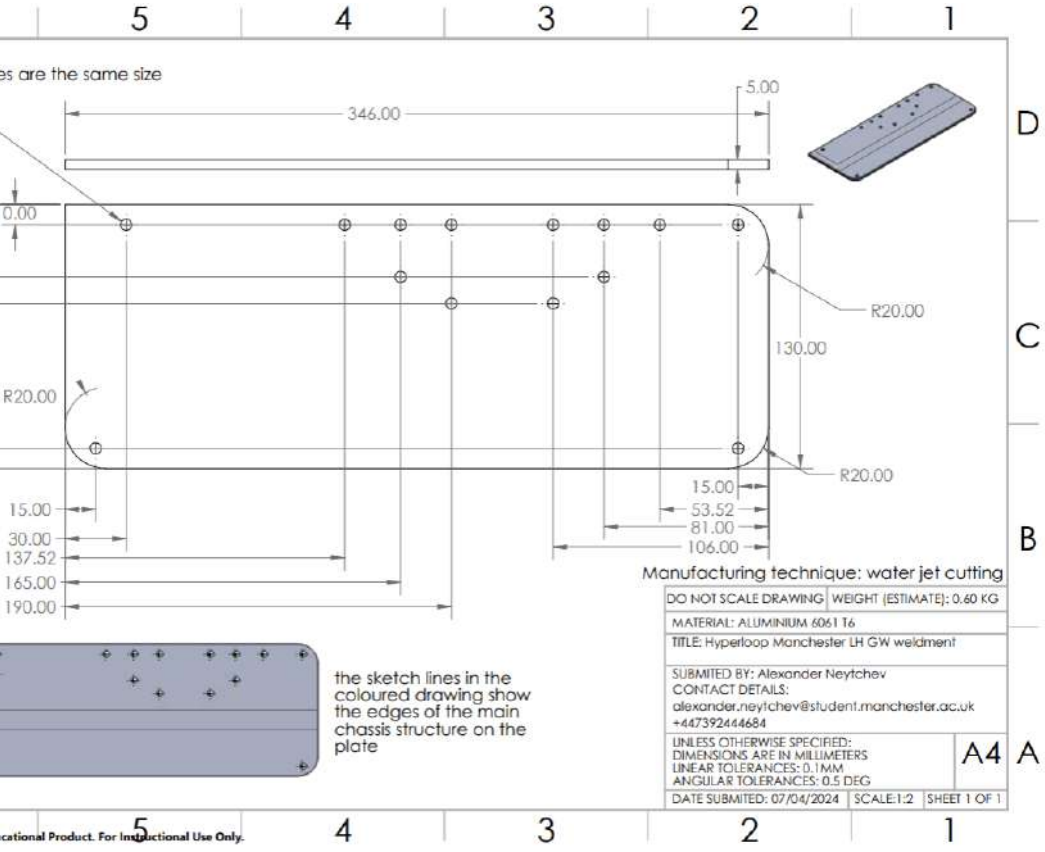

Figure 177: LH GW Weldment

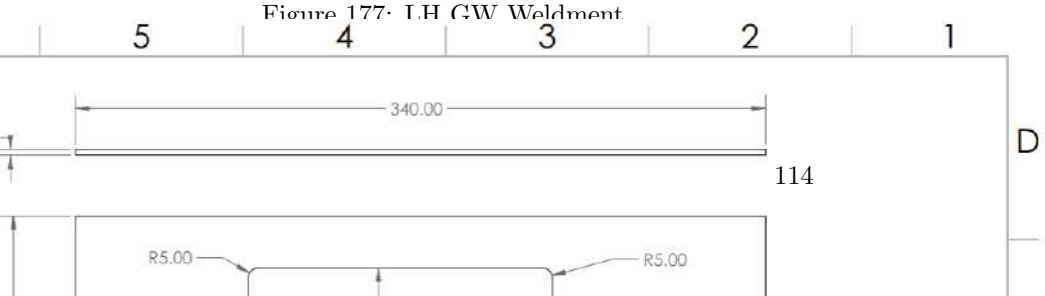

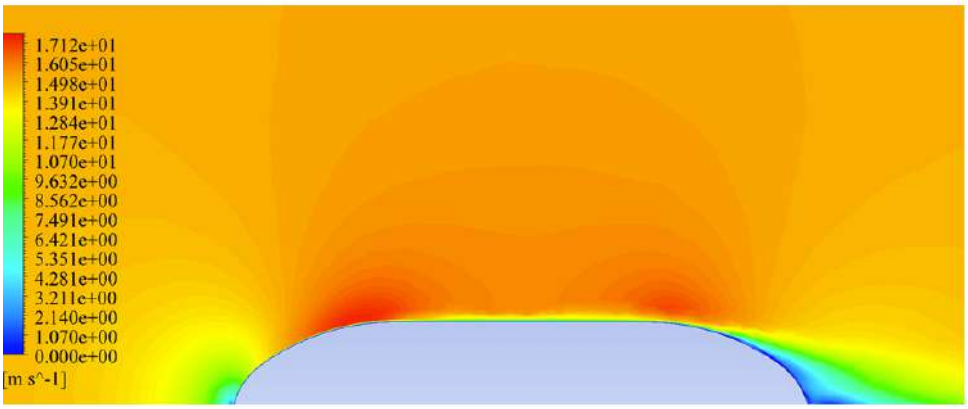

Figure 125: CFD with moving floor

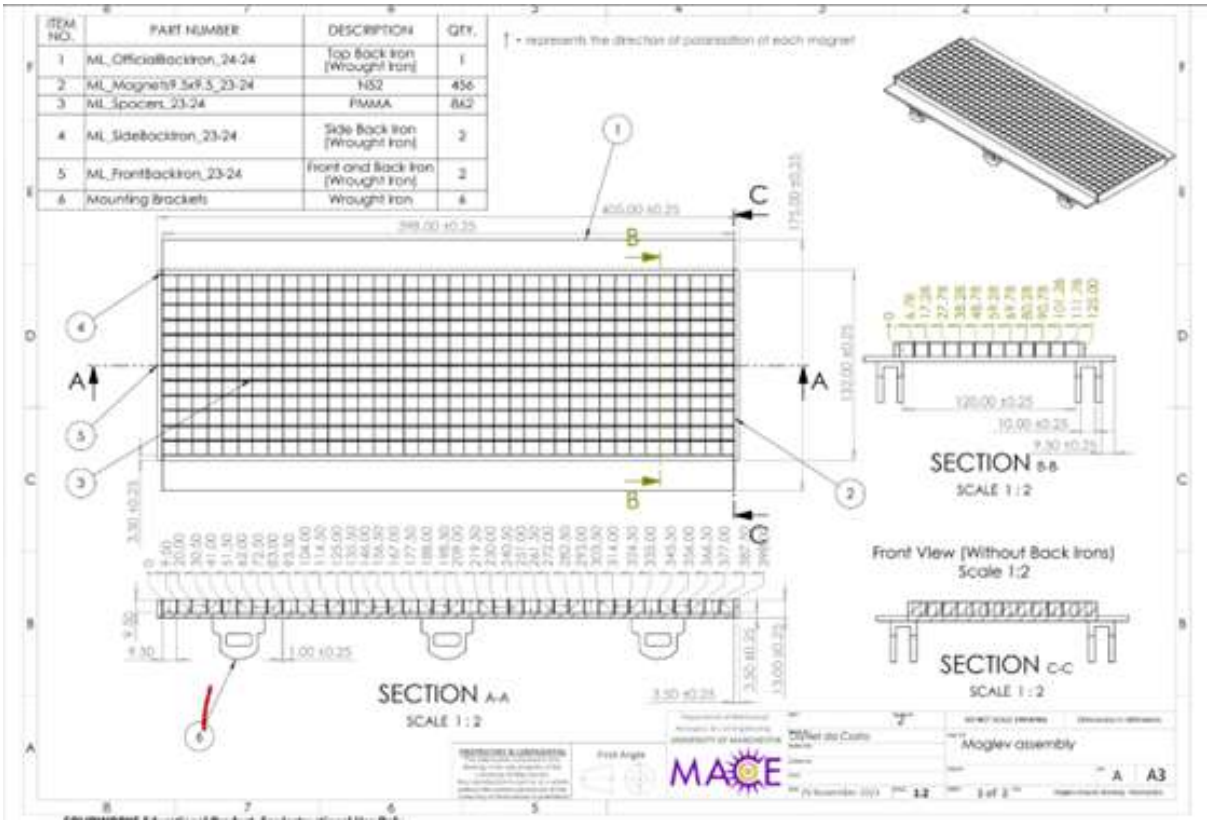

Figure 126: SolidWorks Drawing of Halbach array skis, with polarisation and mounting clevis brackets indicated.

Issue date: 26-4-2023

Technical Datasheet: Neodymium N52 – Anisotropic Sintered

Demagnetisation Curve N52

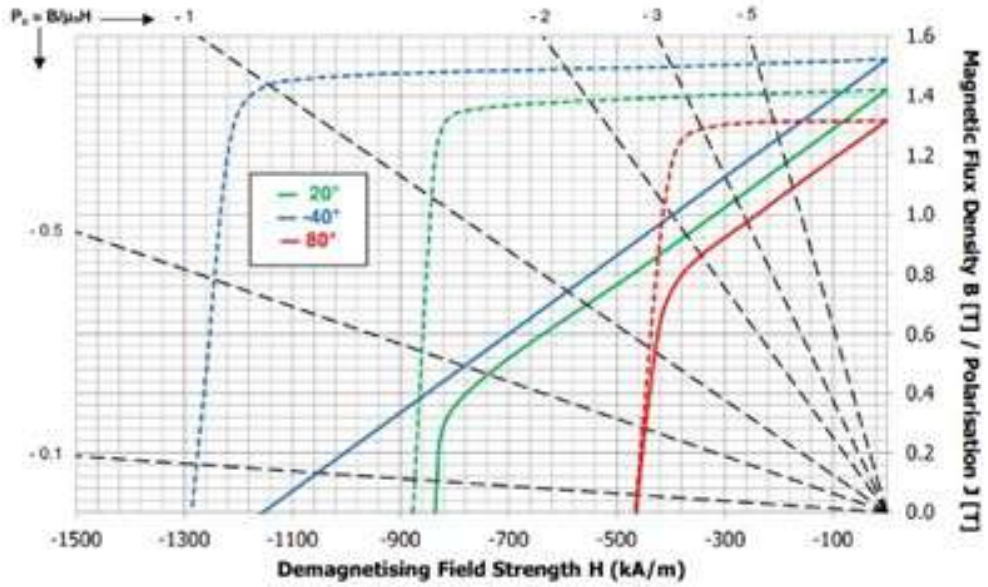

Solid lines represent magnetic flux densities. Dashed lines represent polarisations. The curves here are estimates obtained from data available from the current Goudsmit grade system (Available on the website. See also the magnetic properties below). On request, actual measurements of demagnetisation curves can be obtained. For that, contact us on the address below.

Magnetic Properties @20°C			
B_r	min	1.42	T
H_{cB}	min	836	kA/m
H_{cJ}	min	876	kA/m
$(BH)_{max}$	min	390	kJ/m³
$\alpha(B_r)$	min typ	-0.12	%/°C
$\beta(H_{cJ})$	min typ	-0.78	%/°C
T_{max}		80	°C
μ_r	typ	1.05	-

Physical & Mechanical Properties @20°C			
Density	typ	7400 - 7800	kg/m³
Vickers Hardness	typ	500 - 700	HV
Modulus of Elasticity / Young's modulus	typ	140 - 200	GPa
Flexural / bending strength	typ	100 - 400	MPa
Compressive strength	typ	600 - 1100	MPa
Tensile strength / ultimate strength	typ	74 - 90	MPa
Electrical resistivity	typ	1.1 - 1.7	μΩm
Specific heat capacity	typ	350 - 550	J/(kg K)
Thermal conductivity	typ	5 - 15	W/(m K)
Coefficient of linear thermal expansion, ∥ DOM*	typ	3 - 9	10^{-6}/K
Coefficient of linear thermal expansion, ⊥ DOM*	typ	-3 - 0	10^{-6}/K

* DOM = Direction Of Magnetisation

Figure 127: Data Sheet for magnets of the chosen system.

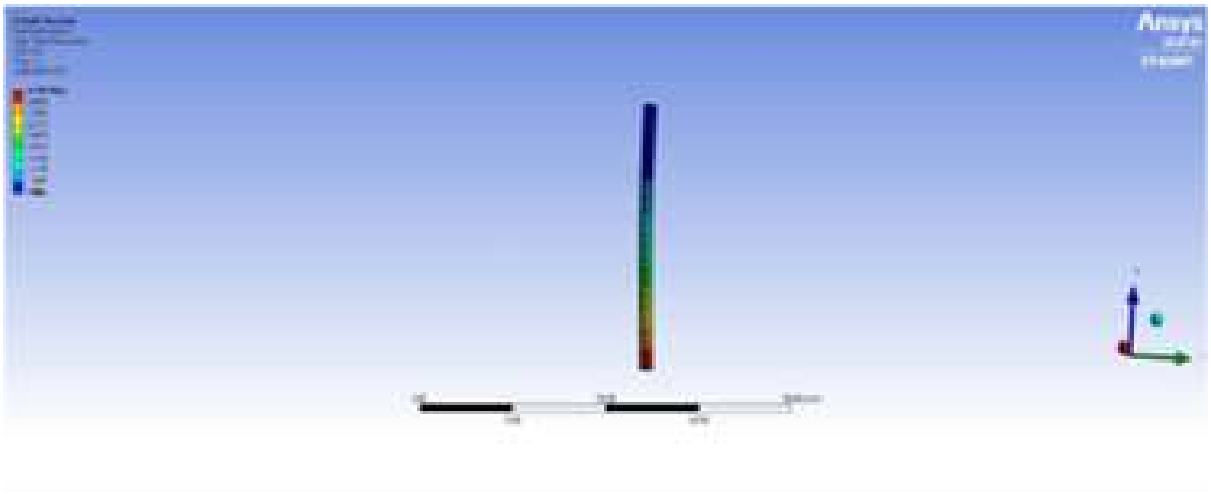

Figure 128: FEA for the braking rod.

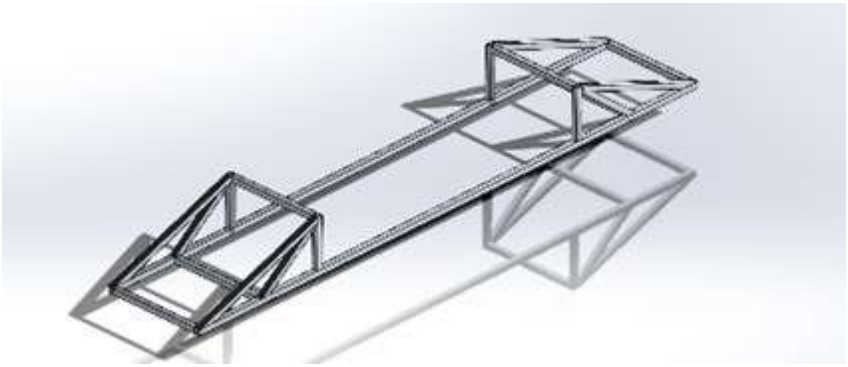

Figure 129: Chassis Shell structure.

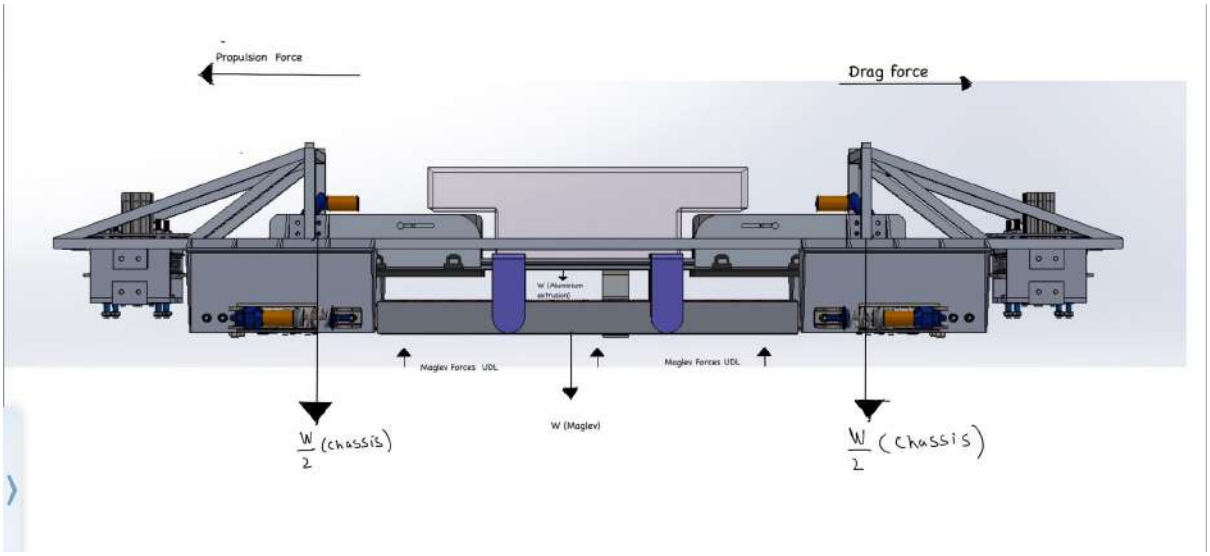

Figure 130: Side facing FBD for chassis system.

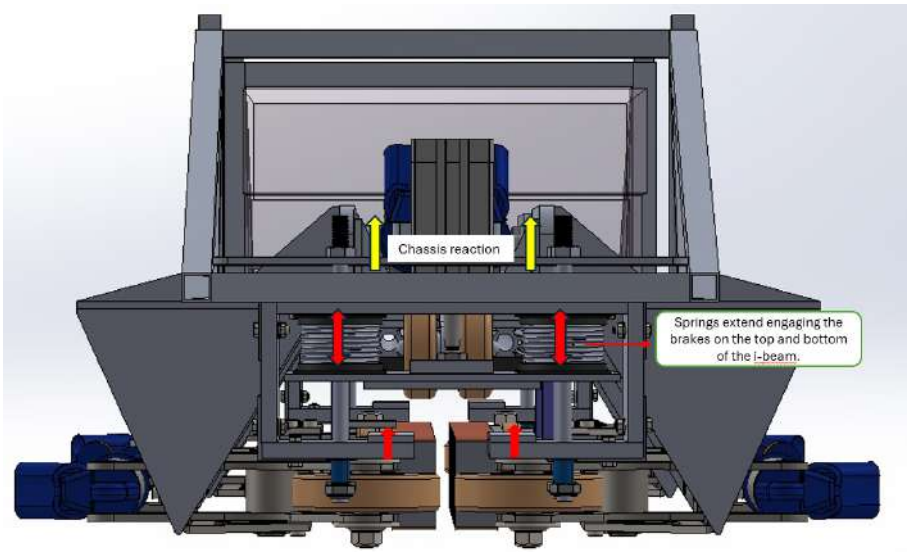

Figure 131: Front facing FBD for chassis system during braking.

$$F_L = \frac{\mu\sigma^2 slB_r^2M^2\sin^2\frac{\pi}{M}\left(1-e^{-kd}\right)^2\left(1-e^{-2ah}\right)}{\pi^2k^2}\frac{v^2}{\left(\sqrt{1+\frac{\mu^2\sigma^2v^2}{k^2}}+1\right)^{\frac{3}{2}}\left(\left(\sqrt{1+\frac{\mu^2\sigma^2v^2}{k^2}}+1\right)^{\frac{1}{2}}+\sqrt{2}\right)}e^{-2ky_1}$$

$$\approx \frac{\mathrm{sl}\,B_r^2M^2\sin^2\frac{\pi}{M}\left(1-e^{-kd}\right)^2\left(1-e^{-2ah}\right)}{\mu\pi^2}e^{-2ky_1} \tag{1}$$

$$F_D = \frac{\sqrt{2}\sigma slB_r^2M^2\sin^2\frac{\pi}{M}\left(1-e^{-kd}\right)^2\left(1-e^{-2ah}\right)\left(1+e^{-2ah}\right)}{k\pi^2}$$
$$\times\frac{v^2}{\left(\sqrt{1+\frac{\mu^2\sigma^2v^2}{k^2}}+1\right)\left(\left(\sqrt{1+\frac{\mu^2\sigma^2v^2}{k^2}}+1\right)^{\frac{1}{2}}+\sqrt{2}\right)}e^{-2ky_1}$$
$$\approx \frac{\sqrt{2}slB_r^2M^2k^{\frac{1}{2}}\sin^2\frac{\pi}{M}\left(1-e^{-kd}\right)^2\left(1-e^{-2ah}\right)\left(1+e^{-2ah}\right)}{\pi^2\mu^{\frac{3}{2}}\sigma^{\frac{1}{2}}v^{\frac{1}{2}}}e^{-2ky_1}.$$

Figure 132: Magnetic levitation equations.

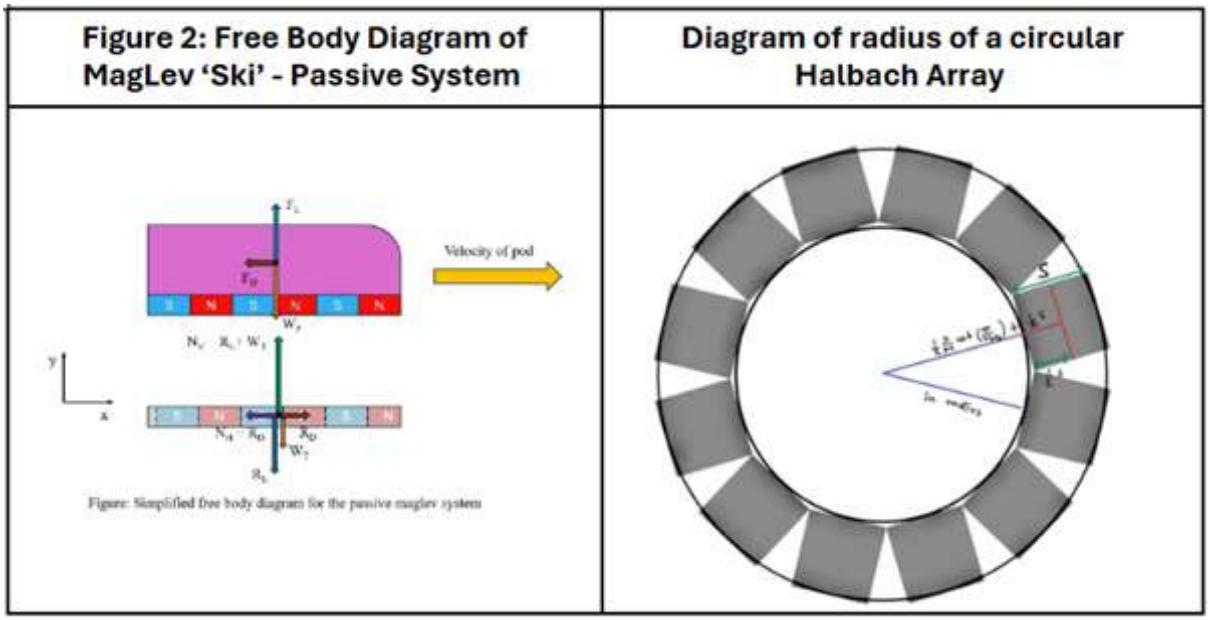

Figure 133: Halbach Array arrangement.

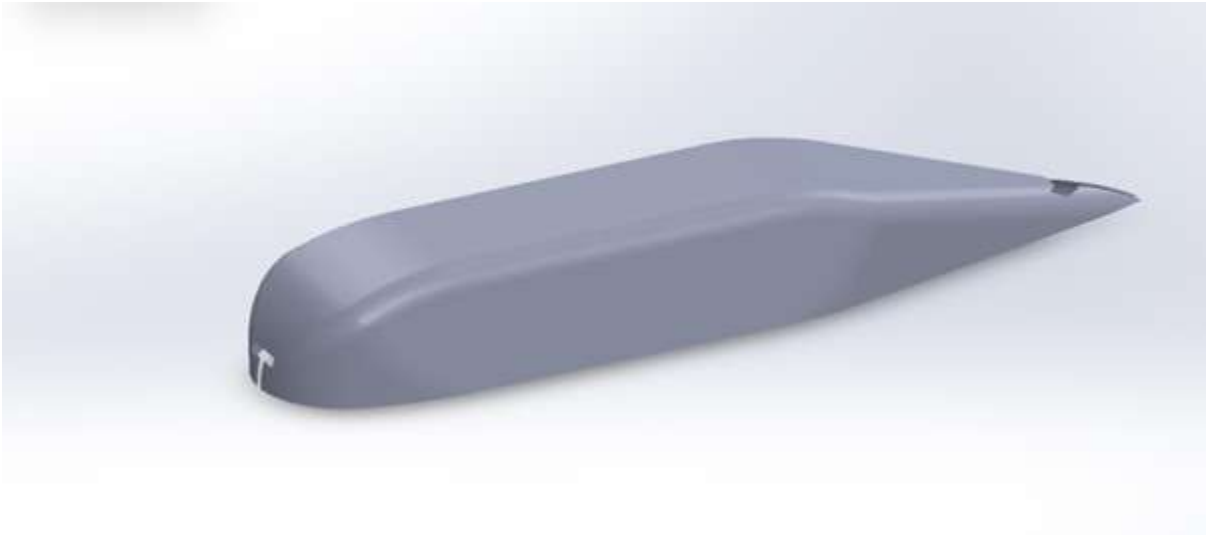

Figure 134: Outerhell Design.

Physical Properties	Metric	English	Comments
Density	0.0320 g/cc	0.00116 lb/in³	DIN 53420, ISO 845, ASTM D 1622
Mechanical Properties	**Metric**	**English**	**Comments**
Tensile Strength at Break	1.00 MPa	145 psi	DIN 53455, ISO 527-2, ASTM D 638
Elongation at Break	3.50%	3.50%	DIN 53455, ISO 527-2, ASTM D 638
Modulus of Elasticity	0.0360 GPa	5.22 ksi	ISO 527-2, ASTM D 638
Flexural Strength	0.800 MPa	116 psi	DIN 53423, ISO 1209, ASTM D 790
Compressive Strength	0.400 MPa	58.0 psi	DIN 53421, ISO 844, ASTM D 1621
Poissons Ratio	0.38	0.38	Calculated
Shear Modulus	0.0130 GPa	1.89 ksi	DIN 53294, ASTM C 273
Shear Strength	0.400 MPa	58.0 psi	DIN 53294, ASTM C 273
Thermal Properties	**Metric**	**English**	**Comments**
CTE, linear	50.3 µm/m-°C	27.9 µin/in-°F	
Maximum Service Temperature, Air	180 °C	356 °F	Heat Distortion Resistance; DIN 53424

Figure 135: Rohacell Datasheet for Aeroshell

Module	Battery voltage (V)			Battery capacity (A)		Fast charge current (A)	Discharge current (A)*1	Initial internal impedance ($m\Omega$)*2	Internal fuse rating (A)
	Min.	Typ.	Max.	Ah	Wh	Max.	Max.	Typ.	Typ.
Li1x1pVTC6	2.5	3.6	4.2	3	10.8	5	30	16.2	45
Li1x2pVTC6				6	21.6	10	60	8.0	90
Li1x3pVTC6				9	32.4	15	90	5.3	135
Li1x4pVTC6				12	43.2	20	120	4.0	180
Li1x5pVTC6				15	54	25	150	3.2	225
Li1x6pVTC6				18	64.8	30	180	2.8	270
Li1x7pVTC6				21	75.6	35	210	2.4	315
Li1x8pVTC6				24	86.4	40	240	2.2	360
Li1x9pVTC6				27	97.2	45	270	2.0	405
Li1x10pVTC6				30	108	50	300	1.8	450
Li2x1pVTC6				6	21.6	10	60	7.7	90
Li2x2pVTC6				12	43.6	20	120	4.0	180
Li2x3pVTC6				18	64.8	30	180	2.8	270
Li2x4pVTC6				24	86.4	40	240	2.1	360
Li2x5pVTC6				30	108	50	300	1.7	450
Li2x6pVTC6				36	129.6	60	360	1.4	540
Li2x7pVTC6				42	151.2	70	420	1.3	630
Li2x8pVTC6				48	172.8	80	480	1.1	720
Li2x9pVTC6				54	194.4	90	540	1.0	810
Li2x10pVTC6				60	216	100	600	1.0	900

Figure 136: Battery Properties.

ONLINE CATALOG > COILOVER SPRINGS > COILOVERS

18FS300 - 1.45 Inch ID, 4.4 Inch Length Coilover Springs

4.4 Inch long, 1.45 Inch ID, coilover spring with a rate of 300 Inch Pounds that allows for 2.583 Inch of travel.

Brand	**Hyperco**
Color	**Blue**
Deflection	**65.61 mm**
Free Length	**111.76 mm**
Inside Diameter	**36.83 mm**
Load	**351.47 kg**
Outside Diameter	**53.21 mm**
Rate	**52.53 N-mm**
SKU	**18FS300**
Series	**FS**
Solid Height	**46.15 mm**

Figure 137: Spring Properties.

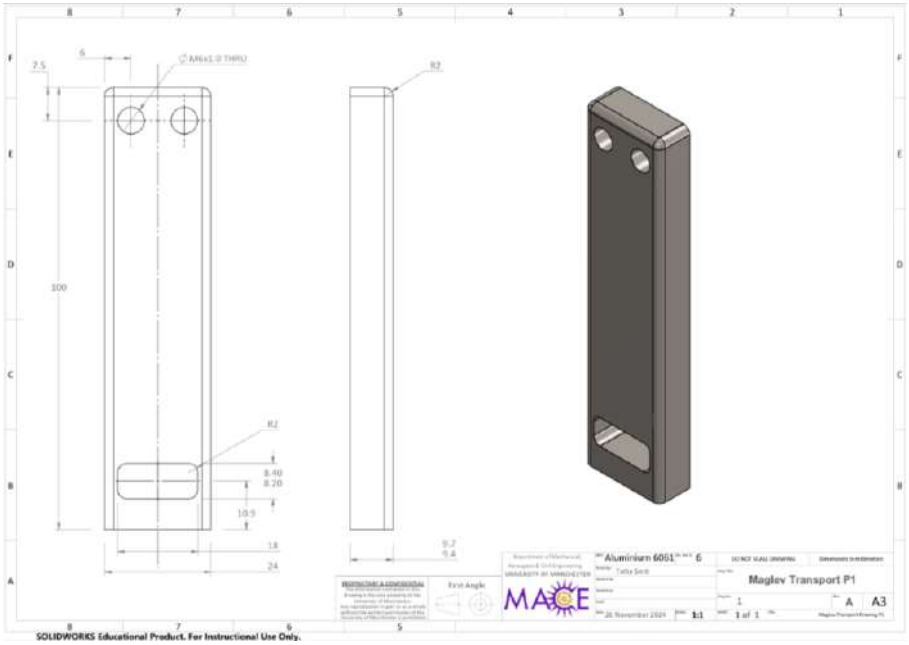

Figure 138: Drawing of transport bar.

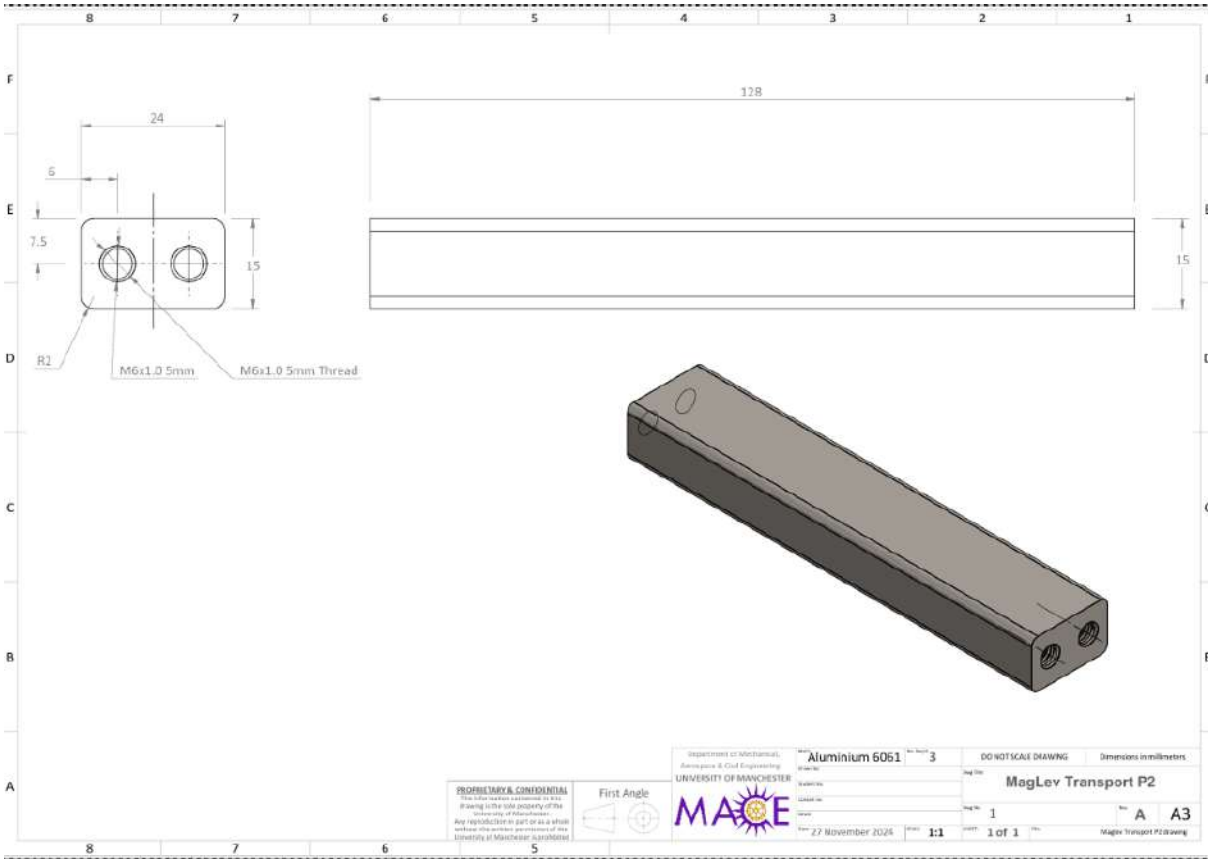

Figure 139: Maglev drawing for rod.

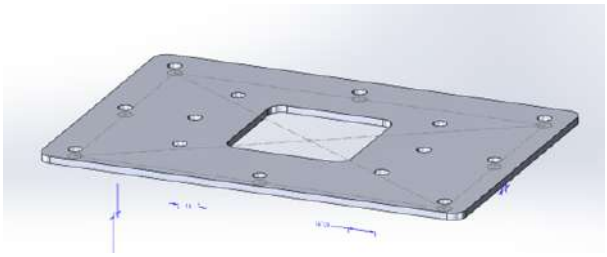

Figure 140: Braking Attachment Plate

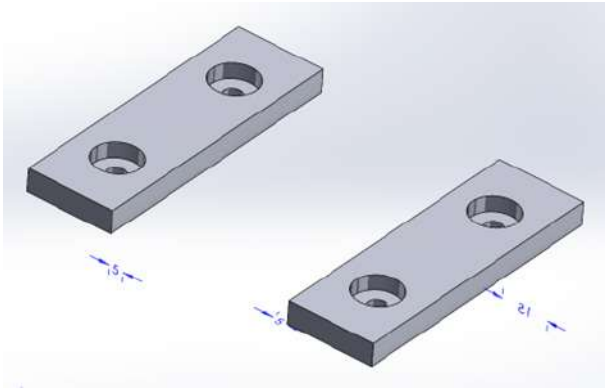

Figure 141: Bottom Brake Pad

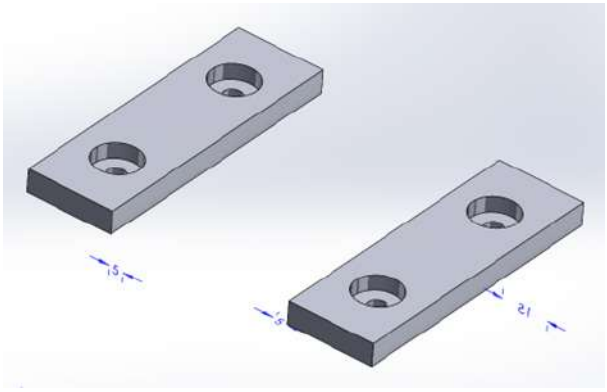

Figure 142: Bottom Brake Pad

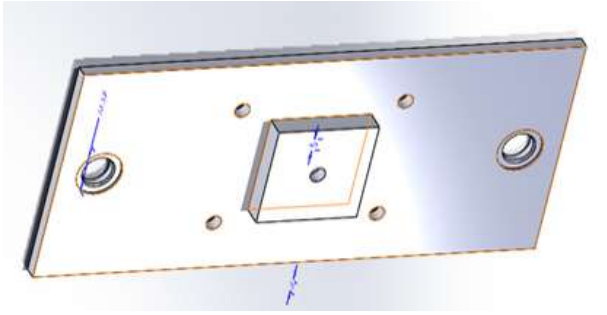

Figure 143: Brake Pad Holder.

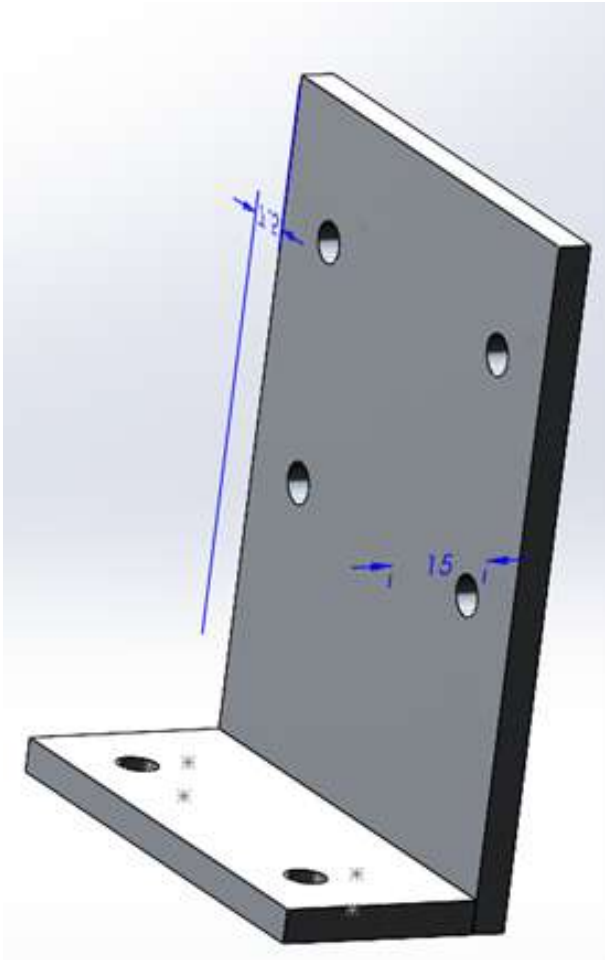

Figure 144: L Bracket.

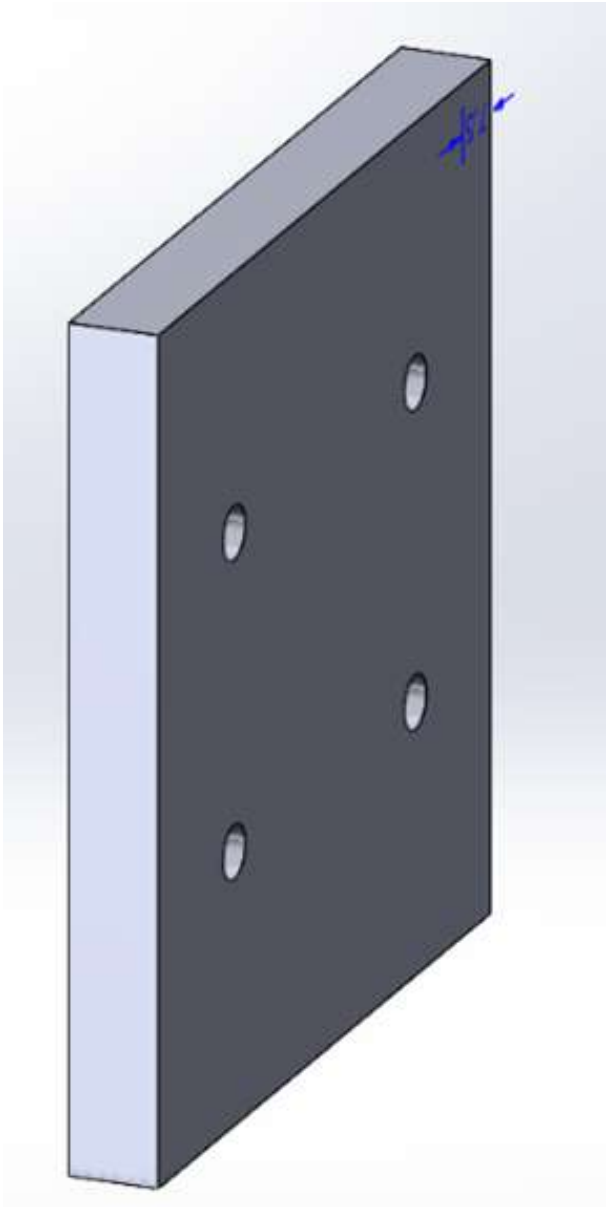

Figure 145: Side Plate

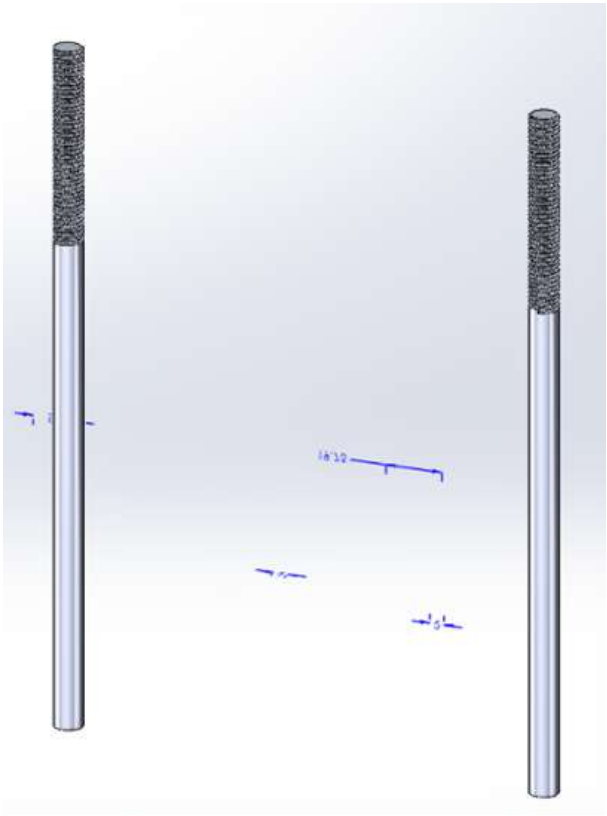

Figure 146: Rails

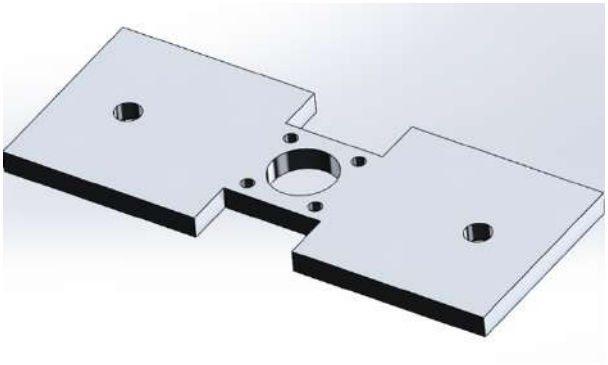

Figure 147: Top Plate

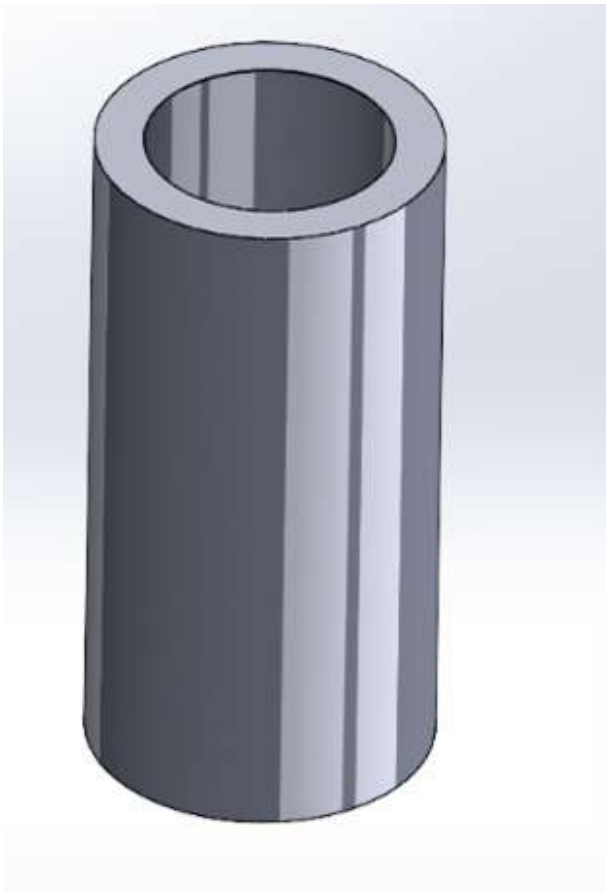

Figure 148: Connecting Rod

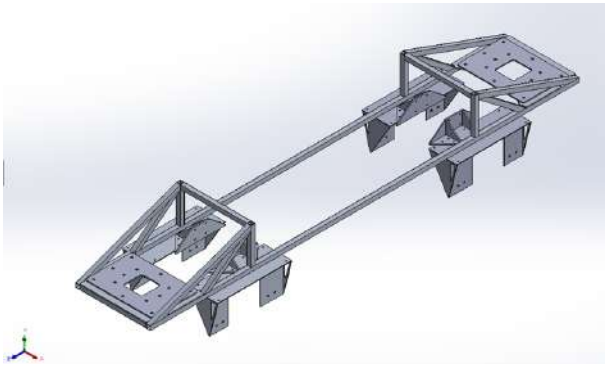

Figure 149: Chassis Assembly

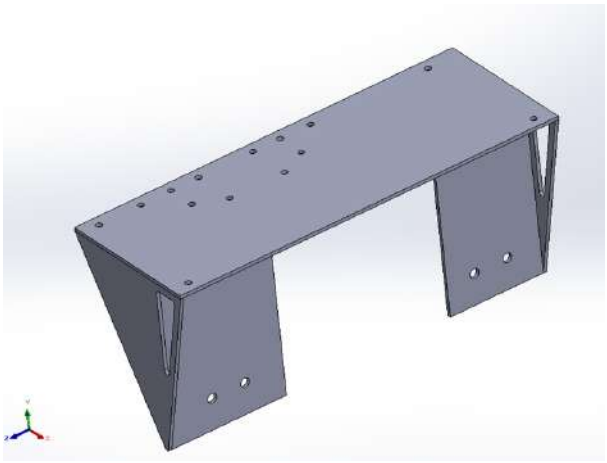

Figure 150: GW Mount Assembly

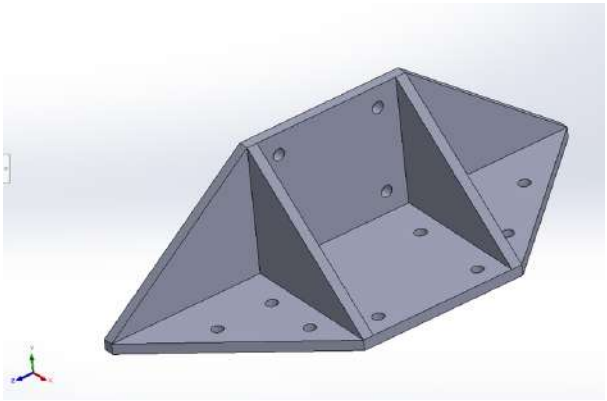

Figure 151: TS Mount Assembly

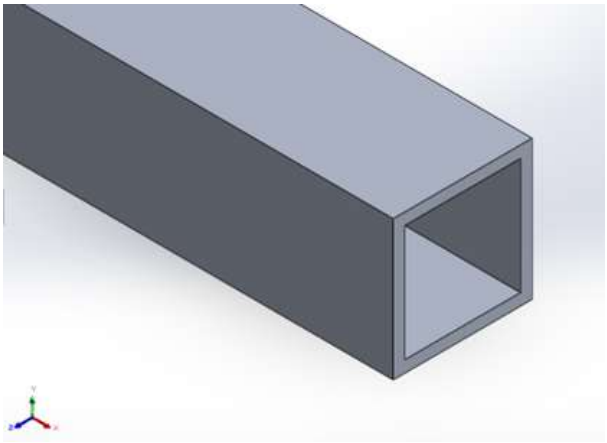

Figure 152: Square Tube Cross Section

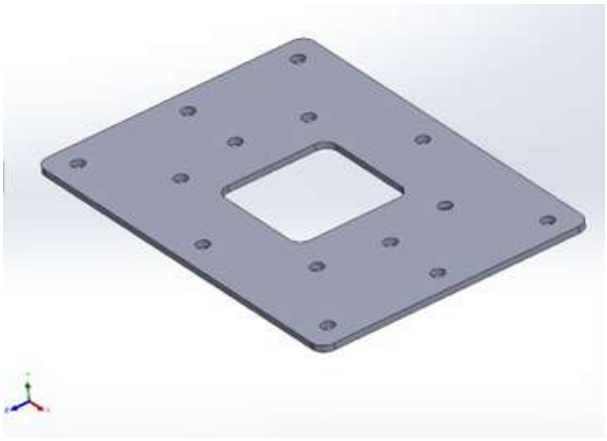

Figure 153: Braking Plate

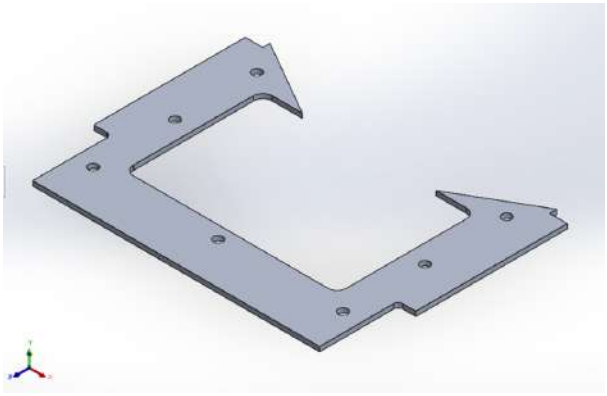

Figure 154: Braking Weldment

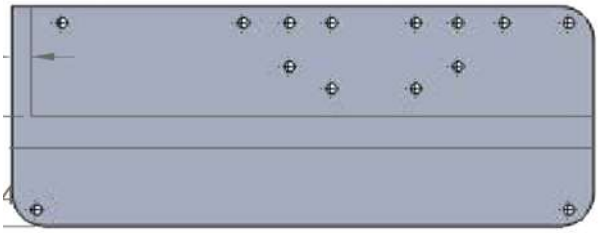

Figure 155: Guide Wheel weldment Right & Left

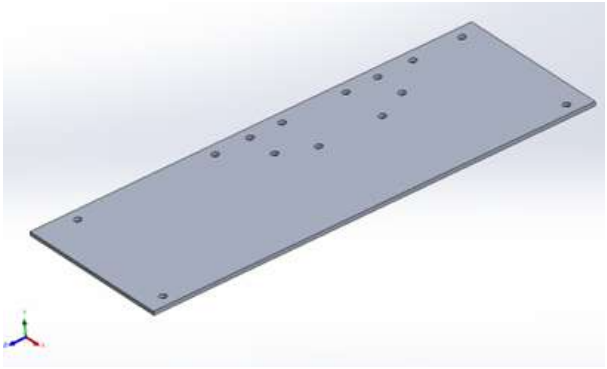

Figure 156: Guide Wheel mount top

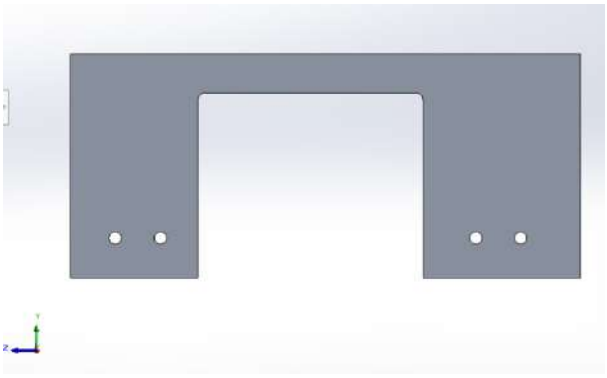

Figure 157: Guide Wheel mount front

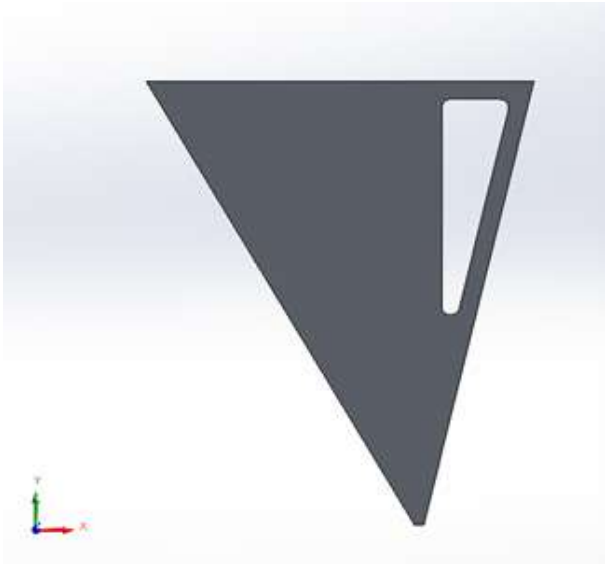

Figure 158: LH & RH Wheel Side Mount

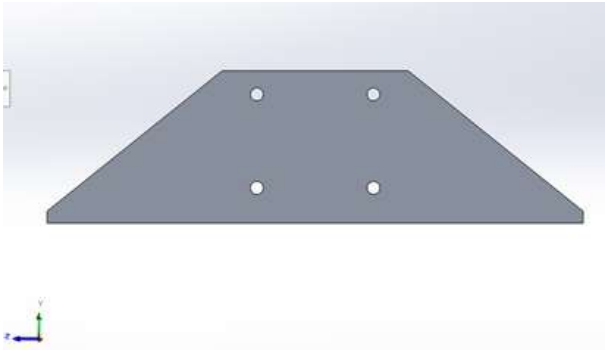

Figure 159: TS Mount Front

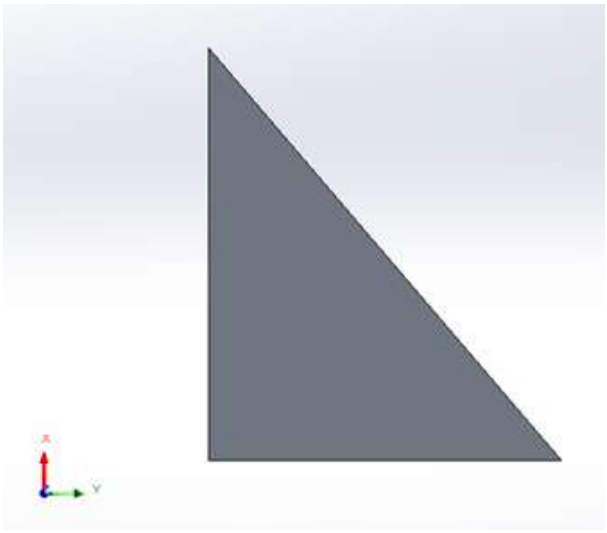

Figure 160: TS Mount Front

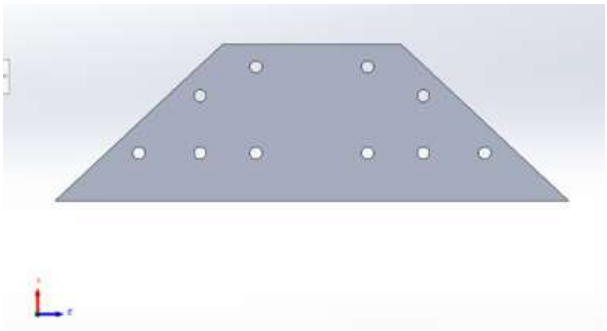

Figure 161: TS Mount Front

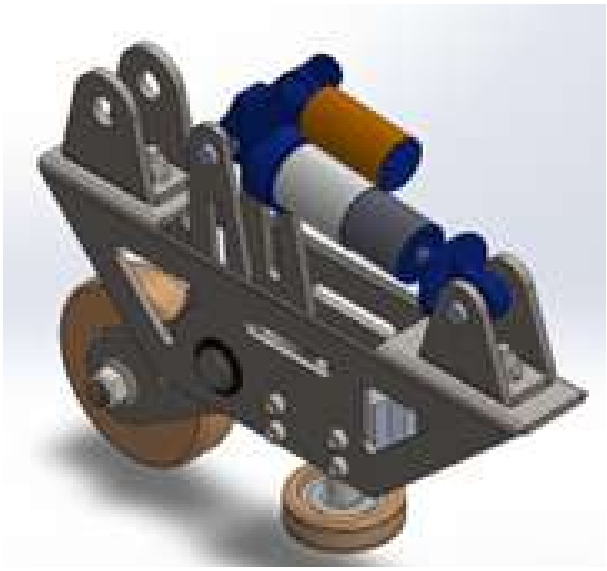

Figure 162: Side Suspension

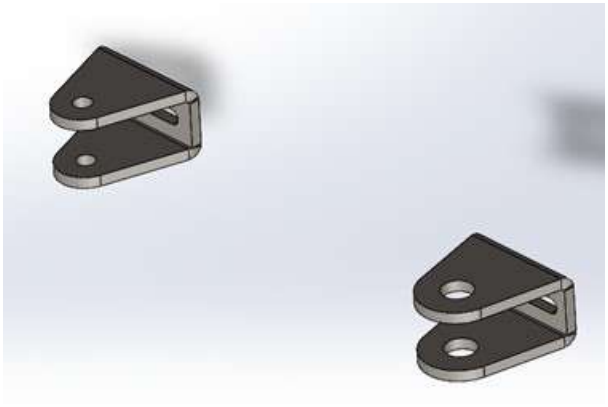

Figure 163: Front & Rear Chassis Brackets

Figure 164: Main Wheel Shaft

Figure 165: Rocker Swing Arm

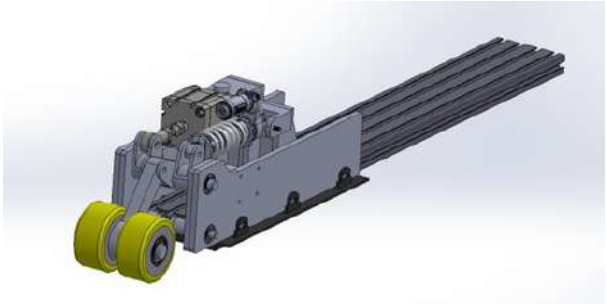

Figure 166: Top Suspension

Figure 167: L Linkage

Figure 168: Wheel Axle

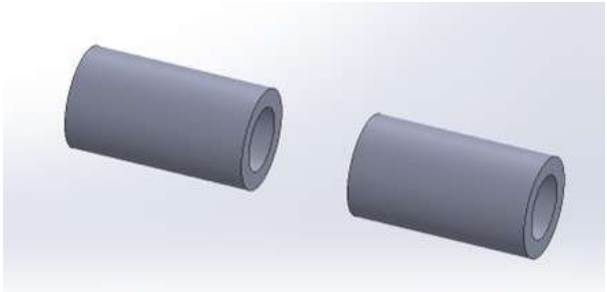

Figure 169: Bottom L Linkage

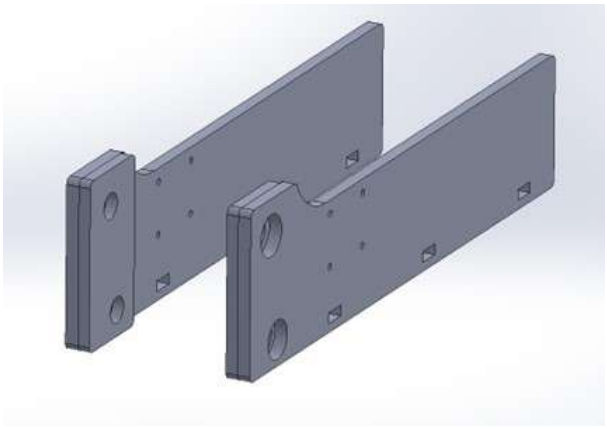

Figure 170: Side Plates (Right and Left)

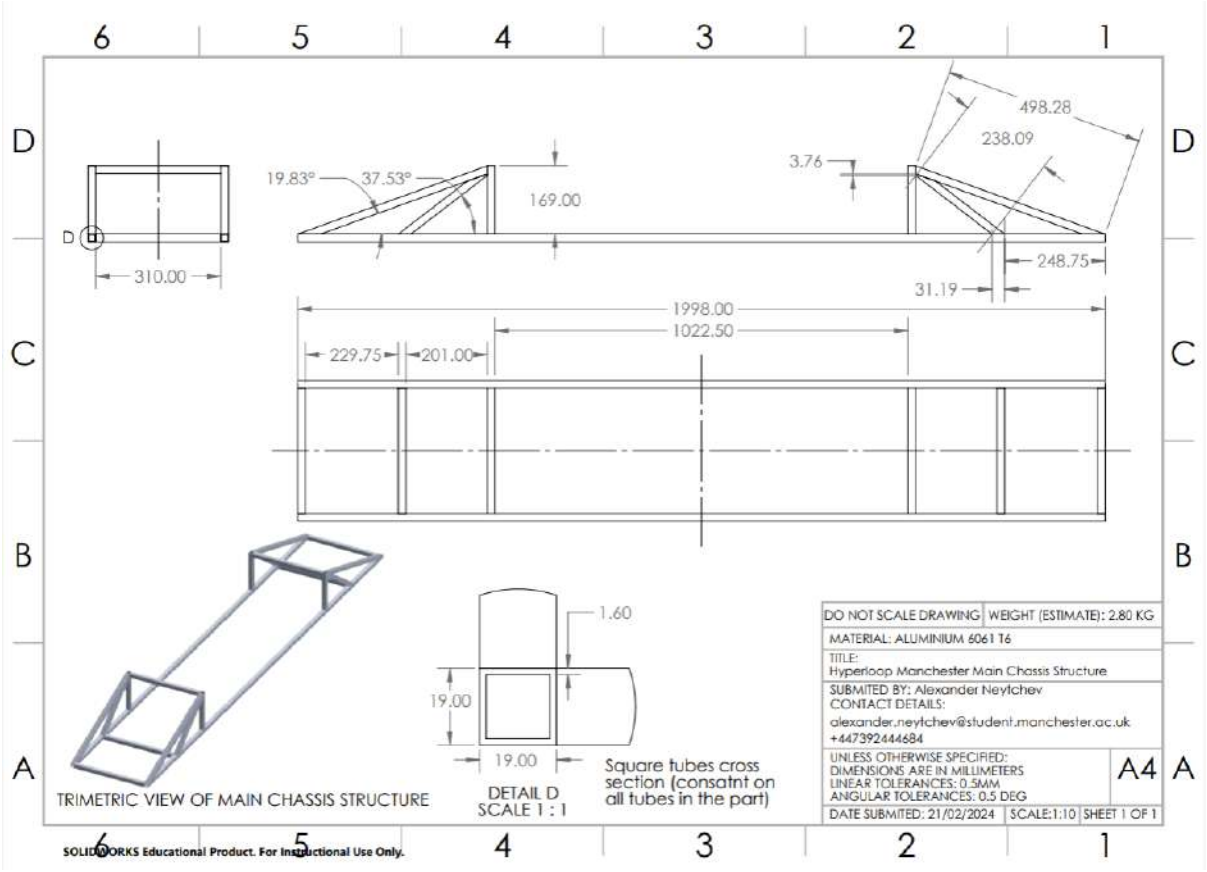

Figure 171: Main Chassis Structure

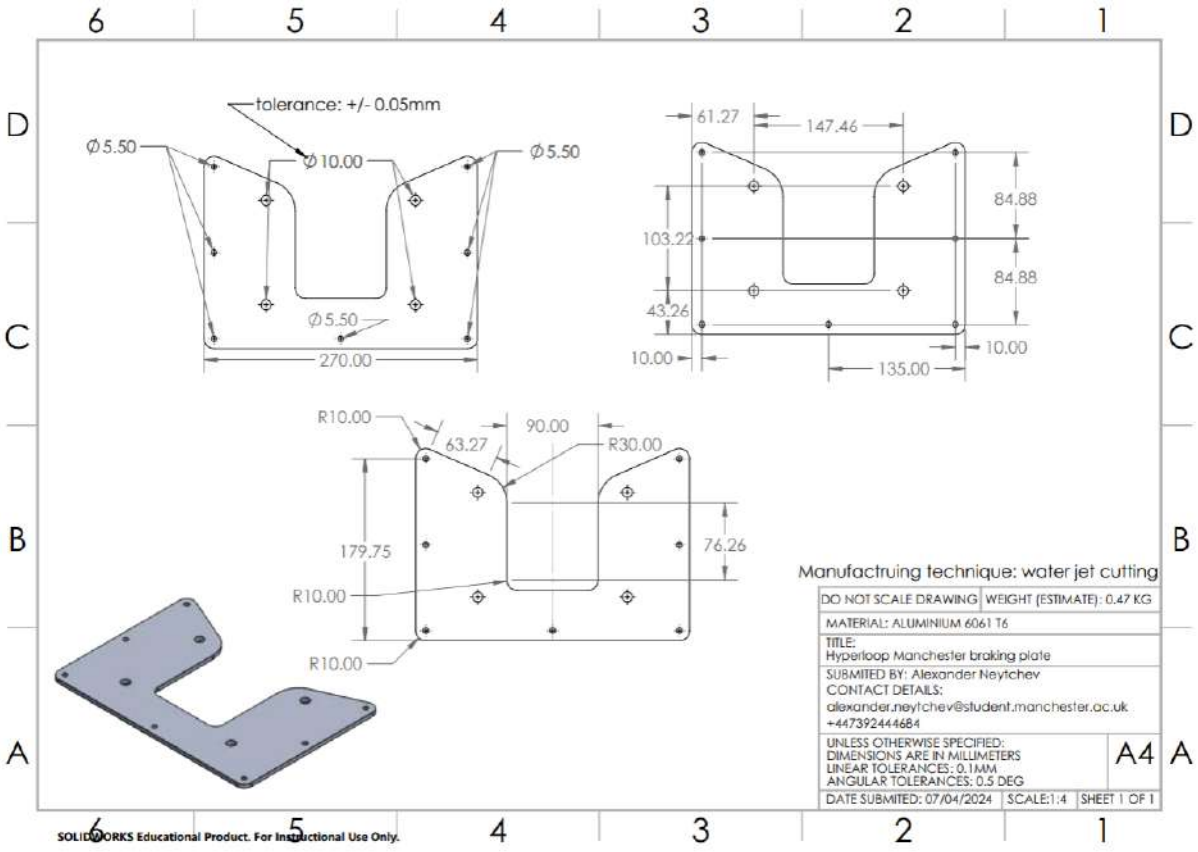

Figure 172: Braking Plate

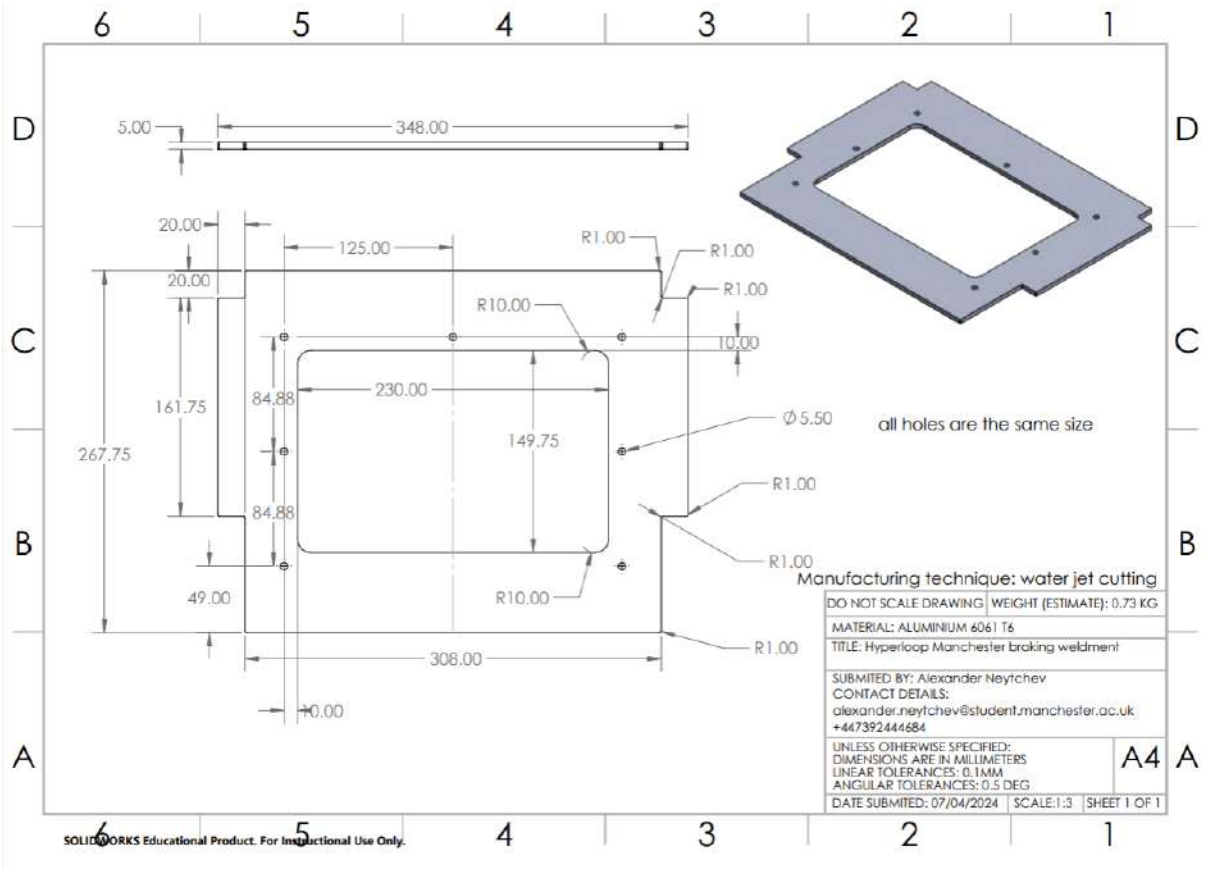

Figure 173: Braking Weldment

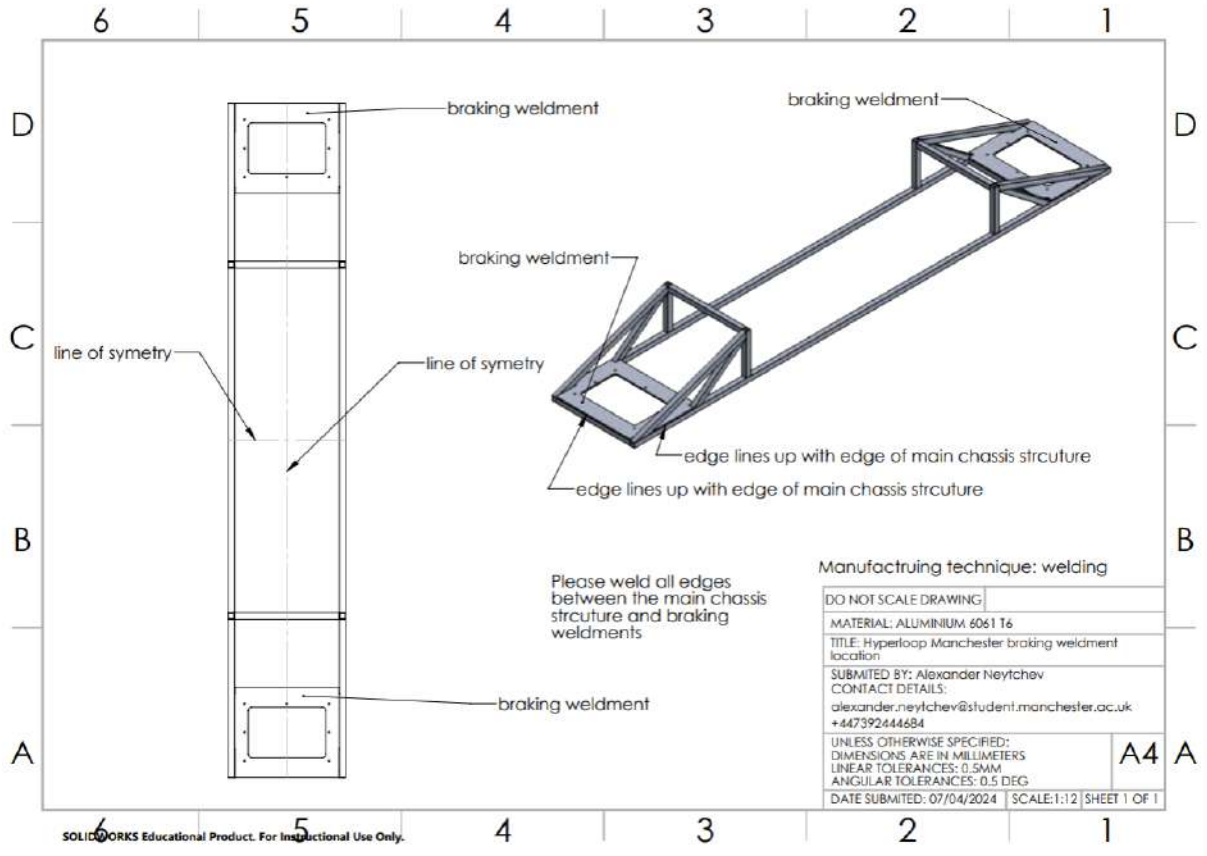

Figure 174: Braking Weldment Location

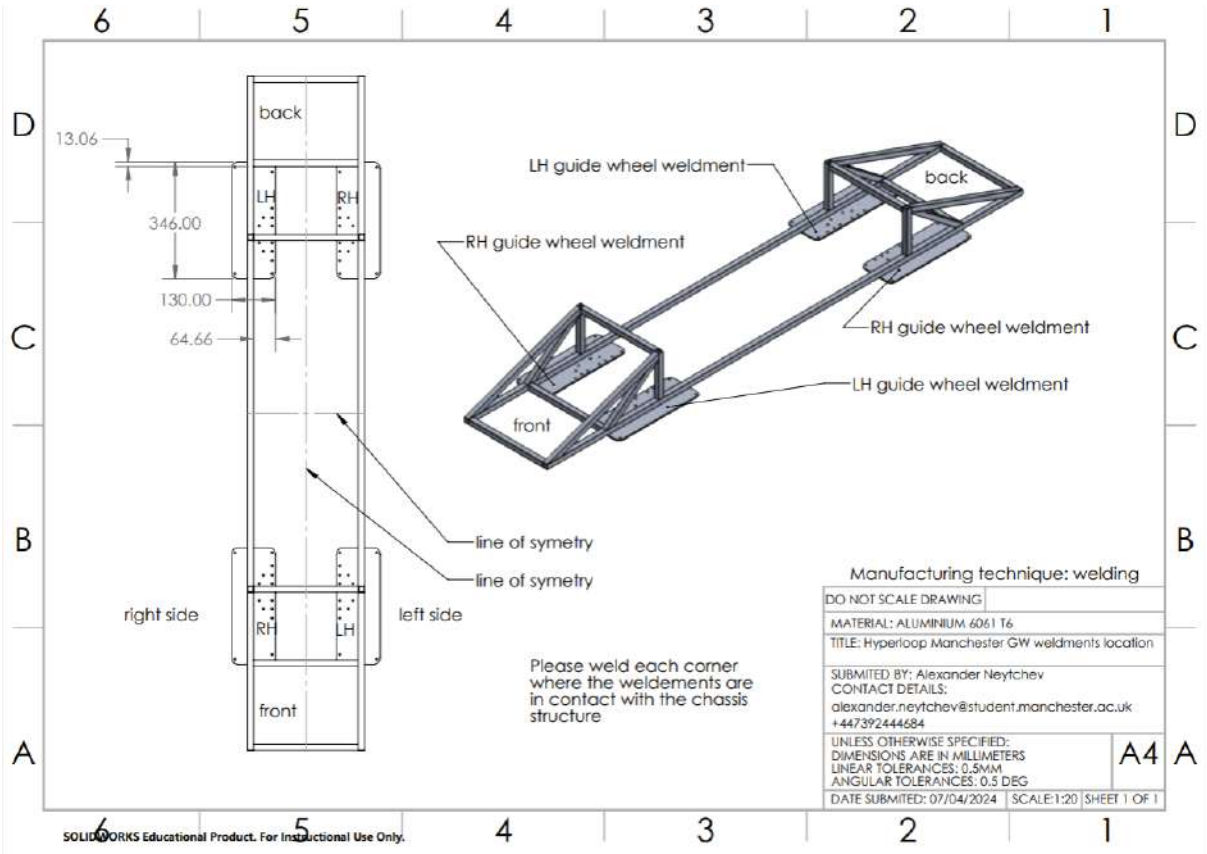

Figure 175: GW Weldment location

References

[1] N. Nick, "Aerodynamic design of a hyperloop pod by computational fluid dynamics analysis," 2019.

[2] M. Bizzozero, Y. Sato, and M. A. Sayed, "Aerodynamic study of a hyperloop pod equipped with compressor to overcome the kantrowitz limit," *Journal of Wind Engineering & Industrial Aerodynamics*, vol. 218, p. 104784, 2021. [Online]. Available: https://doi.org/10.1016/j.jweia.2021.104784

[3] H. Takeda *et al.*, "Japanese superconducting maglev: Present state and future perspective," *Physica B: Condensed Matter*, vol. 164, no. 1–2, pp. 229–235, 1990. [Online]. Available: https://doi.org/10.1016/0921-4526(90)90081-5

[4] F. L. de Wit and T. Terpstra, "Conceptual feasibility study of hyperloop vehicle thermal management systems," Delft Hyperloop VII, 2023.

[5] A. M. Limited, "Aluminium alloy 6061 - aerocom metals limited," 2022, accessed: February 5, 2025. [Online]. Available: https://aerocommetals.co.uk/featured-inventory/aluminium-alloy-6061/

[6] A. Velling, "Stainless steels aisi 304 vs 316 – the difference and use-cases," *Fractory*, 2024, accessed: February 5, 2025. [Online]. Available: https://fractory.com/stainless-steels-aisi-304-vs-aisi-316/

[7] M. Davies, "Water jet cutting advantages and disadvantages," 2018, accessed: February 5, 2025. [Online]. Available: https://www.tmcwaterjet.co.uk/news-blog/water-jet-cutting-advantages-and-disadvantages/

[8] M. Hepburn, "What are the advantages and disadvantages of cnc turning?" 2023, accessed: February 5, 2025. [Online]. Available: https://knowcnc.com/what-are-the-advantages-and-disadvantages-of-cnc-turning/

[9] O. Zienkiewicz, R. Taylor, and D. Fox, *The Finite Element Method for Solid and Structural Mechanics*. Elsevier, 2014.

[10] F. Shao, "Design analysis and optimization of the hyperloop shell and chassis," Master's thesis, DiVA Portal, 2019, accessed 14 Apr. 2024.

[11] V. Apanovitch, "Altair simsolid technology overview," Altair, Technical Report, 2020.

[12] S. S. Rao, *Mechanical Vibrations*, 6th ed. Prentice Hall, 2011.

[13] MatWeb, "Aluminum 6061-t6 data sheet," 2024, available online at https://www.matweb.com [Accessed 2024].

[14] Ansys, *Best Practice: RANS Turbulence Modeling in Ansys CFD*, Ansys, 2022.

[15] Ö. Ozer and M. Quinn, "Progress towards a miniaturised piv system," *Journal Name*, 2022.